

AMERICAN UNIVERSITY OF BEIRUT

HIGHLY CRYSTALLIZED ZINC OXIDE THIN FILMS
GROWN BY PULSED LASER DEPOSITION

by
SHATHA TARIK KAASSAMANI

A thesis
submitted in partial fulfillment of the requirements
for the degree of Master of Science
to the Department of Physics
of the Faculty of Arts and Sciences
at the American University of Beirut

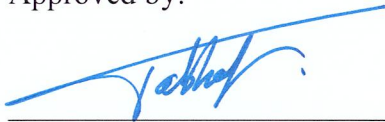
Beirut, Lebanon
March 2017

AMERICAN UNIVERSITY OF BEIRUT

HIGHLY CRYSTALLIZED ZINC OXIDE THIN FILMS
GROWN BY PULSED LASER DEPOSITION

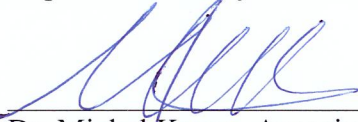
by
SHATHA TARIK KAASSAMANI

Approved by:



Dr. Malek Tabbal, Professor
Department of Physics

Advisor



Dr. Michel Kazan, Associate Professor
Department of Physics

Member of Committee



Dr. Digambara Patra, Associate Professor
Department of Chemistry

Member of Committee

Date of thesis defense: March 8, 2017

AMERICAN UNIVERSITY OF BEIRUT

THESIS, DISSERTATION, PROJECT RELEASE FORM

Student Name: Kaassamani Shatha Tarik
Last First Middle

Master’s Thesis Master’s Project Doctoral Dissertation


I authorize the American University of Beirut to: (a) reproduce hard or electronic copies of my thesis, dissertation, or project; (b) include such copies in the archives and digital repositories of the University; and (c) make freely available such copies to third parties for research or educational purposes.

I authorize the American University of Beirut, to: (a) reproduce hard or electronic copies of it; (b) include such copies in the archives and digital repositories of the University; and (c) make freely available such copies to third parties for research or educational purposes after :

One ---- year from the date of submission of my thesis, dissertation, or project.

Two ---- years from the date of submission of my thesis, dissertation, or project.

Three ---- years from the date of submission of my thesis, dissertation, or project.

 Signature	27/03/2017 Date
--	--------------------

This form is signed when submitting the thesis, dissertation, or project to the University Libraries

ACKNOWLEDGMENTS

First, I would like to express my deepest gratitude to my advisor Prof. Malek Tabbal for his guidance, motivation and continuous support at all times. Thank you for believing in my potentials and for trusting me. I really hope I met your expectations. Besides, I would also like to offer a very special thanks to Prof. Michel Kazan for his advice, support, help and contribution to this work. I thank you for being available at any time and ready to help with enthusiasm. I'm truly honored and had the pleasure to work with both of you.

Second, I am sincerely thankful to Dr. Wassim Kassem for his extreme help and dedication to this work. I've learned a lot from you during a relatively short period of time. You became more like a friend who's always supporting and advising. I cannot forget the times we spent together; you made my research experience at AUB a memorable one.

Many thanks also go to Prof. Digambara Patra, the thesis committee member, Prof. Youssef Mouneimne, the director of the CRSL (Central Research Science Laboratory), Miss Rania Shatila, the lab manager and the lab engineer, Juan Younes for their patience and help in doing the experimental work. To our Administrative Assistant, Jumana Abi Falah, and Elie Melki in the machine shop thank you for all the help you provided.

Last but not least, I send special thanks to Abdo Iskandar, who participated in part of the work, for his help and encouragement; I really enjoyed working with you. I am also grateful to my colleague and friend Laurence Shamseddine for all the pleasant and tough moments we've been through together during our stay at AUB.

Finally, I cannot not mention my parents and take the opportunity here to offer them my sincerest love and gratitude for their unconditional love and endless support they've showed throughout all these years at all times, and for all the sacrifices they've done for me to be here at AUB and at this level.

AN ABSTRACT OF THE THESIS OF

Shatha Tarik Kaassamani for Master of Science
Major: Physics

Title: Highly Crystallized Zinc Oxide Thin Films Grown by Pulsed Laser Deposition

This thesis deals with the synthesis of zinc oxide (ZnO) thin films by the pulsed laser deposition technique (PLD). Since the chemical and physical properties of ZnO are highly dependent on the growth process conditions, special emphasis was placed on the effect of the various deposition parameters on the composition, structural, and morphological properties of the deposited thin films with the search for the optimal conditions. For this, the effect of the substrate temperature, background oxygen pressure and laser power, including laser energy and repetition rate were specifically investigated. The crystalline quality, elemental composition and morphology of the resulting thin films were studied by *X-Ray Diffraction (XRD)*, *Energy Dispersive X-Ray Spectroscopy (EDX)* and *Scanning Electron Microscopy (SEM)*, respectively. In parallel, their optical properties were determined by near infrared visible and ultra-violet (UV-VIS-NIR) spectroscopy, from which the experimental data collected and a corrected Kramers-Kronig model the optical dielectric function of the deposited ZnO thin films was extracted, and their band gap energy was calculated. Moreover, the deposition on large area substrates was also investigated to study the uniformity of the deposited ZnO thin film over the full area.

CONTENTS

ACKNOWLEDGMENTS	v
ABSTRACT.....	vi
LIST OF ILLUSTRATIONS.....	xi
LIST OF IMAGES.....	xvi
LIST OF TABLES	xvii

Chapter

1. PULSED LASER DEPOSITION OF THIN FILMS.....	1
1.1. History and Evolution of Pulsed Laser Deposition	1
1.2. Fundamentals and General Features of Pulsed Laser Deposition.....	2
1.3. Mechanisms of Pulsed Laser Deposition.....	4
1.3.1. Laser-Target Interaction	4
1.3.2. Plasma Plume Generation and Expansion	5
1.3.3. Film Growth.....	5
1.4. Advantages and Disadvantages of Pulsed Laser Deposition	7
1.5. More About Pulsed Laser Deposition.....	8
2. GENERAL PROPERTIES, LITERATURE REVIEW AND PLD GROWTH OF ZnO.....	10
2.1. Introduction.....	10

2.2. Crystal Structure of ZnO	10
2.3. Physical Parameters of ZnO	11
2.4. Pulsed Laser Deposition of Zinc Oxide.....	12
3. EXPERIMENTAL TECHNIQUES AND PROCEDURE	19
3.1. Introduction.....	19
3.2. PLD Experimental Setup	19
3.3. Characterization Techniques and Analysis of Thin Films.....	20
3.3.1. X-Ray Diffraction (XRD) Techniques and Analysis	20
3.3.1.1. Full Width Half Maximum (FWHM) of the XRD Peak w	26
3.3.1.2. Lattice Constant c	26
3.3.1.3. The Strain ϵ	27
3.3.1.4. Average Grain Size h	28
3.3.1.5. Rocking Curves (RC)	31
3.3.2. Surface Profilometry.....	32
3.3.3. Scanning Electron Microscopy (SEM).....	34
3.3.4. Energy-Dispersive X-Ray Spectroscopy (EDX)	38
3.3.5. UV-VIS Spectroscopy	39
3.3.5.1. Kramers-Kronig Method	40
3.3.5.2. Energy Loss Function.....	47
3.3.5.3. Band gap energy E_g	48
3.4. Experimental Procedure.....	50
3.5. Materials and Experimental Details.....	52
4. RESULTS AND DISCUSSION.....	53
4.1. Introduction.....	53
4.2. Effect of Oxygen Pressure at 725°C.....	53
4.2.1. XRD results and analysis.....	54
4.2.2. SEM images and discussion	59
4.2.3. EDX results and analysis	61
4.2.4. Optical Properties	61
4.3. Effect of Substrate Temperature	65

4.3.1. XRD results and analysis.....	66
4.3.2. SEM images and discussion	72
4.3.3. EDX results and analysis	74
4.3.4. Optical Properties	74
4.4. Effect of Oxygen Pressure at 825°C	78
4.4.1. XRD results and analysis.....	78
4.4.2. SEM images and discussion	85
4.4.3. EDX results and analysis	88
4.4.4. Thickness measurements	88
4.4.5. Optical Properties	89
4.5. Effect of Laser Energy	94
4.5.1. XRD results and analysis.....	95
4.5.2. SEM images and discussion	100
4.5.3. EDX results and analysis	101
4.5.4. Optical Properties	101
4.6. Effect of Laser Repetition Rate	104
4.6.1. XRD results and analysis.....	105
4.6.2. Thickness measurements	110
4.6.3. SEM images and discussion	111
4.6.4. EDX results and analysis	112
4.6.5. Optical Properties	113
4.7. Large Area Depositions	115
4.8. Summary.....	120
4.9. Further Analysis.....	121
4.9.1. Variation of the Band gap, strain and FWHM XRD peak as function of O ₂ pressure at 725°C	121
4.9.2. Variation of the Band gap, strain and FWHM XRD peak as function of substrate temperature at 10 mTorr	123
4.9.3. Variation of the Band gap, strain and FWHM XRD peak as a function of O ₂ pressure at 825°C	125
4.9.4. Variation of the Band gap, strain and FWHM XRD peak as a function of laser energy at 10 mTorr and 725°C	126
4.9.5. Variation of the Band gap, strain and FWHM XRD peak as a function of laser repetition rate at 10 mTorr and 725°C.....	128

5. CONCLUSION AND FUTURE DIRECTION OF THE WORK	129
5.1. Conclusion	129
5.2. Future Work.....	133
Appendix	
APPENDIX A.....	134
APPENDIX B	135
APPENDIX C	136
APPENDIX D.....	139
APPENDIX E	140
REFERENCES	141

ILLUSTRATIONS

Figure	Page
1.1. Schematic representation of the Pulsed Laser Deposition (PLD)	3
1.2. Schematic representation of thin film growth modes	6
2.1. Wurtzite structure	11
2.2. Zinc blende structure	11
2.3. Rocksalt structure	11
3.1. Pulsed Laser Deposition (PLD) setup	20
3.2. Bragg's law geometry	21
3.3. Geometry of scattering vector construction.....	22
3.4. Schematic representation of $\theta/2\theta$ scan	22
3.5. Bruker AXS D8 Discover X-ray diffractometer used	23
3.6. EVA match for XRD pattern of S1 sample	24
3.7. Double Lorentzian fit on the XRD peak.....	25
3.8. Schematic representation of the stylus profilometer	33
3.9. Line profile of S11 sample	34
3.10. Cross section representation of the optical elements of the SEM	36
3.11. Integral Contour for deriving K-K relations.....	42
3.12. Energy loss function versus the wavenumber of the ZnO target.....	48
3.13. Smoothed energy loss function of the ZnO target	49
3.14. The envelope of the energy loss function of the ZnO target	49
4.1. $\theta/2\theta$ scans for samples deposited at different oxygen pressures and substrate temperature 725°C	54
4.2. Variation of the lattice constant c and the strain ε with oxygen pressure for films deposited at substrate temperature 725°C	55
4.3. Variation of the width of the (002) peak with oxygen pressure for films deposited at substrate temperature 725°C	56

4.4.	Variation of the average grain height h as a function of oxygen pressure for films deposited at substrate temperature 725°C	56
4.5.	Rocking Curves of S5, S0 and S6 samples; the ZnO films deposited at 1, 10 and 100 mTorr of oxygen pressure, respectively.....	57
4.6.	Variation of the FWHM rocking curves as a function of background oxygen pressure, for films deposited at 725°C of substrate temperature	58
4.7.	Reflectance spectra of ZnO films deposited at different oxygen pressures and substrate temperature 725°C	62
4.8.	Energy loss functions of ZnO films deposited at different oxygen pressures and substrate temperature 725°C	63
4.9.	Variation of the band gap energy value as a function of oxygen pressure for films deposited at substrate temperature 725°C	64
4.10.	$\theta/2\theta$ scans for samples deposited at different substrate temperatures and oxygen pressure of 10 mTorr.....	66
4.11.	Variation of the lattice constant c and the strain ϵ as a function of substrate temperature for films deposited at oxygen pressure of 10 mTorr	68
4.12.	Variation of the width of the (002) peak with substrate temperature for films deposited at 10 mTorr oxygen pressure.....	69
4.13.	Variation of the average grain height h as a function of substrate temperature for films deposited at 10 mTorr oxygen pressure.....	69
4.14.	Rocking Curves of S3, S0 and S2 samples; the ZnO films deposited at a substrate temperature of 625°C , 725°C and 825°C	70
4.15.	Variation of the FWHM rocking curves as a function of substrate temperature, for films deposited at 10 mTorr of oxygen pressure.....	70
4.16.	Schematic representation of scattered x-rays from domains with low-angle boundaries.....	71
4.17.	Reflectance spectra of ZnO films deposited at different substrate temperatures and 10 mTorr oxygen pressure	75
4.18.	Energy loss functions of ZnO films deposited at different substrate temperatures and 10 mTorr oxygen pressure.....	76
4.19.	Variation of the band gap energy value as a function of substrate temperature for films deposited at 10 mTorr oxygen pressure	77
4.20.	$\theta/2\theta$ scans for samples deposited at different background oxygen pressures and substrate temperature 825°C	79

4.21.	Variation of the lattice constant c as a function of oxygen pressure for films deposited at substrate temperature 825°C.....	80
4.22.	Variation of the width of the (002) peak with oxygen pressure for films deposited at substrate temperature 825°C.....	81
4.23.	Variation of the average grain height h as a function of oxygen pressure for films deposited at substrate temperature 825°C	82
4.24.	Rocking curves of S7, S8, S9, S10, S11 and S12 samples; the ZnO films deposited at 25, 50, 75, 100, 200, and 500 mTorr of oxygen pressure, respectively	83
4.25.	Variation of the FWHM rocking curves as a function of oxygen pressure, for films deposited at a substrate temperature of 825°C	84
4.26.	Variation of the thickness of the films deposited at different background oxygen pressures and substrate temperature 825°C	89
4.27.	Reflectance spectra of ZnO films deposited at different oxygen pressures and substrate temperature 825°C.....	90
4.28.	Energy loss functions of ZnO films deposited at different oxygen pressures, and 825°C substrate temperature	91
4.29.	Variation of the band gap energy value as a function of oxygen pressure for films deposited at substrate temperature 825°C	93
4.30.	Schematic representation of the energy levels of the intrinsic defects in ZnO thin films.....	93
4.31.	$\theta/2\theta$ scans for samples deposited at different laser energies, substrate temperature 725°C and 10 mTorr of oxygen pressure.....	95
4.32.	Variation of the lattice constant c and the strain ϵ as a function of laser energy for films deposited at 10 mTorr oxygen pressure and substrate temperature 725°C	96
4.33.	Variation of the width of the (002) peak with laser energy for films deposited at 10 mTorr oxygen pressure and substrate temperature 725°C.....	97
4.34.	Variation of the average grain height h as a function of laser energy for films deposited at 10 mTorr oxygen pressure and substrate temperature 725°C	97
4.35.	Rocking Curves of S1 and S0 samples; the ZnO films deposited at laser energy of 200 mJ and 400 mJ respectively.....	98
4.36.	Variation of the FWHM rocking curves as a function of laser energy, for films deposited at 10 mTorr of oxygen pressure and 725°C of substrate temperature	99

4.37.	Reflectance spectra of ZnO films deposited at different laser energies, 10 mTorr oxygen pressure and substrate temperature 725°C.....	102
4.38.	Energy loss functions of ZnO films deposited at different laser energies, 10 mTorr oxygen pressure and substrate temperature 725°C.....	103
4.39.	Variation of the band gap energy value as a function of laser energy, for films deposited at 10 mTorr of oxygen pressure and 725°C of substrate temperature	104
4.40.	$\theta/2\theta$ scans for samples deposited at different laser repetition rates, substrate temperature 725°C and 10 mTorr oxygen pressure	105
4.41.	Variation of the lattice constant c and the strain ϵ as a function of laser repetition rate for films deposited at 10 mTorr oxygen pressure and substrate temperature 725°C	106
4.42.	Variation of the width of the (002) peak with laser repetition rate for films deposited at 10 mTorr oxygen pressure and substrate temperature 725°C	107
4.43.	Variation of the average grain height h as a function of laser repetition rate for films deposited at 10 mTorr oxygen pressure and substrate temperature 725°C	108
4.44.	Rocking curves of S0 and S4 samples; the ZnO films deposited at a laser repetition rate of 20 Hz and 50 Hz respectively	109
4.45.	Variation of the FWHM rocking curves as a function of laser repetition rate, for films deposited at 10 mTorr of oxygen pressure and 725°C of substrate temperature	109
4.46.	Variation of the thickness of the films deposited at different laser repetition rates, 10 mTorr oxygen pressure and substrate temperature 725°C	110
4.47.	Reflectance spectra of ZnO films deposited at different laser frequencies, 10 mTorr oxygen pressure and substrate temperature 725°C.....	113
4.48.	Energy loss functions of ZnO films deposited at different laser frequencies, 10 mTorr oxygen pressure and substrate temperature 725°C.....	114
4.49.	Variation of the band gap energy value as a function of laser repetition rate, for films deposited at 10 mTorr of oxygen pressure and 725°C of substrate temperature	115
4.50.	Schematic representation of the three silicon pieces pasted on the metal plate	116
4.51.	Cross-sectional SEM of sample I for the (a) 1 (b) 2 and (c) 3 pieces.....	117
4.52.	Cross-sectional SEM of sample II for the (a) 1 (b) 2 and (c) 3 pieces	117

4.53.	Cross-sectional SEM of sample III for the (a) 1 (b) 2 and (c) 3 pieces	117
4.54.	$\theta/2\theta$ scan of sample III	119
4.55.	GIXRD of sample III	120

IMAGES

Image	Page
3.1. Schematic representation of a rocking curve scan.....	32
3.2. Elemental composition report by INCA of one of our samples (S2 sample) ...	39
4.1. SEM images of S5, S0 and S6 samples, the ZnO films deposited at (a) 1, (b) 10 and (c) 100 mTorr of oxygen pressure respectively, and 725°C of substrate temperature.	60
4.2. SEM images of S3, S0 and S2 samples, the ZnO films deposited at (a) 625, (b) 725 and (c) 825°C of substrate temperature respectively, and 10 mTorr of oxygen pressure	73
4.3. SEM images of S7, S8, S9, S10, S11 and S12 samples, the ZnO film deposited at (a) 25, (b) 50, (c) 75, (d) 100, (e) 200 and (f) 500 mTorr of oxygen pressure respectively, and 825°C of substrate temperature	86
4.4. SEM images of S1 and S0 samples, the ZnO films deposited at a laser energy of (a) 200 and (b) 400 mJ respectively, 10mTorr of oxygen pressure and 725°C of substrate temperature.....	100
4.5. SEM images of S0 and S4 sample, the ZnO films deposited at a repetition rate of (a) 20 and (b) 50 Hz, respectively, 10 mTorr of oxygen pressure and 725°C of substrate temperature.....	111

TABLES

Table		Page
2.1.	Physical parameters of ZnO.....	11
2.2.	Summary of the work done by many authors on the growth of high quality ZnO thin films by PLD	18
4.1.	Experimental conditions for samples grown at different oxygen pressures and substrate temperature 725°C.....	53
4.2.	The lattice constant c , the strain ϵ , the (002) peak width and the average grain height h of films deposited at different oxygen pressures and substrate temperature 725°C.....	55
4.3.	The atomic composition of films deposited at different background oxygen pressures and substrate temperature 725°C	61
4.4.	Band gap energy values for films deposited at different oxygen pressures and substrate temperature 725°C.....	64
4.5.	Experimental conditions for samples grown at different substrate temperatures and background oxygen pressure of 10 mTorr.....	66
4.6.	The lattice constant c , the strain ϵ , the (002) peak width and the average grain height h of films deposited at different substrate temperatures and oxygen pressure of 10 mTorr	67
4.7.	The atomic composition of films deposited at different substrate temperatures and 10 mTorr oxygen pressure	74
4.8.	Band gap energy values for films deposited at different substrate temperatures and 10 mTorr oxygen pressure	77
4.9.	Experimental conditions for samples grown at different background oxygen pressures and substrate temperature 825°C	78
4.10.	The lattice constant c , the strain ϵ , the (002) peak width and the average grain height h of films deposited at different oxygen pressures and substrate temperature 825°C.....	80
4.11.	The atomic composition of films deposited at different background oxygen pressures and substrate temperature 825°C	88
4.12.	Band gap energy values for films deposited at different oxygen pressures and substrate temperature 825°C.....	92

4.13.	Experimental conditions for samples grown at different laser energies, 10 mTorr oxygen pressure and substrate temperature 725°C.....	94
4.14.	The lattice constant c , the strain ϵ , the (002) peak width and the average grain height h of films deposited at different laser energies, 10 mTorr oxygen pressure and substrate temperature 725°C.....	96
4.15.	The atomic composition of films deposited at different laser energies, 10 mTorr oxygen pressure and substrate temperature 725°C.....	101
4.16.	Band gap energy values for films deposited at different laser energies, 10 mTorr oxygen pressure and substrate temperature 725°C.....	103
4.17.	Experimental conditions for samples grown at different laser repetition rates, 10 mTorr oxygen pressure and substrate temperature 725°C.....	104
4.18.	The lattice constant c , the strain ϵ , the (002) peak width and the average grain height h of films deposited at different laser repetition rates, 10 mTorr oxygen pressure and substrate temperature 725°C.....	106
4.19.	The atomic composition of films deposited at different laser frequencies, 10 mTorr oxygen pressure and substrate temperature 725°C.....	112
4.20.	Band gap energy values for films deposited at different laser repetition rates, 10 mTorr oxygen pressure and substrate temperature 725°C.....	115
4.21.	Deposition conditions for large area samples.....	116
4.22.	Average thickness of large area deposited samples.....	118
4.23.	Percentage difference in thickness among the different deposited ZnO thin film pieces for each sample	118

Chapter 1

PULSED LASER DEPOSITION OF THIN FILMS

1.1. History and Evolution of Pulsed Laser Deposition

The principle of pulsed laser deposition arose ever since the invention of the laser, back then this technique was not even given a name. In the period of 1970 to 1979 two major developments occurred, considered as improvements to what is now known as pulsed laser deposition (PLD). The first was the ability to generate very short laser pulses to produce high power density, which serves for congruent evaporation to deposit stoichiometric thin films, and to transform the species evaporated from the irradiated material into the form of plasma, and the second development is the high efficiency second harmonic generation to generate shorter wavelength radiation which also favors congruent evaporation. Both developments enhanced the film quality and a number of works was performed during that period including deposition of semiconducting thin films (Chrisey & Hubler, 1994).

In the period of 1980 to 1987, with the progress of laser technology towards an improved quality an increased number of depositions were done using the PLD technique and the resulting thin films showed an improved quality; oxides and fluorides were grown and high-quality II-VI semiconductor thin films were deposited using a Nd:YAG laser at Rockwell International Science Center and the National Research Council of Canada. This promoted PLD as a promising thin-film growth technique; however, till that time PLD remained acronym and not well-commonly named.

From 1987 till our present day, PLD has attracted significant interest and has gained its reputation and recognition. In 1989 participants in the first Material Research Society Symposium on Pulsed Laser Ablation held in San Francisco voted for pulsed laser deposition as the common name for PLD (Chrisey & Hubler, 1994). During this period, it was used to grow high-temperature superconducting films, in addition to oxides on semiconductors, nitrides such as AlN and BN, and diamond-like-carbon. Today, a large number of research laboratories are spread all around the world giving rise to a large amount of publications related to PLD, and there's more yet to come, certainly due to issues opened up by PLD concerning optimal deposition conditions, reproducibility, and large-area depositions, and more realistically, due to the growing need of nano-films in micro-electronic devices in nanotechnology nowadays.

1.2. Fundamentals and General Features of Pulsed Laser Deposition

The principle of pulsed laser deposition relies on the use of ultra-short laser pulses, typically tens of nanoseconds that are guided through a beam-line into a high-vacuum chamber and are focused by a lens to ablate a solid target. Due to the high power density of the laser pulses, of the order of 10^8 W cm^{-2} or more, the radiation absorbed by the target will be converted not only to electronic excitations, but also to thermal and then mechanical energy which causes energetic species such as atoms, ions, electrons, molecules, and micron-sized particulates to be ejected from the target in the form of plasma plume. This plasma plume expands and reaches a heated substrate placed above the target whose components participate in the deposition. Deposition is achieved in vacuum or in a chosen background gas in order to reduce contaminants.

Figure 1.1 shows a schematic representation of the principle of the PLD.

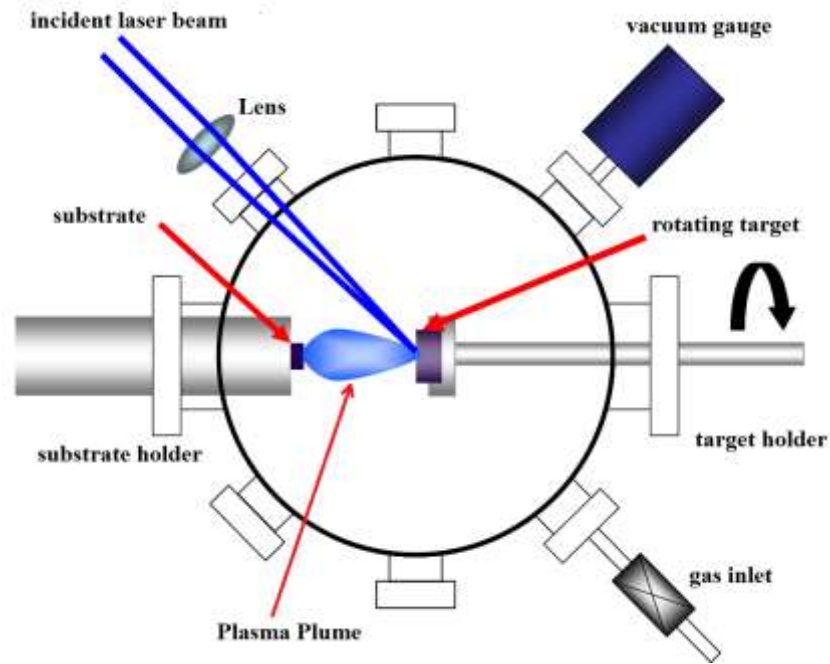


Figure 1.1: Schematic representation of the Pulsed Laser Deposition (PLD)

The lasers employed in PLD have ranged from mid infrared radiation such as CO₂ laser (10.6 μm), to near infrared and visible lasers, like the most often used Nd:YAG laser and its fundamental, second and fourth harmonics (1064 nm, 532 nm and 266 nm respectively), down to the ultraviolet lasers (Chrisey & Hubler, 1994). The latter have been constructed from excimers, unstable molecules, which are formed from a noble gas (xenon Xe, krypton Kr, argon Ar) in an excited state temporarily bond to a similar atom or a halogen such as fluorine F and chlorine Cl. This molecule then dissociates, within few picoseconds, by stimulated emission emitting a photon in the UV range. Lasers in which these molecules participate in the lasing action are hence called excimer lasers. Examples are: XeCl (308 nm), KrF (248 nm), ArF (193 nm), F₂ (157 nm).

1.3. Mechanisms of Pulsed Laser Deposition

In this section the general features discussed in section 1.2 will be more elaborated and explained. We focus on three main aspects that characterize PLD starting with the coupling of electromagnetic radiation with the bulk target material, the generation of the plume and its expansion away from the target towards the substrate, and finally the growth of the film. These three mechanisms may be viewed as conceptually and experimentally simple, but the physical processes involved are highly complex and interrelated.

1.3.1. *Laser-Target Interaction*

When laser pulses arrive on the target, the electromagnetic radiation will be absorbed and converted into electronic excitations. The excited electrons will transfer their energy to the lattice within few picoseconds, and the material will be heated within a depth of $1/\alpha$, known as the optical absorption depth L_o , where α is the optical absorption coefficient. The depth of the heated layer is determined by the thermal diffusion length, given by $L_T = 2\sqrt{D\tau}$, where D is the thermal diffusion constant, and τ is the pulse duration of the laser (Willmott & Huber, 2000). There are two possible considerations to be addressed:

1. $L_T < L_o$, the bulk material will be heated down to $1/\alpha$, independent of the pulse duration. When this condition is satisfied congruent evaporation from multielemental targets is established typically when using UV lasers.

2. $L_T > L_o$, all the electromagnetic energy from the laser pulses is captured in the absorption layer and then thermally transferred to a depth of L_T , the thermal diffusion depth.

1.3.2. *Plasma Plume Generation and Expansion*

Initially the ablated particles' velocities is described by a Maxwellian velocity distribution, however, reflections and collisions of particles will form a layer in contact with the target called the Knudsen layer, which will tend to thermally equilibrate the plasma and lower its degree of ionization, as a result modifying the velocity distribution to a drifted Maxwellian distribution:

$$P(v) \sim v^3 \exp[-m(v - \bar{v})^2 / 2kT]$$

where \bar{v} is the center-of-mass velocity, normal to the target surface - the direction of propagation of the plasma- m is the mass of the species, k the Boltzmann constant and T is the surface target temperature.

Upon expansion of the plasma into vacuum or ambient gas, its temperature adiabatically cools typically to a range of 3000-5000 K, and its species can possess kinetic energies normally in a range of 5-50 eV. Moreover, the angular distribution of the plasma plume was fitted by many authors to a $\cos^n \theta$ function, where n strongly depends on the laser fluence and the ambient pressure; it can take values from 2 to more than 20. To simplify the picture, when the surrounding is dense enough, multiple collisions occur, consequently broadening the angular distribution (i.e. a broad plume) and hence n takes low values (Willmott & Huber, 2000).

1.3.3. *Film Growth*

Lastly, the expanding plasma plume will reach a substrate, placed above the target and usually heated to a certain temperature, and recondense to build up a thin film. When an atom or ion arrives on the substrate it is destined either to re-evaporate from the surface or diffuse across the surface and then escape to the surrounding or bond with the surface and with other atoms. Sufficient surface diffusion allows the

adatoms to migrate and search for thermodynamically stable sites through which they can minimize their surface energy before a full monolayer is deposited; hence the realization of the significance of the substrate temperature for surface diffusion.

There are three conventional nucleation and growth modes to be considered upon thin film build up (Chrissey & Hubler, 1994):

- Three-dimensional island growth (Volmer-Weber) which involves the nucleation of atoms upon their arrival on the substrate to form clusters resulting in three-dimensional islands.
- Two-dimensional full-monolayer growth (Frank-van der Merwe), where one monolayer is deposited at a time resulting in a smooth epitaxial film (Abi Akl, 2009).
- Mixed Growth (Stranski-Krastinov) which combines the two previous modes; it is a two-dimensional growth of full monolayers followed by nucleation and growth of three-dimensional islands.

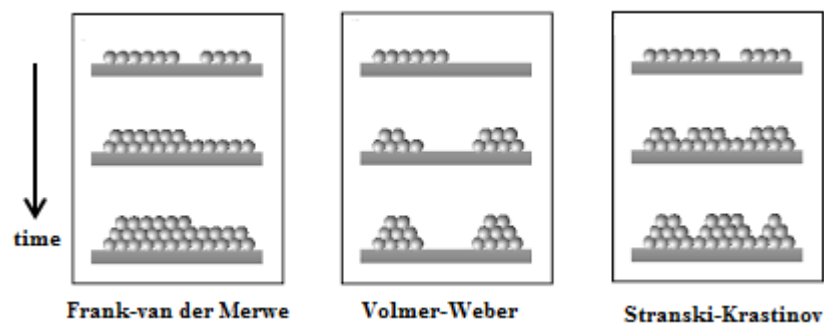


Figure 1.2: Schematic representation of thin film growth modes

What mode is involved during deposition strongly depends on the film-substrate interface energy and the thermodynamics that relates the substrate and film surface energies (Chrissey & Hubler, 1994).

1.4. Advantages and Disadvantages of Pulsed Laser Deposition

Just like any other deposition technique, the pulsed laser deposition has several advantages but naturally also have some drawbacks.

An outstanding aspect of the PLD technique is that the same stoichiometry of the target is usually recovered in the deposited thin films; a variety of stoichiometric thin films can be deposited in an appropriate choice of the background gas without the need for catalysts and further processing.

Almost any material can be ablated, and the growth rate of the films can be controlled (Willmott & Huber, 2000); successfully all materials from transparent dielectrics, semiconductors, metals to superconductors have been grown via PLD. Besides, the plasma plume generated is highly-directional which reduces contamination as opposed to unconfined plume in other processes. Finally, the preparation-deposition conditions can be varied to achieve a desirable quality of thin films; those include background gas pressure, which can be varied in PLD from vacuum ($\sim 10^{-7}$ mbar) up to tenths of milli-bars (hundreds of milliTorrs), the substrate temperature, and the target-substrate distance.

One of the major and problematic drawbacks of the pulsed laser deposition technique is “splashing”. Splashing is the ejection of micron-sized particulates or macroscopic particulates throughout the ablation process; three reasons for its occurrence are subsurface boiling, recoil ejection and exfoliation. Briefly, subsurface boiling is the superheating of the subsurface layer before surface material is ablated hence the boiling subsurface materials are ejected as micron-sized globules, recoil ejection is also termed shock-wave-induced droplet expulsion, and it is caused by the recoil force or pressure exerted by the plasma plume; the ejected particulates are in the submicron range. Lastly, exfoliation is a morphological process; the material ablated

leaves on the target surface deep areas creating outgrowth microstructures around which are mechanically weak and are thermally decoupled and broken away upon two or more laser shots (Hoffman, Singh & Thomas, III, 1998). A simple method to reduce splashing -which does not impose restrictions to deposition and laser parameters-, is to use high density and smooth surface targets, an effective way is to polish the target surface before each deposition (Chrisey & Hubler, 1994).

Another disadvantage is the difficulty in depositing thin films on large area substrates; this presents a challenge due to the lack of uniformity of deposition over a large area (Chrisey & Hubler, 1994). However, this was solved, and few groups were able to deposit on a full wafer, by aligning the laser to hit the target in such a way where the center of the plasma plume reaches the outer edge of a rotating substrate. They were able to achieve a variation in thickness across the film below 5%, which is extremely small (Greer & Tabat, 1995). This approach has proved to be extremely effective for large area depositions, and it has been used to deposit films on substrates that are 12.5 cm and 15 cm in diameter.

Unlike other thin-film growth techniques, the major PLD concerns discussed above did not prevent it from progressing; these drawbacks presented engineering and fundamental challenges and were fortunately managed although not totally eliminated.

1.5. More About Pulsed Laser Deposition

There is much more to mention about PLD and the work done via this exceptional technique that have outstood from other film growth techniques. The ability of PLD to install several targets, have opened the opportunity to work with compound targets especially for deposition of multielemental oxides and nitrides and the fabrication of dielectric and ceramic films, although this presents its own difficulties

(Willmott & Huber, 2000). Besides, PLD has been coupled to a plasma (i.e. reactive) source, and the technique has been labeled Plasma Assisted PLD (PA-PLD) (Abi Akl, 2009), which generates excited and dissociative gas atoms such as oxygen which are far more reactive than neutral gas molecules; this enhances the proportion of the required gas atoms in the films.

Chapter 2

GENERAL PROPERTIES, LITERATURE REVIEW AND PLD GROWTH OF ZnO

2.1. Introduction

Zinc Oxide (ZnO) is a II-VI direct band gap semiconductor with gap energy of 3.37 eV (Sandana et al., 2009) i.e. in the UV range of the electromagnetic spectrum. It has been the focus of intense research for many years due to its potential applications in nano-scale electronics and optoelectronic devices. It is a multifunctional material and plays a major role in numerous devices such as ultraviolet light emitters including lasers, surface acoustic wave devices, varistors, light emitting diodes (LED), piezoelectric transducers and many others.

2.2. Crystal Structure of ZnO

Under ambient conditions, the thermodynamically stable phase of zinc oxide is the hexagonal wurtzite structure. This structure has a hexagonal unit cell with two lattice parameters ' a ' and ' c ', as shown in figure 2.1. In an ideal wurtzite structure the ratio c/a is 1.633 (Morkoç & Özgür, 2009). In addition, ZnO can also be found in zinc blende (Figure 2.2) and cubic structures (Figure 2.3), the latter known as the rocksalt crystal structure.

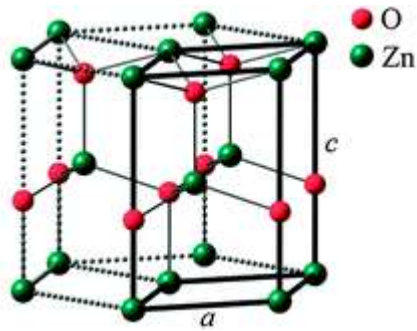


Figure 2.1: Wurtzite structure

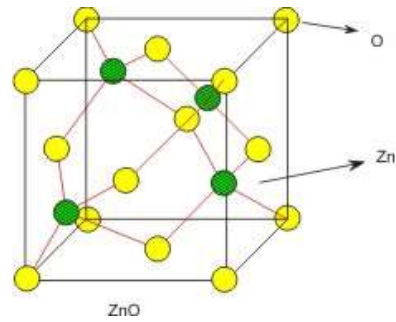


Figure 2.2: Zinc blende structure

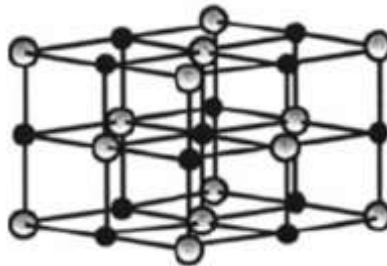


Figure 2.3: Rocksalt structure

The crystal structure of ZnO depends on the method of preparation and fabrication, temperature and pressure conditions. For example, upon oxidizing zinc vapor, zinc oxide crystallizes in zinc blende structure, and it is also stable only by growing it on substrates that have a cubic symmetry. However, ZnO takes a cubic crystal structure if prepared by the flash evaporation method. Cubic ZnO can be obtained at relatively high pressures.

2.3. Physical Parameters of ZnO

Some important physical parameters of ZnO are listed in table 2.1 below (Ali, 2011).

Table 2.1: Physical parameters of ZnO

Parameter	Value
Stable Phase at room temperature	Wurtzite
Lattice Parameters	'a' = 3.2495 Å ; 'c' = 5.2069 Å

Melting Point	1975°C
Static Dielectric Constant	8.656
Refractive Index	For wurtzite: 2.049 For zinc blende: 2.008
Energy Gap	3.37 eV, direct
Exciton Binding Energy	60 meV

2.4. Pulsed Laser Deposition of Zinc Oxide

Different methods and deposition techniques have been used to prepare ZnO in thin film and nanostructured form; these include Molecular Beam Epitaxy (MBE), Physical Vapor Transport (PVT), Chemical Vapor Deposition (CVD), Metalorganic Chemical Vapor Deposition (MOCVD) and sputtering. While these methods were successful in growing ZnO with good crystalline quality and optical properties, Pulsed Laser Deposition has emerged to be the technique of choice for the synthesis of ZnO as detailed below.

Sandana et al. (2009) have reported on the growth of ZnO nanostructures using three different deposition techniques; pulsed laser deposition, metal organic chemical vapor deposition and physical vapor transport. XRD investigations on the samples grown by these processes showed that the intensity of the XRD peak for the nano-ZnO grown by PLD is greatest and least for the one grown by MOCVD. Moreover, the rocking curve full width half maximum (FWHM) for the PLD-ZnO sample was smallest and largest for the MOCVD-ZnO sample. As a conclusion, ZnO nano-structures grown by PLD are better crystallized and highly oriented than those grown by MOCVD and PVT.

A vast amount of work has been done over more than one decade to produce ZnO thin films by PLD, and to determine the optimum growth conditions for the production of high quality films. In the Pulsed Laser Deposition technique, one can vary several parameters and study the effect of this variation on the deposited thin films. These parameters include choice of the substrate, substrate temperature, background gas, gas pressure, laser energy its repetition rate and wavelength.

Y.R. Jang et al. (2010) have reported on the PLD of zinc oxide thin films on silicon at temperatures up to 800°C and pressures ranging from 1 mTorr to 10 Torr. Highly oriented (along the c-axis) and highest crystalline quality films, as deduced from the strong (002) and (103) ZnO reflections and the strongest photoluminescence (PL) UV signal, were obtained at 1 Torr and 600°C. SEM revealed that at high oxygen pressures larger grains were obtained which is consistent with PL and XRD analysis.

M.A. Susner et al. (2014) have investigated the effect of oxygen pressure at 750°C of substrate temperature; under vacuum thin planar films are formed, depositions at intermediate pressures (75 mTorr) yielded the formation of nanoclusters, and high oxygen pressures (>250 mTorr) produced c-axis oriented nanowires. The crystallinity of the films improved with the increase in oxygen pressure (>250 mTorr) as the (002) XRD peak became more intense and dominant. At high oxygen pressures and with increasing the substrate temperature from 600°C to 750°C, the nanowire density decreases since their average radius increases. Longer depositions also yielded a decrease in the nanowire density and a significant increase in their height. A two-step process was then followed to increase the height without increasing the diameter of the nanowires, which involves depositing a “seed layer” at a low temperature followed by further deposition at a higher temperature; ZnO needles and porous nanostructures were observed.

D. Valerini et al. (2008) have reported PLD growth of ZnO nanostructures using different laser wavelengths, ArF (193 nm) and KrF (248 nm). Both showed good optical properties; a strong photoluminescence UV peak was observed, however, the films grown by ArF showed a better crystalline quality, as judged from width of the extremely strong (002) XRD peak revealed for both samples. Relatively smooth films were obtained using KrF laser, at 500°C and 700°C of substrate temperature and 1 Pa (7.5 mTorr) of oxygen pressure, however a rough surface was observed at 600°C. At this latter temperature, with increasing oxygen pressure in the range of 5 Pa to 100 Pa (0.75 Torr) nanorods are formed and a rougher surface is obtained. Finally, using the ArF laser and at 600°C hexagonal nanostructures and pencil-like structures were observed at 1 Pa and 100 Pa of oxygen pressure respectively.

M. Mosca et al. (2013) have studied ZnO deposition on quartz (SiO₂), sapphire (Al₂O₃) and Gallium Nitride (GaN) template. The narrowest photoluminescence UV peak was obtained for the film deposited on GaN and sapphire at 675°C of substrate temperature and 1 Pa of oxygen pressure, representing a good crystalline quality of the films. This was supported by XRD results, for both films on GaN and sapphire a strong and dominant (002) peak was observed in their XRD patterns indicating the preferential orientation of the layers along the c-axis; while the width of the rocking curve was narrowest for the film grown on GaN, the differences were minimal. The roughness of the film was lower for the one deposited on sapphire than that on GaN.

X. Sun and H. Kwok (1999) investigated the PLD of ZnO thin films at a fixed oxygen pressure of 10 mTorr and at various substrate temperatures up to 800°C. The optimum temperature to grow highly crystalline and highly c-axis oriented layers was 700°C, with a smallest FWHM rocking curve, and a clear and strong UV band-edge transition as revealed in photoluminescence scans.

A. Taabouche et al. (2013) have investigated the effect of glass and silicon (Poly-Si, Si (111) and Si (100)) substrates on the PLD of ZnO thin films, at a fixed oxygen pressure and substrate temperature of 1 Pa (7.5 mTorr) and 450°C, respectively. XRD patterns showed that the films are polycrystalline with a well orientation along the (103) rather than the expected (002) texture. For Si (100) and Si (111), only a strong (103) ZnO reflection was revealed. AFM images showed that the roughness was large for the film deposited on glass as compared to the one deposited on Poly-Si substrate. For the former sample (ZnO on glass) the calculated band gap was 3.23 eV.

Liu et al. (2006) have grown ZnO nanorods/grains with various diameters by PLD in an oxygen pressure range from 5 Torr to 20 Torr and substrate temperature range from 550°C to 750°C. All ZnO films were c-axis oriented, as deduced by the appearance of a strong (00*l*) (*l*=2, 4 and 6) in the XRD spectra. In this pressure and temperature range, the average grain size or diameter increased with the increase in oxygen pressure and substrate temperature respectively. Beyond the ranges no nanorods are formed but rather a continuous film is produced. The PL spectra of the ZnO films grown on sapphire showed a UV emission (~380 nm), as well as a green, strong and broad emission (~550 nm) which was attributed to structural defects in the samples such as oxygen vacancies and which increased with the increase in oxygen pressure and substrate temperature. Good optical properties -a minimum green emission- were obtained at 10 Torr and 550°C. On the other hand, ZnO thin films deposited on silicon at 10 Torr pressure and various temperatures but within the range showed a much stronger UV emission and a negligible green emission in the PL spectra.

B. Yang et al. (2009) fabricated ZnO nanostructures by PLD on different substrates, silicon (Si (100)), tungsten (W) and copper (Cu) at fixed substrate temperature and oxygen pressure of 600°C and 0.02 mTorr, respectively. SEM images

revealed that ZnO nanoneedles, with an average length of 1-5 μm , were formed on silicon Si (100), and transmission electron microscopy (TEM) showed that the diameter of their sharp tips and thick roots was $\sim 20\text{-}50$ nm and $\sim 50\text{-}100$ nm respectively. On tungsten W, ZnO nanowires were obtained with a length of 5-10 μm and diameter 50-70 nm. ZnO ‘micro-flowers’ on rough copper were formed with diameters 1-3 μm . Finally, ‘nanocrystalline particles’ were obtained on smooth copper wafer with a diameter of 300-500 nm. XRD investigations showed a preferred (002) orientation of the nanostructures formed on silicon, rough and smooth copper, unlike the nanowires deposited on tungsten, however, the FWHM of the (002) peak is smallest for the sample deposited on tungsten W and consequently this sample has the largest grain size. For ZnO micro-flowers formed on rough Cu the strain ϵ is negligible (-0.01%), however it has a value of -0.5% for nanostructures grown on Si and W substrates, which indicates a compressive strain between the surface and the nanostructures.

R. O’Haire et al. (2005) have reported PLD growth of ZnO nanostructures on three different orientations of sapphire substrates, a-, c- and r-plane sapphire and at a fixed substrate temperature and oxygen pressure of $\sim 700^\circ\text{C}$ and 10 Pa (~ 75 mTorr), respectively. Judging from XRD results and SEM images the growth on a-plane and c-plane sapphire produced (000 l) ($l=2, 4, 6\dots$)-oriented hexagonal nanodots, and nanoparticles with an average size of 300 nm and 150 nm, respectively (this latter sample deposited at 40 Pa) and (1120)-oriented ‘irregular’ nanostructures were formed on r-plane sapphire with a size of 300 nm existing atop a smoother ZnO layer. Finally, photoluminescence (PL) measurements showed a near band-edge emission at around 3.24 eV for all three samples, in addition to a broad blue emission band at around 2.85 eV for the samples grown on a- and c- sapphire substrates, while a broad green emission (~ 2.45 eV) was observed for the film grown on r-sapphire substrate.

Nie et al. (2008) prepared ZnO thin films by PLD of various thicknesses ranging from 4.8 nm to 280 nm, at a substrate temperature and oxygen pressure of 640°C and 20 mTorr respectively. All ZnO deposited films were c-axis oriented, XRD patterns of the samples displayed an intense and dominant (002) reflections. The strain was low for all these samples, and the out-of-plane grain size as well as the in-plane grain size increased to 70 nm and 150 nm with the increase in film thickness to 280 nm. SEM images confirmed the hexagonal structure of the ZnO nanocrystals formed. The band gap energies E_g were determined by the position of the exciton peak in the absorption spectra and its value was observed to increase with the decrease in the out-of-plane grain size, but for out-of-plane and in-plane grain sizes larger than 25 nm and 60 nm respectively, the band gap energy is almost the same.

Z.G. Zhang et al. (2007) have grown ZnO thin films via PLD on silicon at a fixed temperature of 400°C and under various oxygen pressures ranging from 0.003 Pa (0.02 mTorr) to 13 Pa (~98 mTorr). In this pressure range the FWHM of the (002) XRD peak, dominantly revealed for all samples, decreased with the increase in oxygen pressure. The optimum pressure value is 1.3 Pa (~10 mTorr) for producing highly crystalline and c-axis oriented films, as the (002) peak is the strongest and most intense. The thickness of the films showed an increase with the increase in oxygen pressure to 1.3 Pa, nevertheless, as the pressure is further increased to 13 Pa the thickness notably decreased. AFM measurements showed that the surface roughness of the films increased with the increase in oxygen pressure.

Table 2.2 below summarizes the work done by each author/s and at the optimal deposition conditions.

Table 2.2: Summary of the work done by many authors on the growth of high quality ZnO thin films by PLD

	Substrate (Temperature)	O ₂ Pressure	Analysis: Comments
Y.R. Jang et al.	Silicon (600°C)	1 Torr	XRD: Strong (002) and (103) peaks Strong PL UV signal SEM: larger grains at high O ₂ pressures
M.A. Susner et al.	Silicon (750°C)	>250 mTorr	XRD: among the peaks, (002) reflection is the strongest SEM: c-axis oriented nanowires
D. Valerini et al.	Silicon (600°C)	7.5 mTorr	XRD: Only extremely strong (002) peak Strong UV PL emission SEM: Relatively rough surface
M. Mosca et al.	Sappphire/GaN (675°C)	7.5 mTorr	XRD: c-axis oriented films, only (002) peak Narrowest PL UV line SEM: low roughness
X. Sun & H. Kwok	Sapphire (700°C)	10 mTorr	XRD: highly c-axis oriented layers Strong PL UV emission
A. Taabouche et al.	Silicon (450°C)	7.5 mTorr	XRD: Polycrystalline, strong (103) orientation
Liu et al.	Silicon (550°C)	10 Torr	XRD: Strong (00 <i>l</i>) (<i>l</i> =2, 4 and 6) peaks Strong PL UV signal, minimum green emission SEM: ZnO nanorods
B. Yang et al.	Silicon/ Rough Copper /tungsten (600°C)	0.02 mTorr	XRD: preferred (002) orientation for ZnO films on silicon and copper SEM: nanoneedles/micro-flowers/nanowires
R. O'Haire et al.	Sapphire (~700°C)	~75 mTorr	XRD: (00 <i>l</i>) oriented nanostructures PL Near UV band-edge emission
Nie et al.	Sapphire (640°C)	20 mTorr	XRD: intense and dominant (002) peak
Z.G. Zhang et al.	Silicon (400°C)	~10 mTorr	XRD: highly c-axis oriented films, only extremely strong (002) peak SEM: Relatively rough surface

Chapter 3

EXPERIMENTAL TECHNIQUES AND PROCEDURE

3.1. Introduction

In this chapter we describe the Pulsed Laser Deposition system used to grow the zinc oxide thin films and the different characterization techniques used to characterize their physicochemical properties, namely:

- X-Ray Diffraction (XRD)
- Scanning Electron Microscopy (SEM)
- Energy-Dispersive X-Ray Spectroscopy (EDX)
- Surface Profilometry
- UV-VIS Spectroscopy

3.2. PLD Experimental Setup

Figure 3.1 shows the PLD workstation setup used in this work. It consists of a high vacuum deposition chamber that can be pumped down to 10^{-7} mbar by a turbomolecular backed by diaphragm pumps. The chamber houses a target manipulator and a substrate holder; the target manipulator can hold up to four different targets and is mounted on rotary drives to allow for its rotation and toggling. The substrate holder is placed on top of the chamber (above the target) with a shutter and a heater that can go up to 950°C as measured by a thermocouple embedded in the substrate holder.

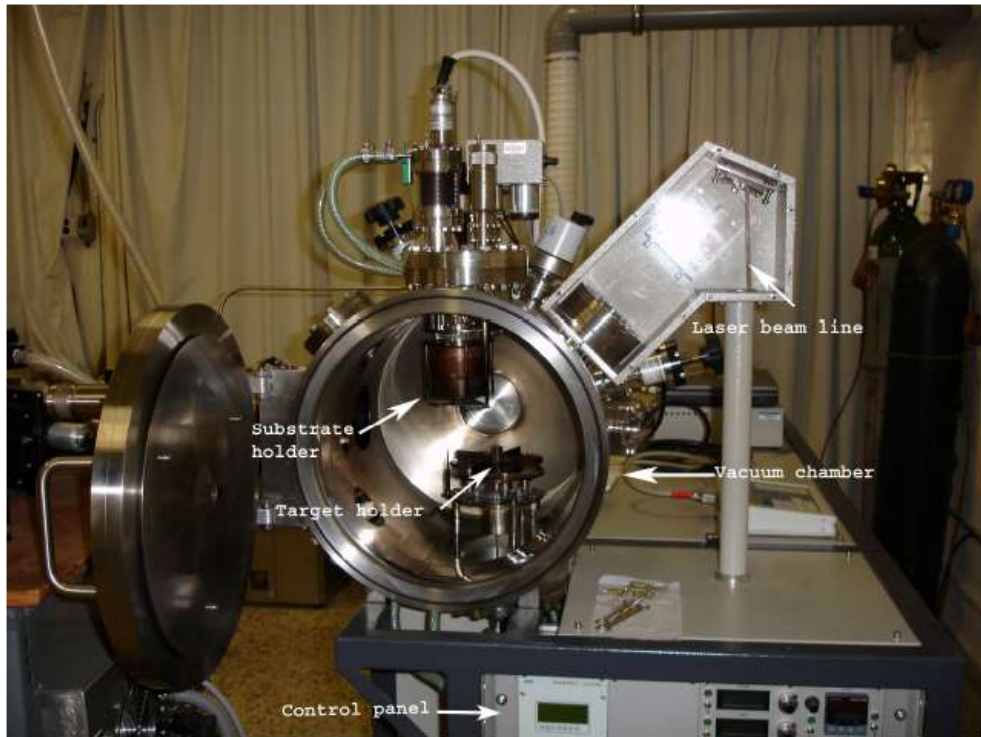


Figure 3.1: Pulsed Laser Deposition (PLD) setup

The laser used is a KrF excimer laser operating at 248 nm wavelength, 20 ns pulse duration with an adjustable repetition rate or frequency (1-50 Hz) and laser energy up to 700 mJ. A beam-line consisting of two mirrors and a lens guides and focuses the laser pulses on the target. Due to the high energy of the laser pulses, species such as atoms and ions will be ablated from the surface of the target in the form of a plasma plume, reaches the substrate and are deposited on it.

3.3. Characterization Techniques and Analysis of Thin Films

3.3.1. X-Ray Diffraction (XRD) Techniques and Analysis

The interatomic and interplanar distances in crystals are in the range of 0.15 to 0.4 nm which, in the electromagnetic spectrum, corresponds to the wavelength of x-rays. According to this, since both the interplanar distances and wavelength of x-rays

are comparable, constructive and destructive interference and diffraction phenomena should be observed when a crystal or molecular structure is exposed to x-rays. A crystal can be viewed as a set of lattice planes separated by a distance d_{hkl} , in which hkl are the Miller indices that defines the lattice planes. In x-ray diffraction, the sample is illuminated by x-rays that impinge them at an angle θ (Birkholz, 2005). The incident angle θ is varied leading to a variation in the intensity of the reflected waves. Constructive interference takes place when Bragg's law is satisfied

$$2d_{hkl} \sin \theta_B = \lambda \quad (3.1)$$

where, θ_B is the angle at which the peak is observed. This is geometrically visualized in figure 3.2.

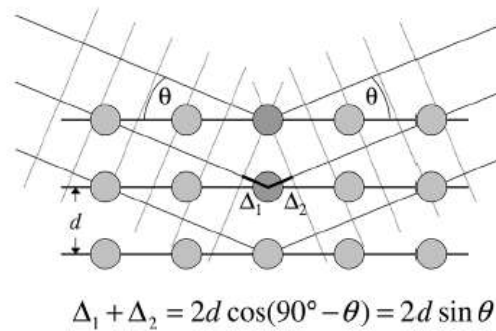


Figure 3.2: Bragg's law geometry

There are different geometries used in XRD, two of which we used in this work: Grazing Incidence and the Bragg-Brentano ($\theta/2\theta$) geometries. Both the grazing incidence x-ray diffraction (GIXRD) and the Bragg-Brentano (BB) are two major modes in thin film analysis. The difference between them will be explained briefly and will be understood by utilizing the geometry of scattering vector construction depicted in figure 3.3. Suppose that the incoming beam and the reflected one has wave vector K_0 and K respectively, then the scattering vector Q is defined as the wave vector difference $K - K_0$.

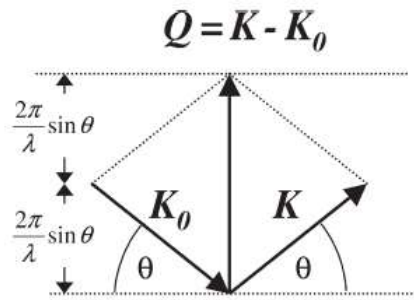


Figure 3.3: Geometry of scattering vector construction

It should be noted that K also represents the position of the detector

In the BB geometry, the XRD scan type is named locked coupled or $\theta/2\theta$, the x-ray beam is incident on the sample at a variable angle θ and the detector scans at the same angle. During the scan both the angle of the incident and the outgoing beams are continuously varied, but are equal at all times. In this geometry, the scattering vector Q has a fixed direction; it is always perpendicular to the surface of the sample, so only the planes that are parallel to the surface and perpendicular to Q will contribute to a peak in the XRD pattern (Birkholz, 2005).

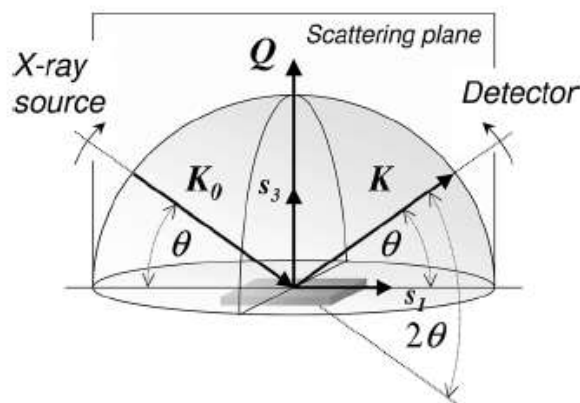


Figure 3.4: Schematic representation of $\theta/2\theta$ scan

The reason for naming the scan $\theta/2\theta$ is because the variation in the exit variable angle (2θ) is coupled the incident one (θ).

In GIXRD, the source or the incident beam of x-rays is held at a fixed and small angle θ ($\theta=1^\circ, 2^\circ$ or 3°), while the detector scans a certain angular range (2θ). Hence it should be emphasized that in this configuration the scattering vector Q changes both its magnitude and direction.

The X-ray measurements were performed using fully automated D8 Discover and D8 Advance diffractometers from Bruker AXS systems both available in our lab. In the D8 Discover Bruker diffractometer, the X-ray source consists of a ceramic Siemens tube operating at 40 kV with a current of 40 mA and emitting a $\text{CuK}\alpha$ radiation of wavelength $\lambda=1.5418 \text{ \AA}$. The diverging x-rays emitted from the x-ray tube are transformed into an intense parallel beam by a Göbel mirror (Bruker AXS XRD user's manual, 2010), which is free of K_β radiation eliminated by placing a nickel (Ni) filter. A sölér slit placed between the sample and the detector collimates the diffracted beam (Figure 3.5). However, the D8 Advance diffractometer does not have a Göbel mirror and was used in the Bragg-Brentano geometry.

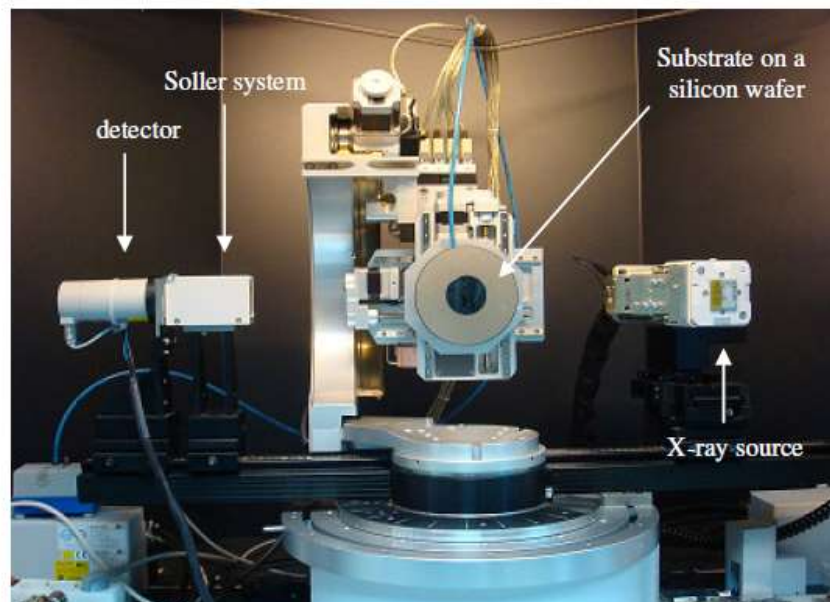


Figure 3.5: Bruker AXS D8 Discover X-ray diffractometer used

The parameters chosen for x-ray measurements of all samples are 0.2 s as the time per step, 0.02° as the increment and 25°-80° for the 2θ range.

The collected data and patterns were then analyzed by Bruker's EVA software. This software allows us to determine the crystal phase and structure of the thin films, by a search and match process and the aid of a database from the International Center for Diffraction Data (ICDD). An example of this search and match process is shown below in figure 3.6.

The black line represents the XRD signal from a ZnO sample and the blue vertical lines correspond to a matched pattern obtained from the database. The first numbers in parentheses correspond to the hkl indices, shown as (h,k,l) and the second number is the diffraction angle (2θ) of the XRD peak.

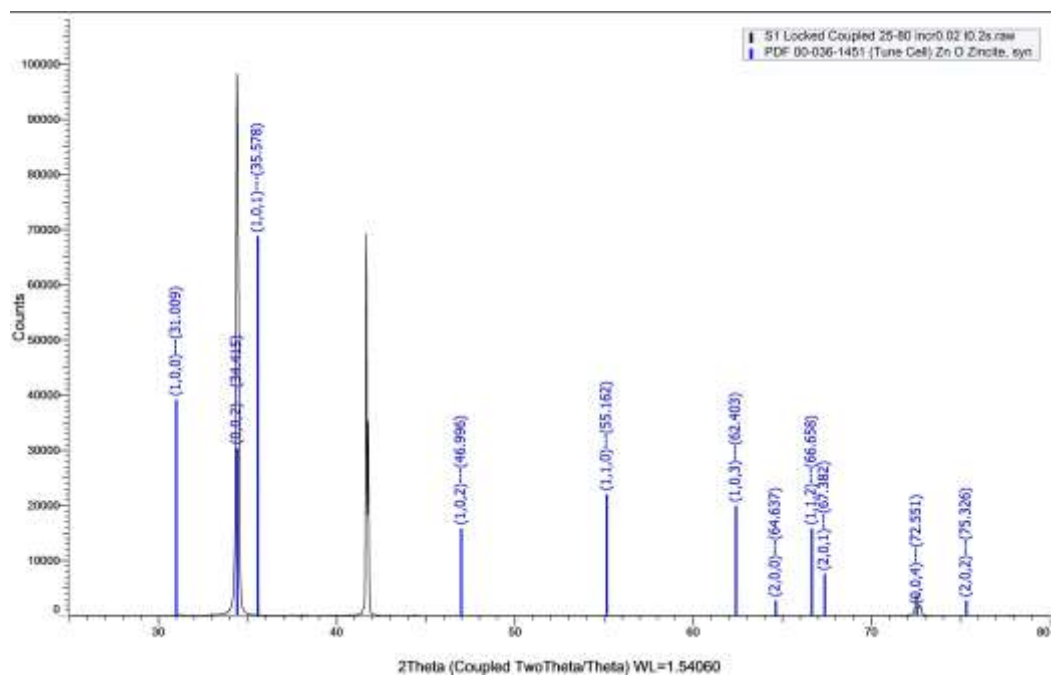


Figure 3.6: EVA match for XRD pattern of S1 sample

To measure the width w of the XRD peak (002) which allows us to determine the c value of our ZnO films and the average grain size h , slow scans were performed on

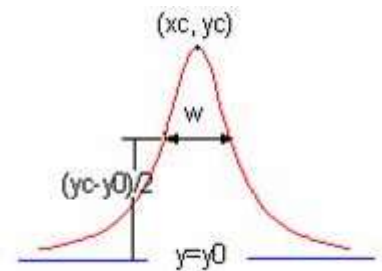
the (002) peak. The range of the XRD pattern was taken between 32° and 36°, the increment was chosen to be 0.002° and the time per step was 0.2s. A double Lorentzian fit was done on the (002) XRD peak of ZnO due to the presence of two peaks, one corresponding to K-alpha1 and the second to K-alpha2. The Lorentzian function is given by the following equation:

$$y = y_0 + \frac{2A}{\pi} \left(\frac{w}{4(x - x_c)^2 + w^2} \right)$$

where A is the area of the XRD peak,

w is the width of the peak, x_c is its position,

y_0 is the offset.



An example of the fit performed on the peak in the XRD diffractogram of one of the samples (S2 sample) is shown below:

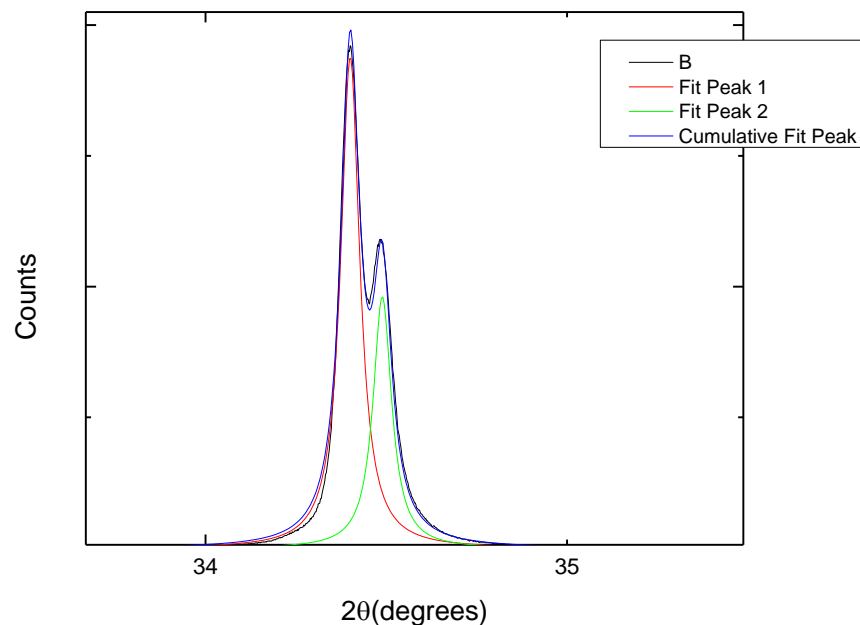


Figure 3.7: Double Lorentzian fit on the XRD peak

In most of the fits, a constraint was applied to the double Lorentzian function to obtain an exact and an accurate value of the position of the XRD peak and its width. The constraint is forcing the intensity of K-alpha1 to be twice the intensity of K-alpha 2 ($A_1=2*A_2$) as it should be in theory.

3.3.1.1. Full Width Half Maximum (FWHM) of the XRD Peak w

The fit will provide us with two values of the width, a width for K-alpha1 peak and a width for K-alpha 2. The average of the two values is reported. The error on w is the standard error obtained from the double Lorentzian fit via Origin software, and has been referred to it to appropriately report the values.

3.3.1.2. Lattice Constant c

Moreover, from the fit we can get the position of both peaks which will allow us to calculate the lattice constant c . From literature reviews and our XRD patterns the samples have a wurtzite hexagonal crystal structure. For a hexagonal crystal system, there are two main lattice constants namely a , and c which are related to each other and to the interplanar distance d by the following equation (Birkholz, 2005):

$$\frac{1}{d_{hkl}^2} = \frac{4}{3} \frac{h^2 + hk + k^2}{a^2} + \frac{l^2}{c^2}$$

The dominant peak in the XRD pattern is the (002) ($h=k=0$) and therefore the interplanar distance between the (002) planes will be:

$$\frac{1}{d_{(002)}^2} = \frac{4}{c^2} \Rightarrow c = 2d_{(002)}$$

Using Bragg's equation we can calculate d and consequently c :

$$2d_{(002)} \sin \theta_{(002)} = \lambda$$

Therefore,

$$c = 2d_{(002)} = \frac{\lambda}{\sin \theta_{(002)}}$$

where $\theta_{(002)}$ is the diffraction angle of the (002) peak. Given the wavelengths of K-alpha1 and K-alpha2 lines to be 1.54056Å and 1.54439Å respectively (Smyth & McCormick, 1995), and given the position $2\theta_{(002)}$ of both peaks from the fit we can calculate two values of the lattice constant c and their average value is then reported.

The increment (0.002°) chosen in the slow XRD scans contributes mainly to the error on the 'c' value. From error analysis and propagation of error, the error on c,

$$\alpha_c \text{ is given by: } \alpha_c = \sqrt{\left(\frac{\partial c}{\partial \lambda} \alpha_\lambda\right)^2 + \left(\frac{\partial c}{\partial \theta} \alpha_\theta\right)^2}$$

The wavelengths of K-alpha1 and K-alpha2 are known to a high accuracy and hence their error α_λ is negligible compared to the error on θ .

Therefore:

$$\alpha_c = \left| \frac{\partial c}{\partial \theta} \alpha_\theta \right| = \left| \frac{\lambda \cos \theta}{(\sin \theta)^2} \alpha_\theta \right| = \left| \frac{c \cos \theta}{\sin \theta} \alpha_\theta \right|$$

where $\alpha_\theta = 0.002^\circ$ must be in radian measure.

Knowing θ and the 'c' value for each sample, the error α_c is calculated and it takes a value of 0.0006 Å.

3.3.1.3. The Strain ε

The strain by definition is a dimensionless quantity, as it is the ratio of the variation in the length to the original length. Specifically in this work, we report the variation in the lattice constant 'c' of our thin films. As a percentage it is given by:

$$\varepsilon = \frac{\bar{c} - c_{theoretical}}{c_{theoretical}} \times 100$$

It can be either positive or negative.

$\varepsilon > 0$ i.e. $\bar{c}_{thin\ film} > c_{target}$, the strain is tensile.

$\varepsilon < 0$ i.e. $\bar{c}_{thin\ film} < c_{target}$, the strain is compressive.

3.3.1.4. Average Grain Size h

Finally, to estimate the average grain size h in our samples, we have used the known Scherrer equation for cylinders. For that matter, we assume that the crystals are cylindrical since they only show reflections from the (002) planes.

Based on the work of Langford and Louër (1982), the quantity required to calculate Scherrer constant is the common-volume function, which is the volume between the crystallite and its “ghost”, shifted a distance t parallel to the diffraction vector (in the direction $[hkl]$). For a cylinder of height H and diameter D this volume is given by the following equation:

$$V(t) = \frac{1}{2} D^2 (H - t \cos \varphi) [\arccos \alpha - \alpha(1 - \alpha^2)^{1/2}] \quad (3.2)$$

The normalized volume function may be expressed as:

$$\frac{V(t)}{V(0)} = \frac{2}{\pi} (1 - T\alpha) \left[\arccos \alpha - \alpha(1 - \alpha^2)^{1/2} \right] \quad (3.3)$$

where:

φ is the angle between the normal of the diffracting plane and the cylinder axis

t is the displacement of the ‘ghost’ crystallite.

$$\alpha = \frac{t}{D} \sin \varphi$$

$V(0)$ is the volume of the cylinder

$$T = \frac{\tan \Phi}{\tan \varphi} \text{ and } \Phi = \tan^{-1} \left(\frac{D}{H} \right)$$

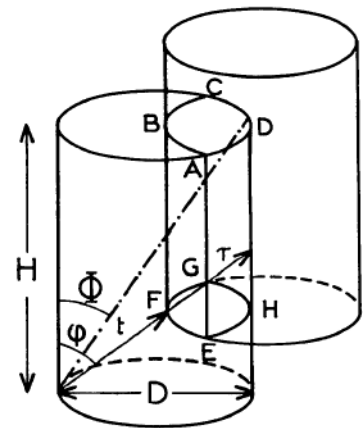


Fig. 1. Volume ABCDEFGH common to a cylinder and its 'ghost' displaced a distance t perpendicular to the diffracting planes.

Φ determines the upper limit of φ , so $0 \leq \varphi \leq \Phi$

Scherrer constant K is a dimensionless quantity which is used to determine the size of the crystallite. In general, it is defined as the ratio between the true size and the apparent size of the crystallites in the direction of the normal to the diffracting planes

$$K = \frac{\text{'true' size}}{\text{apparent size}} = \frac{p}{\varepsilon}$$

The breadth B of a small-crystallite profile yields an apparent size ε_B , which is a weighted average of the size (thickness) of the crystallite in the direction perpendicular to the diffracting planes, therefore Scherrer constant K_B for cylindrical crystallites is given by:

$$K_B = \frac{\gamma D}{\varepsilon_B}, \text{ where } \gamma = \left(\frac{\pi H}{4 D}\right)^{1/3}$$

Two ways can be used to find the Scherrer constant:

- The half-width (FWHM) Scherrer constant, K_w where the apparent size is given by the full-width at half-maximum intensity (FWHM) of the diffraction peak ε_w . However, this cannot be derived analytically.
- The integral-breadth Scherrer constant K_β .

The integral-breadth apparent size ε_β is given by:

$$\varepsilon_\beta = \frac{2}{V(0)} \int_0^\tau V(t) dt \quad (3.4)$$

where:

$V(0)$ is the volume of the cylinder

τ is the maximum thickness (length) of the crystallite in the direction normal to the diffracting plane i.e. in the direction of the diffraction vector and can be expressed in terms of the dimensions of the crystallite. It is given by: $\tau = H \sec \varphi$

In our case, since we only have reflection from the (002) and (004) planes then the angle $= 0 \Rightarrow \alpha = 0$, $\tau = H$, $\arccos(0) = \frac{\pi}{2}$. Substituting in equation (3.3) above gives the following:

$$\frac{V(t)}{V(0)} = \frac{2}{\pi} \left[\frac{\pi}{2} \right] = 1$$

Solving integral (3.4) leads to the following:

$$\varepsilon_{\beta} = 2 \int_0^H \frac{V(t)}{V(0)} dt = 2 \int_0^H dt = 2H$$

The apparent size is proportional to the inverse of the integral breadth β (which is defined as the ratio of the peak area (area under the curve) to the peak maximum (peak height))

$$\varepsilon_{\beta} = \frac{\lambda}{\beta \cos \theta} \quad (3.5)$$

where θ is the diffraction angle.

From the Lorentz fit we can find the integral-breadth β , it is given by:

$$\beta = \frac{\pi w}{2} \text{ where } w \text{ is the FWHM of the diffraction peak}$$

Substituting $\beta = \frac{\pi w}{2}$ and $\varepsilon_{\beta} = 2H$ in equation (3.5) we arrive at the following equation of H which resembles the average height of the grains (crystallites):

$$h = H = \frac{\lambda}{\pi w \cos \theta}$$

In our determination of H or h we took the average value of h (average value between h obtained from Kalpha1 and h obtained from Kalpha2).

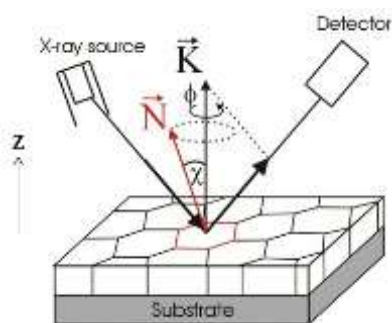
We convert w to radians so the equation becomes:

$$h = \frac{\lambda}{\pi^2 \frac{w}{180} \cos(x_c/2)} \quad (3.6)$$

This equation (3.6) relates the size of the crystallites or grains to the broadening of the XRD peak.

3.3.1.5. Rocking Curves (RC)

A rocking curve is a plot of x-ray intensity versus theta (θ) or the incident angle i.e. the angle between the sample and the incident x-ray beam. In a rocking curve scan the detector is set and fixed at a specified Bragg angle (2θ) and the sample is tilted about its theta axis. The rocking curves of all our samples have been obtained using the D8 Discover X-Ray diffractometer. Before each RC scan, Z and Chi alignments of the samples were carried out; the resulting Z and Chi (χ) values were fixed, the range of the scan was $15^\circ - 19^\circ$, and the scan parameters were chosen to be 0.002° as the increment and 0.5s for the time per step.



For all our samples, as will be shown and discussed in Chapter 4, the XRD patterns of the samples show a strong peak at a Bragg angle $\sim 34^\circ$, hence after taking the exact value, this was the angle to be fixed in the RC scan, then theta will be $\sim 17^\circ$, and this is the reason for choosing the scan range $15^\circ - 19^\circ$.

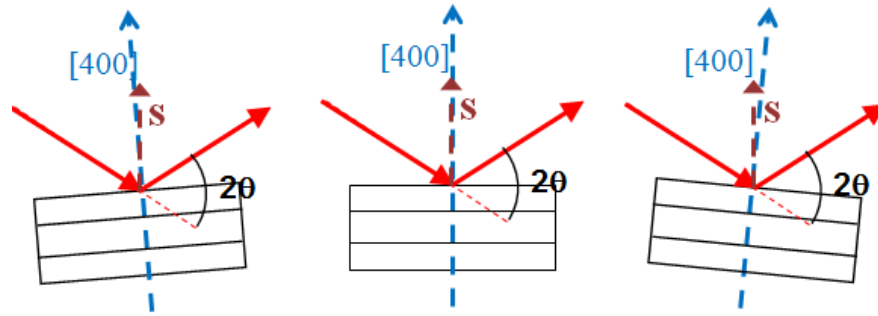


Image 3.1: Schematic representation of a rocking curve scan

Rocking curves are significantly investigated because they are used not only to study the crystallinity of structured materials and thin films, but also to study defects embedded in them such as dislocation density, inhomogeneity, misorientation, curvature as well as lattice mismatch and layer thickness (Speakman, 2012).

To measure the FWHM rocking curve, denoted by ω_r , Gaussian and Lorentz functions were used as the fitting functions. The broadening of the peak is affected by two different sources: instrumental contributions and sample contributions; the latter including micro-strain, and the grain/crystallite size (Barnes et al., 2006). It was noticed that the rocking curve peak follows a Lorentzian shape for FWHM (ω_r) less than 0.25° , and follows a Gaussian shape for FWHM (ω_r) larger than 0.25° .

3.3.2. Surface Profilometry

The surface profilometer is a stylus profilometer which is a technique used to measure the thickness of thin films by monitoring the mechanical movement of the stylus as it scans the region of a film-substrate step (Abi Akl, 2009) (figure 3.8). To generate this step, a strip of aluminum foil was used as a mask to cover a small area of the substrate.

An XP series stylus profilometer from Ambios technology was used in our measurements. The force of the stylus was chosen for all scans to be 8 mg, for which we obtained a clear step. The scan speed was set to 0.15 mm/s and the scanning length was adjusted between 4 and 6 mm depending on the scanned region. All these parameters are adjusted via the Ambios XP software.

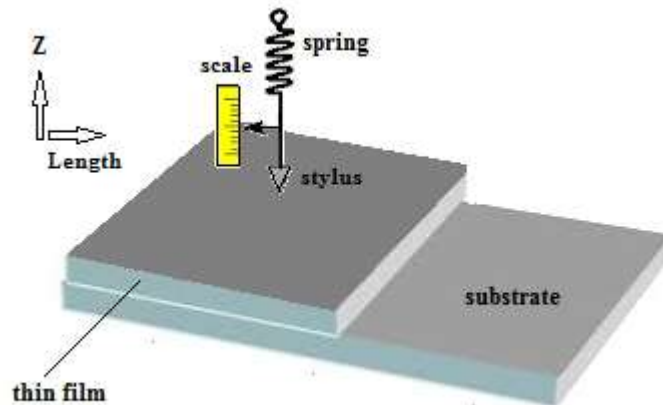


Figure 3.8: Schematic representation of the stylus profilometer

Data measurements by the profilometer will be provided as a graph revealing the Z position or vertical displacement of the stylus in angstroms (\AA) as a function of the horizontal displacement or length it scans on the surface of the sample. An example of the graph obtained is shown in figure 3.9.

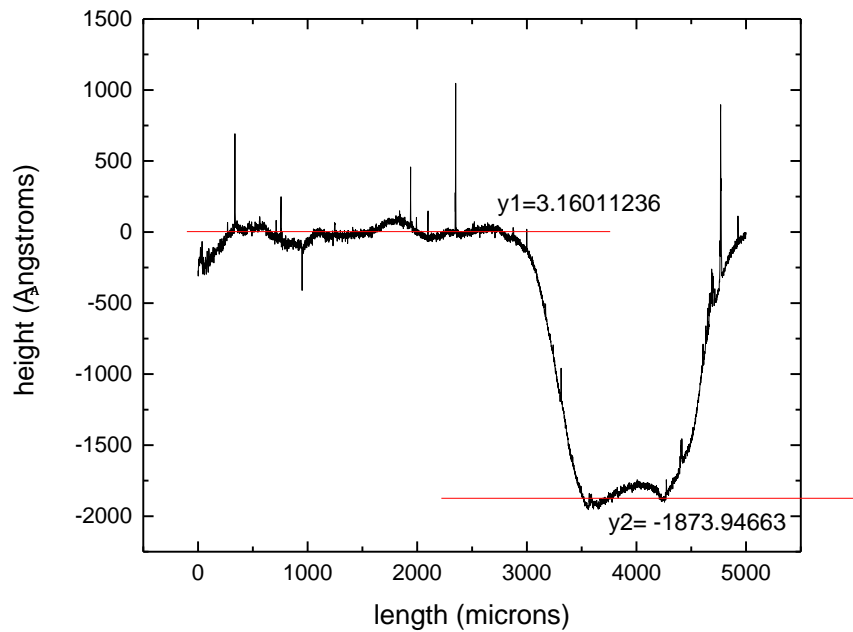


Figure 3.9: Line profile of S11 sample

The thickness of the thin film is the absolute value of the difference between y_1 and y_2 ; $h = |y_1 - y_2|$. Each sample was scanned at several positions of the film-substrate step, the procedure shown in figure 3.9 was applied, the value of h was calculated for each scan and the thickness of the thin film was computed and reported as the average value of the h values obtained. As a result the error on the thickness resembles the root-mean-square (rms) error on h .

3.3.3. Scanning Electron Microscopy (SEM)

Since the 1930s electron microscopy has proved to be a powerful tool for characterizing the shape and size of nanostructures. Similar to optical microscopy, it provides the user with an image of the nanomaterial under investigation. Fortunately, the advantage of electron microscopy over optical microscopy is that the resolution

provided by the former is much higher, as low as 0.1 nm, which makes it suitable for imaging nanostructures, whereas the resolution of the latter one is hundreds of nanometers (~ 200 nm), based on the fact that the resolution of a microscope is determined by the wavelength of the radiation used for imaging; it is directly proportional to the wavelength. In electron microscopes, an electron beam, with electron energies of few thousand electron volts (~ 3600 eV) are used, this is thousand times greater than the photon energy (2-3 eV) in case of optical microscopes. So, with this energy of electrons the wavelength can be computed, and taking into consideration aberrations of the electron lens and the final aperture the resolution that can be achieved is a tenth of a nanometer (Prasad, 2004).

Scanning electron microscopy is one of the major electron microscopic methods in which a focused electron beam from an electron gun scans over and across the sample. The electron beam is focused by condenser lenses, beneath which a set of scanning coils deflects the electron beam that is allowed to scan the surface, residing at each point for few microseconds. The deflected electrons called the secondary or back-scattered electrons which are in charge of imaging are captured by a detector. The detector converts each into a light flash which produces electrical pulses and which, in turn, are amplified by a signal amplifier. These amplified signals modulate the brightness of each spot in a two or a three dimensional picture which is displayed on a cathode ray tube (CRT). Hence, every spot on the CRT corresponds to a spot on the surface of the sample. The brightness of a certain area in a SEM image is a measure of the intensity of the secondary electrons detected; the surface areas directly facing the detector will appear bright, while holes and cavities will be pictured as dark areas (Prasad, 2004).

The MIRA 3 series scanning electron microscope, which is available in the CRSL, was utilized for imaging the surface of our thin films. It is a family of fully PC-controlled scanning electron microscopes equipped with a Schottky Field emission electron gun designed for high vacuum or variable pressure operations.

Three factors control the quality of the images provided, they are the spot size, the aperture angle and the beam intensity of the electron beam. The spot size is considered to be circular, with an intensity described by a Gaussian distribution. It is smaller at shorter working distances. The incident electron beam is cone-shaped, with a cone angle determined by the aperture angle of the objective lens; the narrower the cone, the higher the depth of focus. Finally the beam intensity is proportional to the number of electrons passing in a defined area and time.

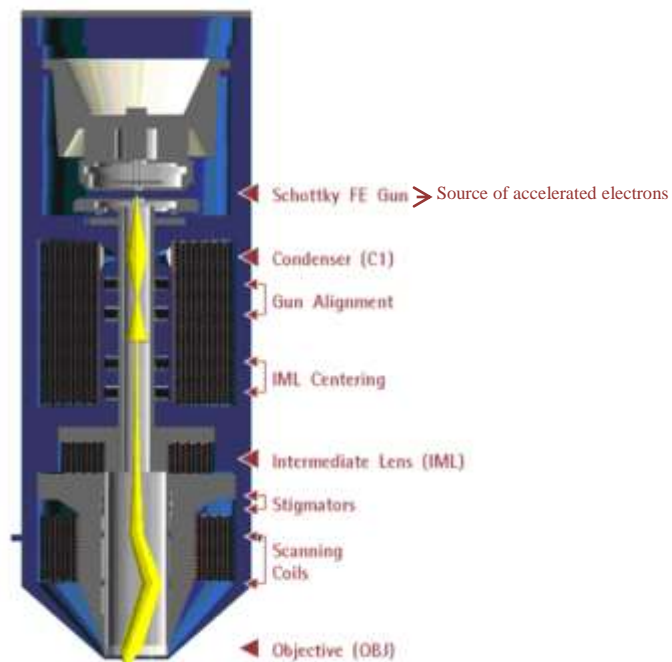


Figure 3.10: Cross section representation of the optical elements of the SEM

As a brief description of the main components making up the microscope, the **condenser** is a strong magnetic lens that determines and controls the number of electrons passing through the diaphragm. The **gun centering or alignment** is composed of a system of electromagnetic deflection coils whose role is to tilt the electron beam emitted from the electron gun to enter the axis of the optical system of the column. The **IML lens** is a magnetic lens used to change the aperture of the beam entering the objective lens and the **stigmators coils** is a component used to reduce the astigmatism of the beam in all modes. Finally, the **objective lens** is a magnetic lens that forms the resulting electron beam (MIRA 3 series SEM user's manual, 2011).

The sample was installed in the SEM chamber that was then evacuated by pumping it to a pressure of 0.005 Pa. The high voltage, the accelerating voltage of the electrons between the cathode (electron gun) and the anode (sample stage), was set at 5 kV. At first, for each scan auto gun centering was applied, in order to obtain high quality images. The basic SE (secondary electron) detector was chosen and the resolution mode was selected to take topographic images of our samples; it is the basic and most common mode characterized by its high resolution and a low depth of focus. Next, the magnification and the working distance (WD), which is the distance where the electron beam focuses, were adjusted to get a clear image after which the working distance and the Z position of the sample stage (WD & Z) was lowered (down to 5 mm) to get a more resolved image; WD & Z move simultaneously. Further enhancement of the image was done by adjusting WD & Z with small increments and the stigmators, in addition to centering the column manually. By selecting manual column centering the image starts wobbling, periodically changing its working distance, and to achieve a clear image we had to manually minimize the movement of the image by the trackball on the Pad panel. The manual column centering is suitable for high magnification

images. Note that centering of the microscope, the gun or the column, and the adjustments made to the stigmators and the working distance is electronic and fully controlled by the PC.

3.3.4. *Energy-Dispersive X-Ray Spectroscopy (EDX)*

The X-ray energy dispersive microanalyzer is always coupled to a scanning electron microscopy (SEM). It is a basic technique, a non-destructive and a quick method used to identify the chemical composition of the sample investigated, by making use of characteristic X-rays generated by an accelerated electron beam striking the surface of the sample. When electrons with sufficient energy strike atoms (such as atoms of the sample), electron in an inner shell of the atom is excited and with high enough energy the electron in this shell will be expelled creating a hole in its place. To minimize the energy, the hole has to be filled up by an electron from a higher energy shell. By this transition a photon will be emitted in the form of X-rays. An energy dispersive spectrometer monitors the number and energy of x-rays emitted from the sample, and since the energy of these emitted x-rays is linked to the difference in energy between the higher and the lower shells i.e. to the atomic structure, the chemical composition of the sample is determined.

To investigate the elemental composition of our sample the INCA energy system was employed, which consists of a PC loaded with INCA energy software, an x-stream module to control x-ray acquisition and an EDS detector to detect x-rays (INCA Energy EDX operator manual, 2006).

As an important notice in order not to damage the system the LED inside the SEM chamber should be turned off and the working distance (WD & Z) of the SEM should be set at 15 mm before turning the INCA software on and starting the data acquisition.

The results provided to the user are reported in different forms one of which is depicted in the image below (Image 3.2) and which was selected for our purposes.

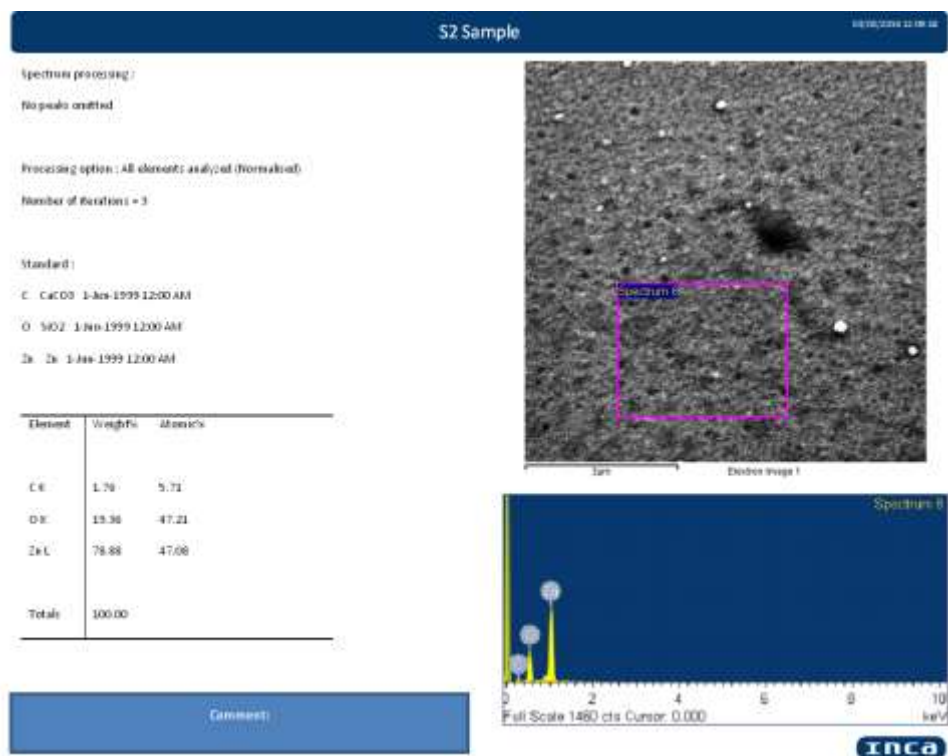


Image 3.2: Elemental composition report by INCA of one of our samples (S2 sample)

INCA allows data and spectrum acquisition of different regions selected by the user. Also note that with increasing the high voltage (HV: 10-15 kV), electrons can penetrate deep into the sample and information about the elemental composition of the bulk of the sample is acquired.

3.3.5. UV-VIS Spectroscopy

The UV-VIS spectroscopy technique is an optical characterization technique that uses ultraviolet, visible and sometimes near infrared (NIR) radiation to study electronic transitions between the atomic and molecular energy levels. It can be referred to as either absorption or reflectance spectroscopy in the UV-VIS-NIR spectral range.

This kind of technique has proven to be an efficient technique in determining the band gap of the sample under study. For our objectives we have chosen reflectance spectroscopy, and it involves the study of reflected or scattered light from the surface of a sample as a function of wavelength.

Our UV-VIS reflectivity measurements were done using the ARN-475 Model UV-VIS spectrometer, available in the CRSL lab, which enables measurements in a broad wavelength range from 200 nm to 2000 nm. Light from the spectrophotometer is always polarized by a grating. In our case the reflectivity spectrum was scanned from 300 nm to 1500 nm, so it is more in the ultraviolet, visible and near infrared regions and it can be referred to as UV-VIS-NIR spectroscopy. This spectrometer allows one to measure the absorbance, transmittance, absolute and relative reflectance.

The reflectance unit consists of an integrating sphere, a solid sample holder attached to a detector. The selection between absolute and relative reflectance relies on the sample under investigation, and the difference between them is that the angle of incidence in the former can be changed by moving the detector in an angular range from 5° to 90° . However, in relative reflectance the sample is mounted on the rear of the integrating sphere (at a fixed 90° angle) to which the detector is attached ().

The reflectance measuring unit is attached to the spectrometer and the baseline is measured at an angle of incidence of 90° , for the purpose of eliminating any effects and reflections from the unit. For our purposes we have selected relative reflectance to measure the reflectivity spectrum of our samples.

3.3.5.1. Kramers-Kronig Method

Kramers-Kronig relations are mathematical relations used to relate the real and imaginary part of any complex function which is analytic in the upper half of the

complex plane. These relations are used to determine the real part from the imaginary part, or vice versa, of response functions in physical systems. Hence, they can be applied to study complex optical functions describing light matter interaction such as susceptibility, the dielectric function, complex index of refraction, reflectivity... In reflection spectroscopy, Kramer-Kronig (K-K) relations are applied to relate the measured reflectance and the phase change of the reflectivity (Abu Amer, 2015).

For the K-K relations to be applied, a complex response function $\alpha(\omega) = \alpha_1(\omega) + i\alpha_2(\omega)$ must satisfy the following conditions:

1. $\alpha(\omega)$ must be analytic in the upper half of the complex plane.
2. The real part $\alpha_1(\omega)$ must be an even function and $\alpha_2(\omega)$ must be an odd function.
3. The complex function must vanish at very high wavenumbers, i.e. the integral $\frac{\alpha(\omega)}{\omega}$ along a semicircle with infinite radius in the upper half of the complex plane vanishes.

To derive the K-K relations, we choose a complex function $\alpha(\omega)$ satisfying the above conditions, and we begin with Cauchy's residue theorem. Since α is analytic in the upper half of the complex plane, then the function $\frac{\alpha(s)}{s-\omega}$ is also analytic and Cauchy's theorem states that its integral on a closed contour shown in figure 3.11 is zero.

$$\oint \frac{\alpha(s)}{s-\omega} ds = 0$$

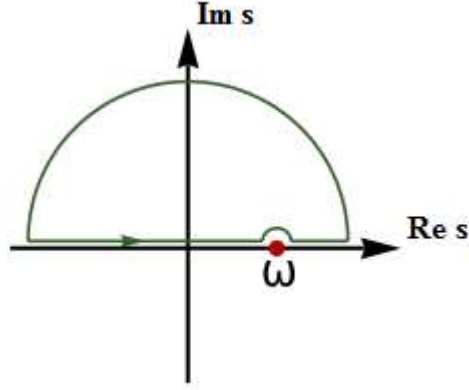


Figure 3.11: Integral Contour for deriving K-K relations

The integral can be decomposed into three parts; first we take the integral along the length of the semicircle segment in the upper part of the complex plane, but this integral vanishes, since in this limit $\alpha(\omega)$ vanishes faster than $1/|\omega|$. Second, the integration is taken along the real axis and it is given by:

$$P \int_{-\infty}^{+\infty} \frac{\alpha(s)}{s - \omega} ds$$

where P is referred to as the principle part of the integral

The third region for integration is taken along the small semicircle at the pole $s = \omega$, and the integration is given by the theory of residues to be equal to $-i\pi\alpha(\omega)$.

Combining the results we get:

$$\int \frac{\alpha(s)}{s - \omega} ds = P \int_{-\infty}^{+\infty} \frac{\alpha(s)}{s - \omega} ds - i\pi\alpha(\omega) = 0$$

The expression of $\alpha(\omega)$ is given by:

$$\alpha(\omega) = \frac{1}{i\pi} P \int_{-\infty}^{+\infty} \frac{\alpha(s)}{s - \omega} ds \quad (3.7)$$

Equation (3.7) is the compact form of Kramers-Kronig relations.

Recalling $\alpha(\omega)$ is a complex function having the form: $\alpha(\omega) = \alpha_1(\omega) + i\alpha_2(\omega)$

Therefore,

$$\alpha_1(\omega) + i\alpha_2(\omega) = \frac{1}{i\pi} P \int_{-\infty}^{+\infty} \frac{\alpha_1(s) + \alpha_2(s)}{s - \omega} ds$$

$$\alpha_1(\omega) + i\alpha_2(\omega) = \frac{-iP}{\pi} \int_{-\infty}^{+\infty} \frac{\alpha_1(s)}{s - \omega} ds + \frac{P}{\pi} \int_{-\infty}^{+\infty} \frac{\alpha_2(s)}{s - \omega} ds$$

$\alpha_1(\omega)$ and $\alpha_2(\omega)$ are expressed as:

$$\alpha_1(\omega) = \frac{P}{\pi} \int_{-\infty}^{+\infty} \frac{\alpha_2(s)}{s - \omega} ds \quad (3.8)$$

$$\alpha_2(\omega) = \frac{-P}{\pi} \int_{-\infty}^{+\infty} \frac{\alpha_1(s)}{s - \omega} ds \quad (3.9)$$

Integral rearrangements can be done to equations (3.8) and (3.9)

Split the integral into two parts:

$$\alpha_1(\omega) = \frac{P}{\pi} \int_{-\infty}^0 \frac{\alpha_2(s)}{s - \omega} ds + \frac{P}{\pi} \int_0^{+\infty} \frac{\alpha_2(s)}{s - \omega} ds$$

Flip the first integral and replacing s by $-s$, and remember that $\alpha_2(s)$ is odd so,

$$\alpha_2(-s) = -\alpha_2(s)$$

$$\alpha_1(\omega) = \frac{P}{\pi} \left(\int_0^{+\infty} \frac{\alpha_2(s)}{s + \omega} ds + \int_0^{+\infty} \frac{\alpha_2(s)}{s - \omega} ds \right)$$

Take common denominator:

$$\alpha_1(\omega) = \frac{P}{\pi} \left(\int_0^{+\infty} \frac{\alpha_2(s) * (s - \omega) + \alpha_2(s) * (s + \omega)}{(s - \omega)(s + \omega)} ds \right)$$

$$\Rightarrow \alpha_1(\omega) = \frac{P}{\pi} \left(\int_0^{+\infty} \frac{\alpha_2(s) * 2s}{s^2 - \omega^2} ds \right)$$

This equation finally gives the first relation of Kramers-Kronig:

$$\alpha_1(\omega) = \frac{2P}{\pi} \int_0^{+\infty} \frac{s * \alpha_2(s)}{s^2 - \omega^2} ds \quad (*)$$

Similarly for $\alpha_2(s)$ we work out the same procedure; splitting the integral into two parts and now using the condition that $\alpha_1(s)$ must be even i.e. $\alpha_1(-s) = \alpha_1(s)$, we get:

$$\alpha_2(\omega) = \frac{-P}{\pi} \left(\int_0^{+\infty} \frac{-\alpha_1(s)}{s + \omega} ds + \int_0^{+\infty} \frac{\alpha_1(s)}{s - \omega} ds \right) \quad (3.10)$$

Adjusting equation (3.10) by taking common denominator results in the second relation of Kramers-Kronig:

$$\alpha_2(\omega) = \frac{-2\omega P}{\pi} \int_0^{+\infty} \frac{\alpha_1(s)}{s^2 - \omega^2} ds \quad (**)$$

The K-K relations can be used to analyze the reflectance data acquired. These relations allow us to relate the amplitude of the reflectance to the phase change between the incident and reflected signal. The ratio of the intensity of the reflected radiation to the incident one is known as Fresnel coefficient of reflectivity r where:

$$r = \frac{A_{reflected}}{A_{incident}} = \rho(\omega)e^{i\varphi(\omega)} = \rho(\omega) \cos \varphi(\omega) + i\rho(\omega) \sin \varphi(\omega)$$

The reflectivity R is $R = rr^* = \rho(\omega)^2$

Where ρ is the amplitude and φ is the phase change

$$\ln r(\omega) = \ln \rho(\omega) + \ln e^{i\varphi(\omega)}$$

$$\ln r(\omega) = \ln \rho(\omega) + i\varphi(\omega)$$

This has the form:

$$\alpha = \alpha_1 + i\alpha_2$$

$$\alpha_1 = \ln \rho(\omega) = \frac{\ln R(\omega)}{2} \text{ and } \alpha_2 = \varphi(\omega)$$

Hence Kramers-Kronig relations can be applied to find the phase change from the reflectance:

$$\varphi(\omega) = \frac{-\omega P}{\pi} \int_0^{+\infty} \frac{\ln R(s)}{s^2 - \omega^2} ds$$

This can be written in a more useful form:

$$\varphi(\omega) = \frac{-1}{2\pi} \int_0^{+\infty} \left(\ln \left| \frac{s + \omega}{s - \omega} \right| \frac{d \ln R(s)}{ds} ds \right) \quad (3.11)$$

Once the reflectance of a certain material is known the phase change can be determined by equation (3.11).

Moreover, the coefficient of reflectivity is also given by:

$$r(\omega) = \frac{\sqrt{\varepsilon(\omega)} - 1}{\sqrt{\varepsilon(\omega)} + 1}$$

The complex refractive index N and the dielectric function ε are related by the following:

$$N = \sqrt{\mu * \varepsilon(\omega)}$$

where μ is the material's relative permeability, and for non-magnetic materials $\mu=1$

$$\text{So, } N = \sqrt{\varepsilon} \text{ or } N^2 = \varepsilon$$

Taking $N = n(\omega) + ik(\omega)$ and $\varepsilon(\omega) = \varepsilon_1(\omega) + i\varepsilon_2(\omega)$

n is the real part of the complex index of refraction N , and k is the imaginary part known as the extinction coefficient.

Therefore,

$$\varepsilon = (n + ik)^2 = n^2 - k^2 + 2ink$$

$$\varepsilon_1(\omega) = n(\omega)^2 - k(\omega)^2$$

$$\varepsilon_2(\omega) = 2n(\omega)k(\omega)$$

Hence, the coefficient r is also expressed as:

$$r(\omega) = \frac{n(\omega) + ik(\omega) - 1}{n(\omega) + ik(\omega) + 1} \quad (3.12)$$

The real and imaginary parts of the complex coefficient $r(\omega)$ are functions of the index of refraction n and the extinction coefficient k .

With some arrangements to equation (3.12), we get:

$$r = \frac{(n^2 + k^2 - 1) + 2ik}{(n + 1)^2 + k^2}$$

For now we have two forms of the coefficient of reflectivity $r(\omega)$; the first form which involves the amplitude and the phase change is obtained by Kramers-Kronig relations, and by equating the second form to the first one, the second form can be obtained.

The two forms are equated as follows:

$$\left\{ \begin{array}{l} \rho(\omega) \cos \varphi(\omega) = \frac{n^2 + k^2 - 1}{(n + 1)^2 + k^2} \quad (i) \\ \rho(\omega) \sin \varphi(\omega) = \frac{2k}{(n + 1)^2 + k^2} \quad (ii) \end{array} \right.$$

Recalling, given the reflectance R the amplitude ρ is known; $\rho = \sqrt{R}$ and the phase change $\varphi(\omega)$ is obtained by the K-K relations derived above.

The two equations (i) and (ii) represent a system of two equations with two unknowns (n and k) which are equated and solved using a MATLAB code that performs iterations on all the frequency range.

As a summary, reflectivity measurements R allow the determination of the real index of refraction n and the extinction coefficient k from Kramers-Kronig relations. Once the reflectivity measurements are done, the graph of R (reflectivity) versus wavenumber will be extrapolated to the high and low wavenumber regions by Lorentz functions, since Kramers-Kronig integrals are up to infinity. The results are put in a K-K MATLAB code that gives n and k . Then these values are inserted in a corrected K-K MATLAB code which searches for the corrected n and k values i.e. those that satisfy Maxwell's relations. Finally, this code provides us with the corrected values of n and k that are used to calculate the energy loss function.

3.3.5.2. Energy Loss Function

The energy loss function involves the imaginary part of the function $(-1/\varepsilon)$

$$\begin{aligned}\frac{-1}{\varepsilon} &= \frac{-1}{\varepsilon_1 + i\varepsilon_2} = \frac{-(\varepsilon_1 - i\varepsilon_2)}{\varepsilon_1^2 + \varepsilon_2^2} \\ \frac{-1}{\varepsilon} &= \frac{-1}{(n^2 - k^2)^2 + (2nk)^2} ((n^2 - k^2) - 2ink) \\ \text{Im}\left(\frac{-1}{\varepsilon}\right) &= \frac{2nk}{(n^2 - k^2)^2 + (2nk)^2} = \frac{2nk}{n^4 + k^4 - 2n^2k^2 + 4n^2k^2} \\ &= \frac{2nk}{n^4 + k^4 + 2n^2k^2}\end{aligned}$$

Therefore,

$$\text{Im}\left(\frac{-1}{\varepsilon}\right) = \frac{2nk}{(n^2 + k^2)^2} \quad (3.13)$$

Plotting this function (equation (3.13)) against the wavenumber, we obtain the energy loss function graph. The peak appearing in the graph determines the position of the band gap. An example of an energy loss function computed and graphed as a function of the wavenumber is depicted in figure 3.12.

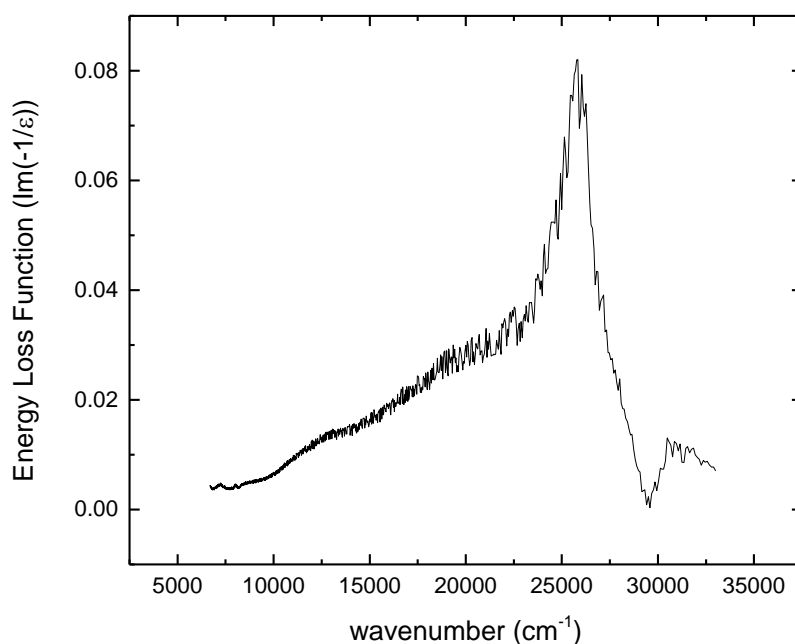


Figure 3.12: Energy loss function versus the wavenumber of the ZnO target

3.3.5.3. Band gap energy E_g

The plots of the energy loss functions of most samples revealed considerable noise which affected our accurate determination of the position of the band gap. To remove the noise, the ‘smoothing’ processing technique via Origin software has been performed on our data plots, with the choice of the Savitzky-Golay method, which performs local polynomial regression around each point and creates a new smoothed value for each data point. The advantage of this specific method is that the features of the original plot, such as the peak height and width, will be preserved. One can increase the smoothness of the plot by increasing the window size, which is the number of data points used in each local regression; a clear smoothed plot of the energy loss functions has been obtained by choosing 51 points as the window size. The resulting smoothed plot of the energy loss function of the target (figure 3.12) is shown in figure 3.13 (the

red curve). In the next chapter the red curve or the envelope (such as in figure 3.14) of the energy loss function of the samples will be presented.

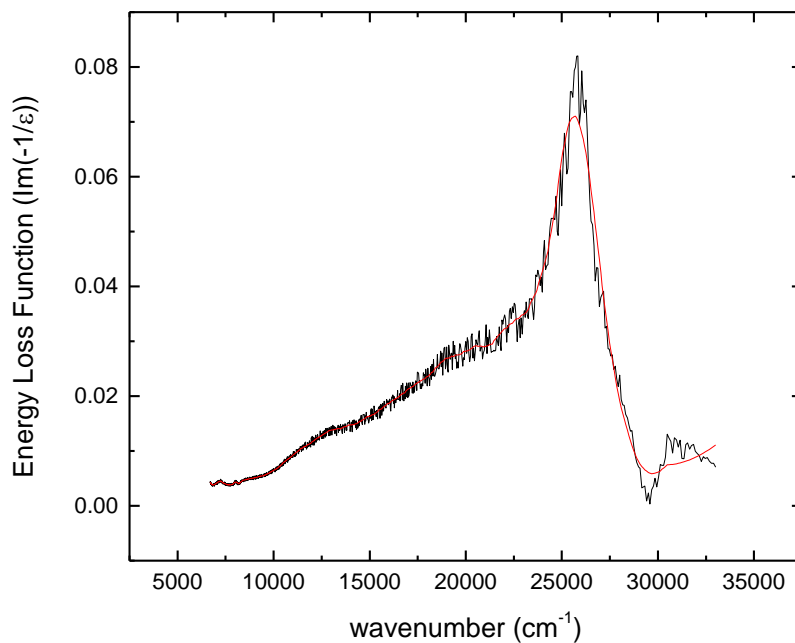


Figure 3.13: Smoothed energy loss function of the ZnO target

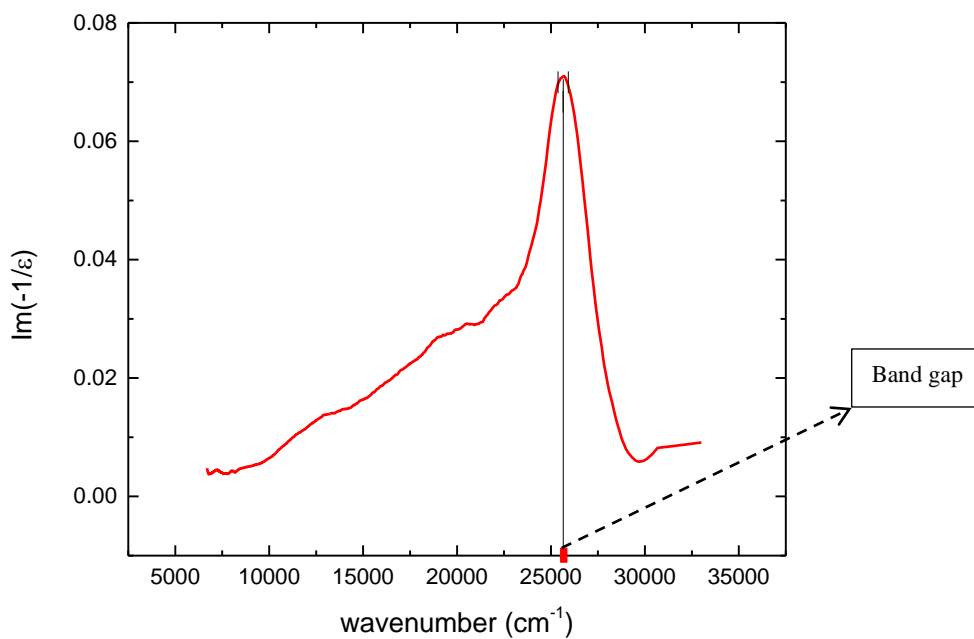


Figure 3.14: The envelope of the energy loss function of the ZnO target

The band gap has been determined by the position of the peak appearing in the energy loss function (such as in figure 3.14); the value of this position (in cm^{-1}) has been converted into electron volts (eV) and listed in the next chapter. The error has been taken to be visual i.e. around the maximum of the peak.

3.4. Experimental Procedure

The growth of the ZnO films was achieved in the following manner:

Step 1: Preparing the PLD chamber and laser alignment

The laser was allowed to warm up for 8 minutes before being used. To make sure that the laser is hitting the entire target, a plexi glass was placed in the target port, the substrate shutter was closed and the laser was set at a certain high voltage and relatively low repetition rate. Turning the target rotation on and then running the laser for few minutes we ensured a maximum coverage of the target by the laser.

This plexi glass was removed and a clean one was placed instead, the substrate holder and the metal plate were also placed in their position in the chamber. One laser shot was performed, and the point where the laser hit the target (i.e. plexi glass) was projected via a needle-like metal by a mark on the metal plate. At this mark the sapphire piece should be placed.

Step 2: Cleaning and pasting the substrate

For the first seven samples, the sapphire substrates were ultrasonically cleaned by isopropanol for 10 minutes and then rinsed with double distilled water for two minutes. EDX results showed that there is some carbon contamination in these samples, whose origin is still unknown, but suspected that the cleaning procedure is not appropriate, and so we developed another way to clean the sapphire pieces and wafers based on cleaning procedure guides (Kern and Vossen) and literature reviews. The rest

six substrates were placed in acetone at 60°C for 10 minutes and then for another 10 minutes in methanol at 70°C, after which they were rinsed with double distilled water for 2 minutes and dried with N₂ gas.

Once cleaned, the substrates were glued to a 2 inch round metal plate using silver paste. For the paste to dry, the plate with the substrate glued on it was heated in an oven for 30-60 minutes at 150°C-200°C.

Step 3: Installing the substrate in the chamber

After removing the metal plate from the oven, an aluminum strip was placed on the edge or corner of the sapphire piece, wiped previously with isopropanol. The ZnO target, metal plate and substrate holder were installed in their position in the PLD chamber which was then cleaned and wiped with alcohol (isopropanol, ethanol or methanol), dried with N₂ gas and put under vacuum. The base pressure was of the order of 10⁻⁵ mbar.

Step 4: Deposition Conditions

After reaching vacuum, the heater was turned on and the required temperature was chosen and left for some time to be reached and stabilized. Next, oxygen gas was introduced into the chamber to attain the required pressure. Sometimes the rotational speed of the pump was adjusted in process of achieving the required pressure.

Step 5: Deposition

Before starting our deposition, the ZnO target was cleaned by shooting it by the laser for five minutes whose high voltage was set at 27 kV and repetition rate 10 Hz. Finally, it's time for deposition. The substrate-target distance is set, the energy mode is chosen from the laser controller (energy mode, no gas refill EGY NGR), and the laser energy, and repetition rate are selected. The laser was executed for 20 minutes.

After deposition, oxygen input was disabled, and the sample was removed from the chamber after allowing the heater to cool down to room temperature.

3.5. Materials and Experimental Details

For all deposited samples the target used was a 99.99% pure ZnO and the substrate was sapphire (Al_2O_3) which was placed at half maximum distance (~7.5 cm) from the target. The deposition time for all samples was 20 minutes.

Chapter 4

RESULTS AND DISCUSSION

4.1. Introduction

In this chapter we present the results of the growth of zinc oxide thin films under various deposition parameters. We investigate the impact of these parameters on the structural, morphological and optical properties of the films using the characterization techniques discussed in the previous chapter.

4.2. Effect of Oxygen Pressure at 725°C

To study the effect of deposition oxygen pressure on the properties of the deposited ZnO films, three samples were prepared at a fixed trial substrate temperature 725°C. The table below lists the conditions for the samples grown at 725°C and at different oxygen pressures.

Table 4.1: Experimental conditions for samples grown at different oxygen pressures and substrate temperature 725°C

Sample name	O ₂ pressure (mTorr)	Temperature (°C)	Laser Energy (mJ)	Repetition Rate (Hz)
N nS5	1	725	400	20
S0	10	725	400	20
S6	100	725	400	20

4.2.1. XRD results and analysis

Figure 4.1 shows the diffraction patterns for these samples. These correspond to $\theta/2\theta$ scans. Clearly, a strong and a narrow peak appears for all three samples at a diffraction angle $2\theta \sim 34^\circ$ which corresponds to the (002) orientation of the ZnO films, in addition to a small peak at around $2\theta \sim 72^\circ$ corresponding to the (004) orientation of the films. This is an indication that the films are strongly crystallized and highly oriented along the c-axis.

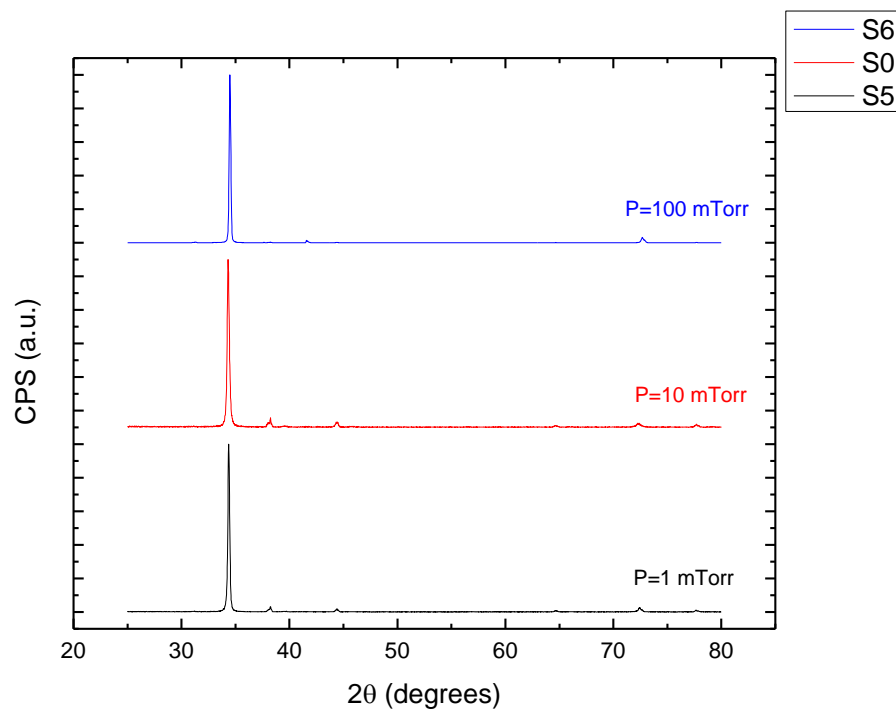


Figure 4.1: $\theta/2\theta$ scans for samples deposited at different oxygen pressures and substrate temperature 725°C

The small peaks appearing in the XRD patterns of S0 and S5 samples at diffractions angle $\sim 38.2^\circ$ and 44.36° are proved to be reflections from the sapphire substrate, by the search and match process via the EVA software (Appendix B).

The table below summarizes the lattice constant c , the average or macroscopic strain ϵ , the FWHM of the (002) peak and the average grain size h obtained from XRD graph and analysis.

Table 4.2: The lattice constant c , the strain ϵ , the (002) peak width and the average grain height h of films deposited at different oxygen pressures and substrate temperature 725°C

Pressure (mTorr)	c (Å)	w (degrees)	h (nm)	strain ϵ (%)
1	5.2164 (0.0006)	0.085	35	0.23606
10	5.2139 (0.0006)	0.214	13.7	0.18812
100	5.1978 (0.0006)	0.135	21.8	-0.12125

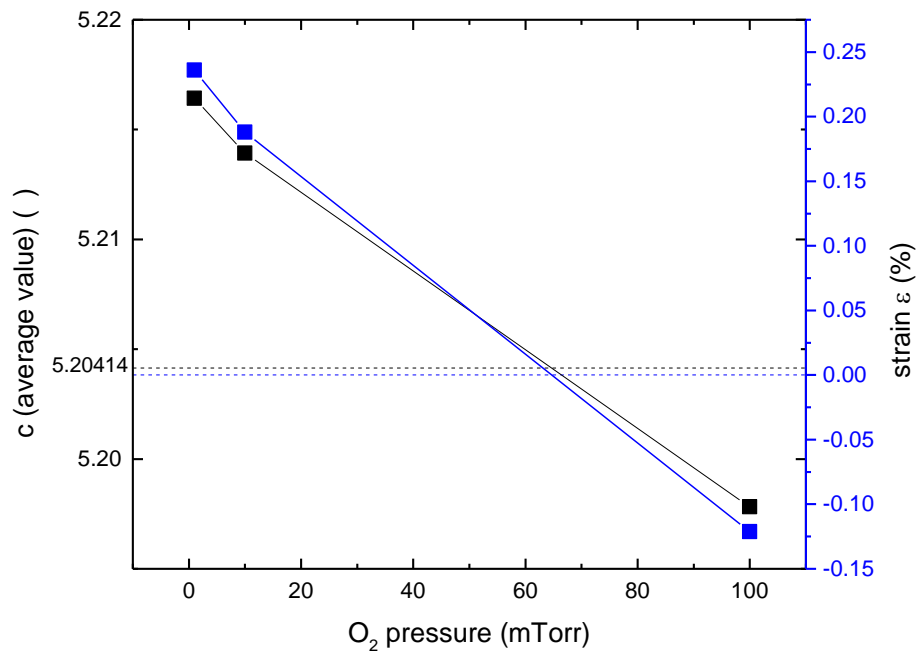


Figure 4.2: Variation of the lattice constant c and the strain ϵ with oxygen pressure for films deposited at substrate temperature 725°C

Figure 4.2 shows the variation of the lattice constant ' c ' and the average strain ϵ as a function of background oxygen pressure. The black dotted line in figure 4.2 represents the c value of the target. It appears from the graph that the c value of the samples and consequently the strain ϵ decreases with increasing pressure, and that the variation in deposition pressure allows us to vary the stress in the layers from tensile stress (at low pressures) to compression (at high pressures).

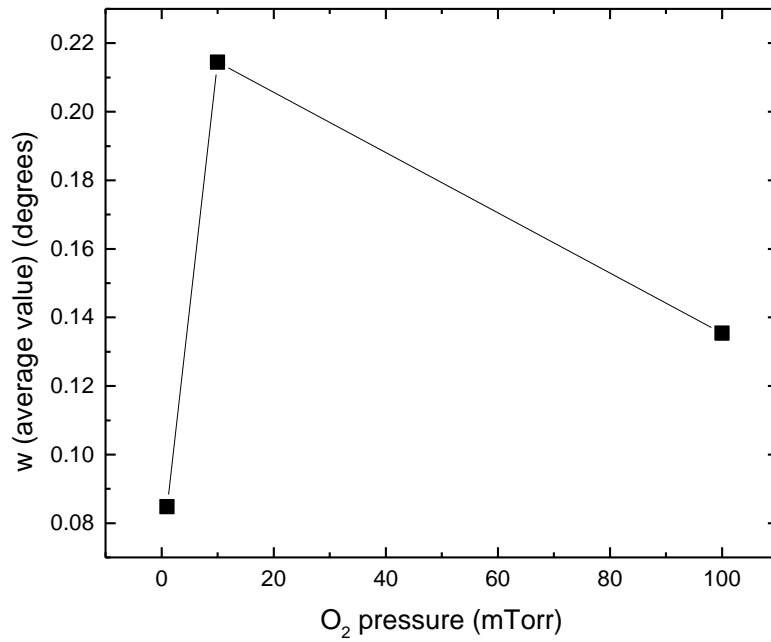


Figure 4.3: Variation of the width of the (002) peak with oxygen pressure for films deposited at substrate temperature 725°C

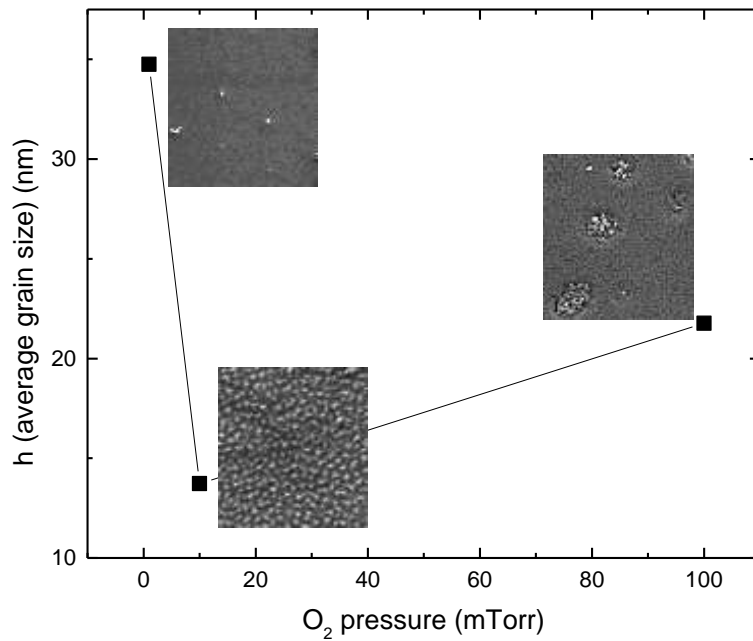


Figure 4.4: Variation of the average grain height h as a function of oxygen pressure for films deposited at substrate temperature 725°C

The width w of the XRD peak and the grain size h are inversely proportional; a smaller width implies larger grains and hence better crystallinity, and this is what appeared at low and high pressures (1 mTorr and 100 mTorr) unlike at intermediate ones (10 mTorr). As a conclusion, for a substrate temperature of 725°C, the crystalline quality of the films is enhanced at 1 mTorr and 100 mTorr and the enhancement at 1 mTorr is at a greater percentage than that at 100 mTorr. Contrary to our results, Zhang et al. concluded that the crystallinity of the deposited films is degraded at high oxygen pressures (100 mTorr), the (002) peak in the XRD pattern became weak and other peaks appeared. This might be due to the type of laser in charge; they employed a pulsed Nd:YAG laser operating at 10 Hz and an energy of 200 mJ and the substrate temperature which was 400°C.

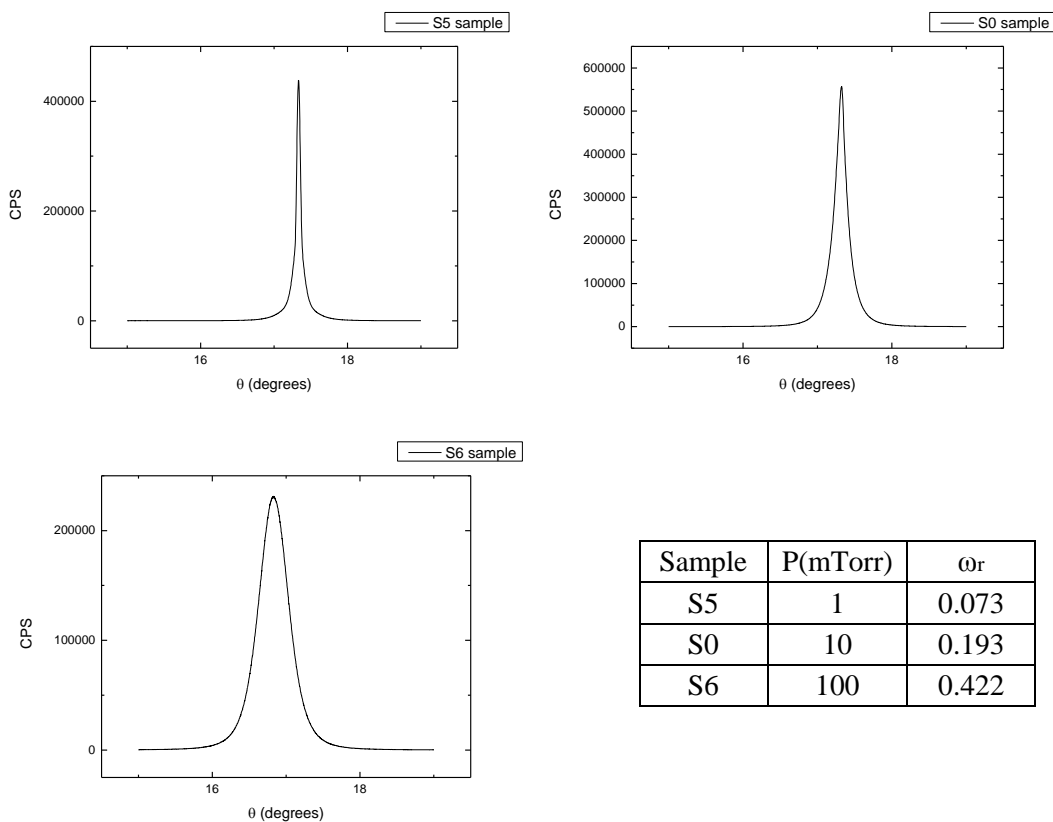


Figure 4.5: Rocking Curves of S5, S0 and S6 samples; the ZnO films deposited at 1, 10 and 100 mTorr of oxygen pressure, respectively

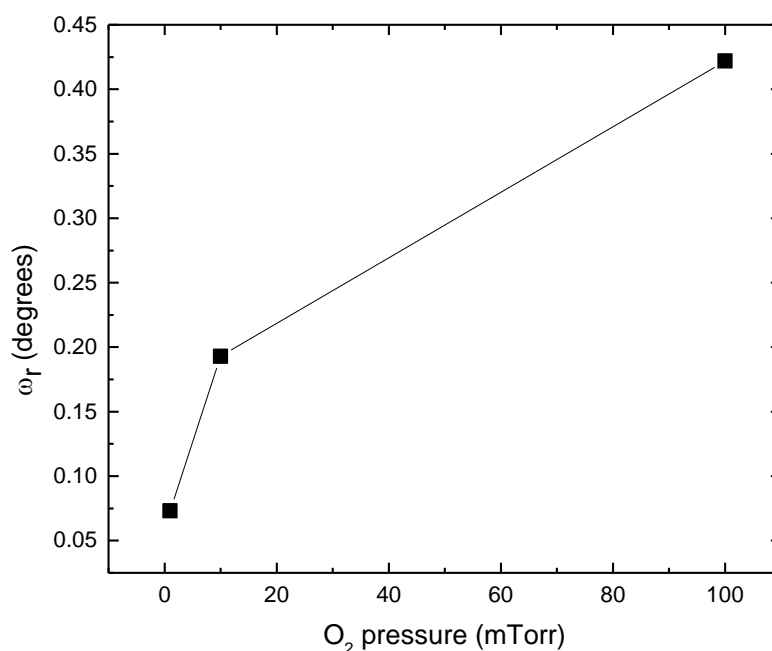


Figure 4.6: Variation of the FWHM rocking curves as a function of background oxygen pressure, for films deposited at 725°C of substrate temperature

Figure 4.5 shows the rocking curves of the three samples deposited at different background oxygen pressures, and figure 4.6 reveals the trend of the variation of the FWHM (ω_r) of the rocking curves with oxygen pressure. This latter figure shows an increasing trend in ω_r as the oxygen pressure increases. Since ω_r is the smallest for an oxygen pressure of 1 mTorr, then the ZnO thin film deposited at this value of O₂ pressure (and 725°C of substrate temperature) has the best crystalline quality. This is in agreement with the FWHM of the (002) XRD peak and the grain size analysis, recalling that at this oxygen pressure the FWHM (002) peak is the smallest and consequently the average grain size is the largest among the rest of the films in this set.

4.2.2. SEM images and discussion

SEM imaging of the three samples deposited under various oxygen pressures revealed different surface morphologies. For the sample at 1 mTorr of oxygen pressure (S5 sample), the surface is extremely smooth and hexagonal structures can be barely seen at a magnification of $2\ \mu\text{m}$, in addition to ZnO nanodots, with careful looking, are seen to be present on top of ZnO pyramidal caps. With increasing oxygen pressure to 10 mTorr, the surface becomes rougher and ZnO nanostructures are seen, making it a grained surface, in addition to ZnO nanorods found atop the surface. The surface of the sample at 100 mTorr of oxygen pressure consisted of rough islands of ZnO nano-grains. So, we can conclude that the oxygen pressure has a significant impact on the surface morphology of the deposited films; as the background oxygen pressure increases the surface of the film becomes rougher. This conclusion is in agreement with Valerini et al. although their deposition conditions were different, such as a substrate temperature of 600°C , 10 Hz repetition rate and silicon (100) as the substrate, they observed a rougher surface as the oxygen pressure in the chamber increases.

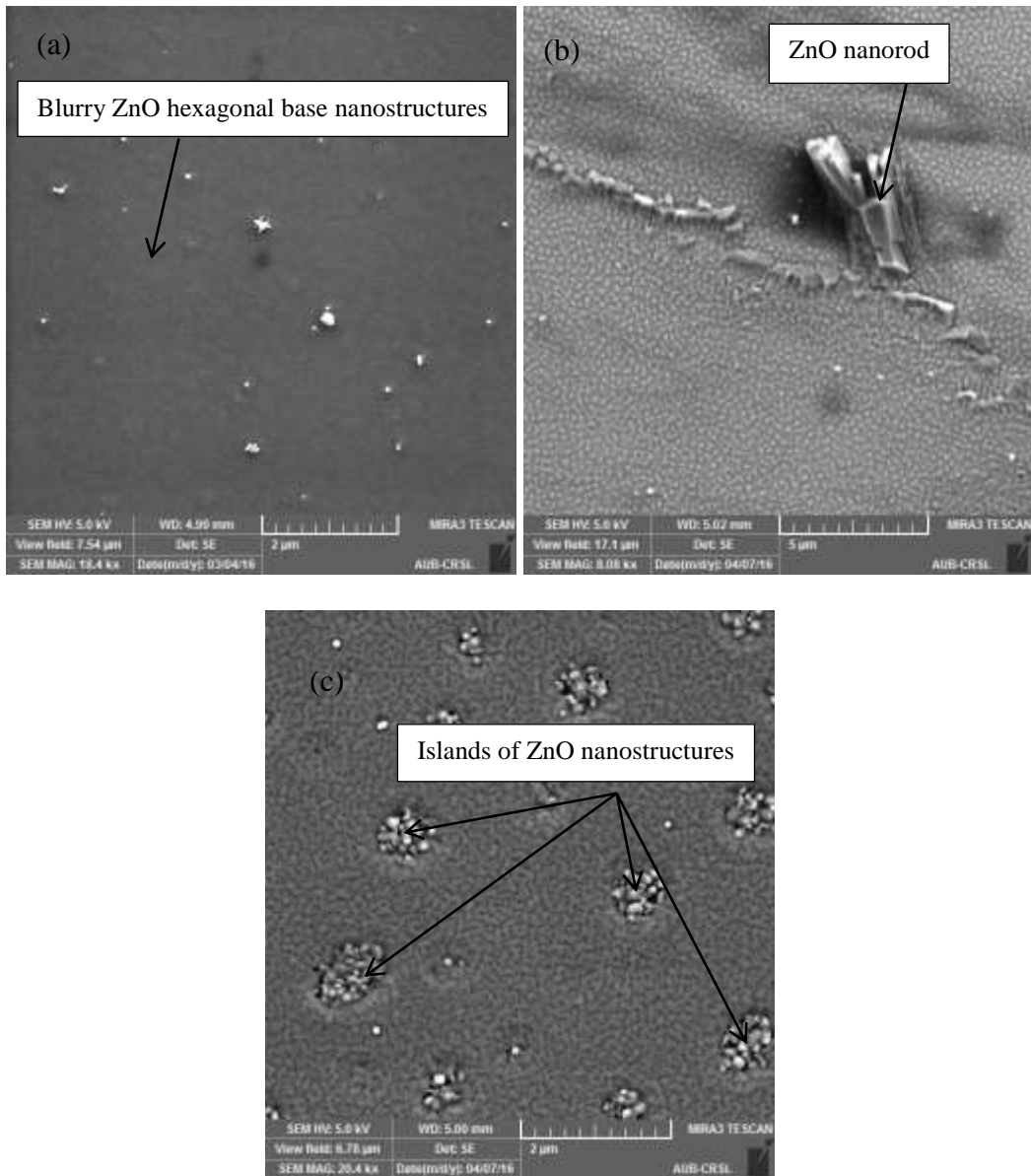


Image 4.1: SEM images of S5, S0 and S6 samples, the ZnO films deposited at (a) 1, (b) 10 and (c) 100 mTorr of oxygen pressure respectively, and 725°C of substrate temperature.

4.2.3. EDX results and analysis

Table 4.3: The atomic composition of films deposited at different background oxygen pressures and substrate temperature 725°C

SEM-EDX					
Sample	Pressure	atomic % Zn	atomic % O	atomic ratio	atomic % C
S5	1 mTorr	47.3	52.7	0.898	0
S0	10 mTorr	40.08	40.88	0.980	19.04
S6	100 mTorr	48.86	51.14	0.955	0

where the atomic ratio = $\frac{\text{atomic \% Zn}}{\text{atomic \% O}}$

From EDX measurements we can notice that there are no oxygen deficiencies or vacancies in the samples and the atomic ratio of Zn atoms to O atoms is almost 1:1, except for the sample deposited at an oxygen pressure of 1 mTorr (S5 sample) were it contained deficiencies in zinc atoms, this is due to unknown reasons. Carbon contamination in some regions in S0 film was detected as shown above, and the atomic percent of carbon atoms in the selected region reached 19%. The source of carbon in the films is suspected to be due to an unclean PLD chamber and substrate (sapphire). This was solved by cleaning well the chamber with strong alcohols such as methanol, acetone and isopropanol, in addition to following the cleaning procedure for sapphire wafers and pieces discussed in the previous chapter (chapter 3).

4.2.4. Optical Properties

In chapter 3 we discussed the technique used to study the optical properties of the deposited ZnO films, the UV-VIS spectroscopy technique. The reflectance (%R) spectra of the ZnO films deposited at various oxygen pressures and at a fixed substrate temperature 725°C are shown in figure 4.7.

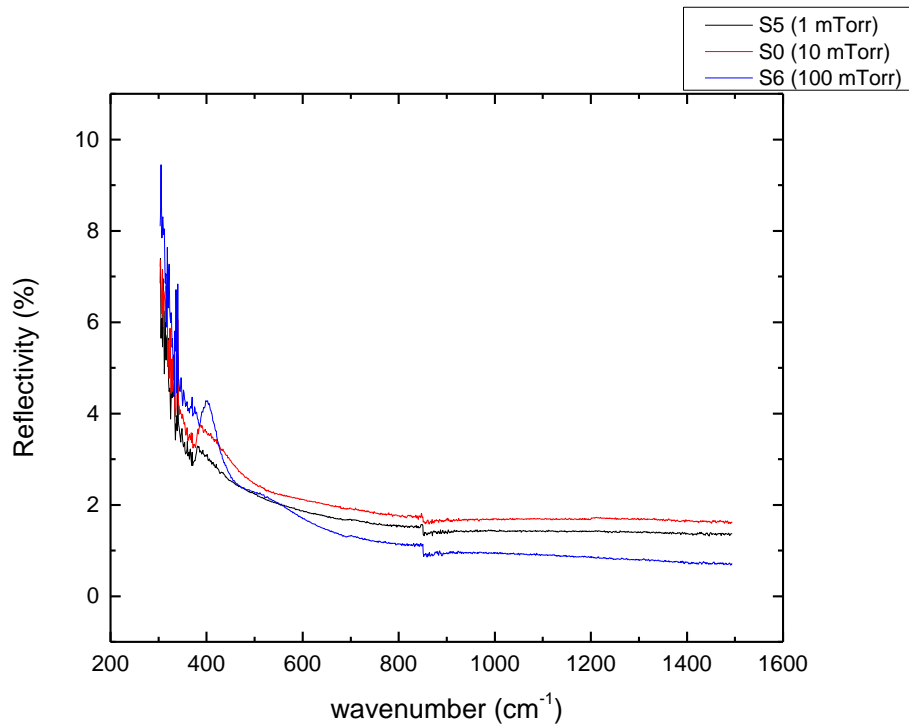


Figure 4.7: Reflectance spectra of ZnO films deposited at different oxygen pressures and substrate temperature 725°C

In the infrared and visible range (1500 nm to ~450 nm), the samples have a minimal percentage of reflectance, below 2%, which means that over this wide wavelength range transmission of radiation takes place, explaining the fact that all three samples are observed to be extremely transparent.

From the experimental data shown in figure 4.7, the energy loss function of each sample was calculated by the Kramers-Kronig method as described in Chapter 3. The smoothed plots of the corresponding energy loss functions as a function of wavenumber are shown in figure 4.8.

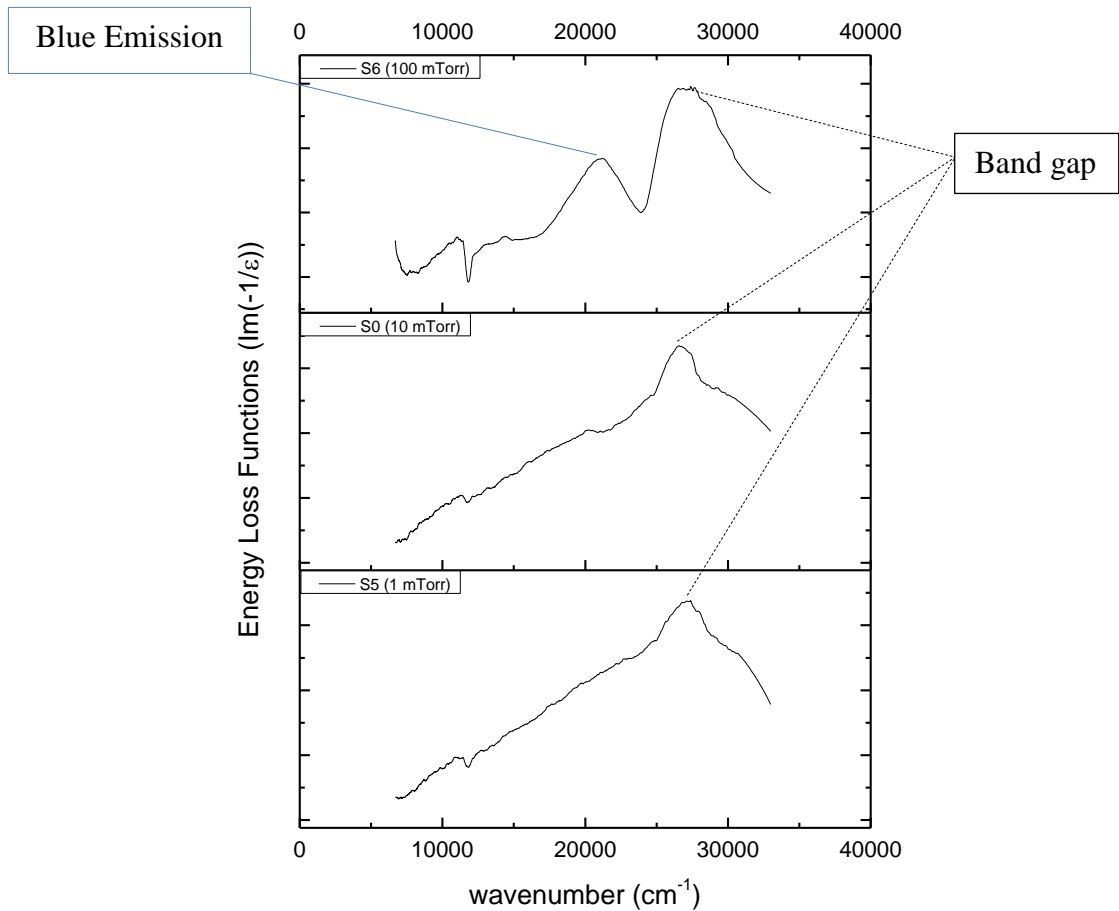


Figure 4.8: Energy loss functions of ZnO films deposited at different oxygen pressures and substrate temperature 725°C

A UV peak centered at ~370 nm can be observed for all the samples which correspond to the near band edge emission. The energy loss function of the sample deposited at 100 mTorr of oxygen pressure reveals an additional peak around a wavenumber of 21097 cm^{-1} i.e. 475 nm which is a blue emission and hence an indication of a defect in the thin film. The other two samples deposited at an oxygen pressure of 1 mTorr and 10 mTorr do not reveal significant defects in the samples and the band gap E_g of the films along with that of the target were obtained (see chapter 3) and are listed in table 4.4.

Table 4.4: Band gap energy values for films deposited at different oxygen pressures and substrate temperature 725°C

Sample	Pressure	Energy	Temp	RepRate	Band gap (eV)	Error (eV)
S5	1 mTorr	400 mJ	725°C	20 Hz	3.371	0.029
S0	10 mTorr	400 mJ	725°C	20 Hz	3.30	0.04
S6	100 mTorr	400 mJ	725°C	20 Hz	3.36	0.08
Target					3.181	0.026

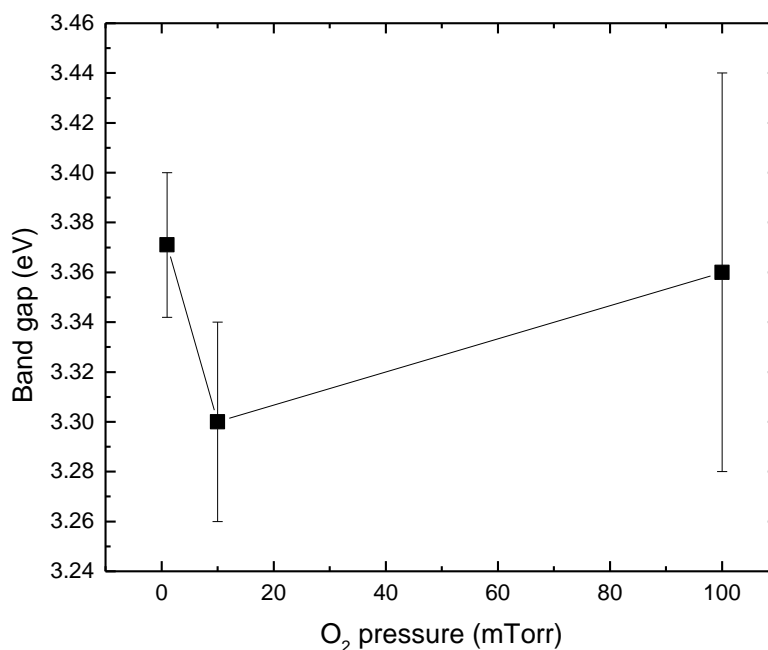


Figure 4.9: Variation of the band gap energy value as a function of oxygen pressure for films deposited at substrate temperature 725°C

Figure 4.9 shows the variation of the band gap of the deposited ZnO films as a function of the oxygen pressure. The band gap of the ZnO films is shifted from that of the target; their band gap is larger and actually agrees with the literature reviews. It is important to note at this point that the band gap energy is greatly affected by the stress imposed in the films and it is for this reason why the band gap values are shifted from that of the target, the stress-free sample. In some articles it is stated that ZnO has a band gap of 3.3 eV (Sun et al., 1999) and in some others it is considered as 3.37 eV (Sandana

et al., 2009), depending on the reference sample. In this set of samples the band gap energy has been varied from 3.30 eV to 3.37 eV, nevertheless, the variation is considered to be within the experimental error.

Comparing to Liu et al. results, where they deposited at a laser energy of 250 mJ and varied the oxygen pressure in the range 5-20 Torr while keeping the substrate temperature at 700°C, a strong, broad and green emission was revealed in the PL spectrum signifying defects in the samples such as oxygen vacancies, however, in our samples at the different oxygen pressures we varied this green emission was not detected, but rather a blue emission only for the highest oxygen pressure deposited sample (100 mTorr).

4.3. Effect of Substrate Temperature

An extensive study has been done over years to test the effect of the substrate temperature on the quality of the deposited thin films. Based on this and the literature, ZnO thin films deposited at low substrate temperatures i.e. below 500°C down to room temperature have a poor crystalline structure and bad optical properties. These resulting thin films were against our aim and so we have chosen three different temperatures (>500°C) to do our deposition, hoping to get excellent qualities of the films in terms of crystallinity and band gap energy. The table below summarizes the conditions chosen to study this effect.

Table 4.5: Experimental conditions for samples grown at different substrate temperatures and background oxygen pressure of 10 mTorr

Sample name	Temperature (°C)	O ₂ pressure (mTorr)	Laser Energy (mJ)	Repetition Rate (Hz)
S3	625	10	400	20
S0	725	10	400	20
S2	825	10	400	20

4.3.1. XRD results and analysis

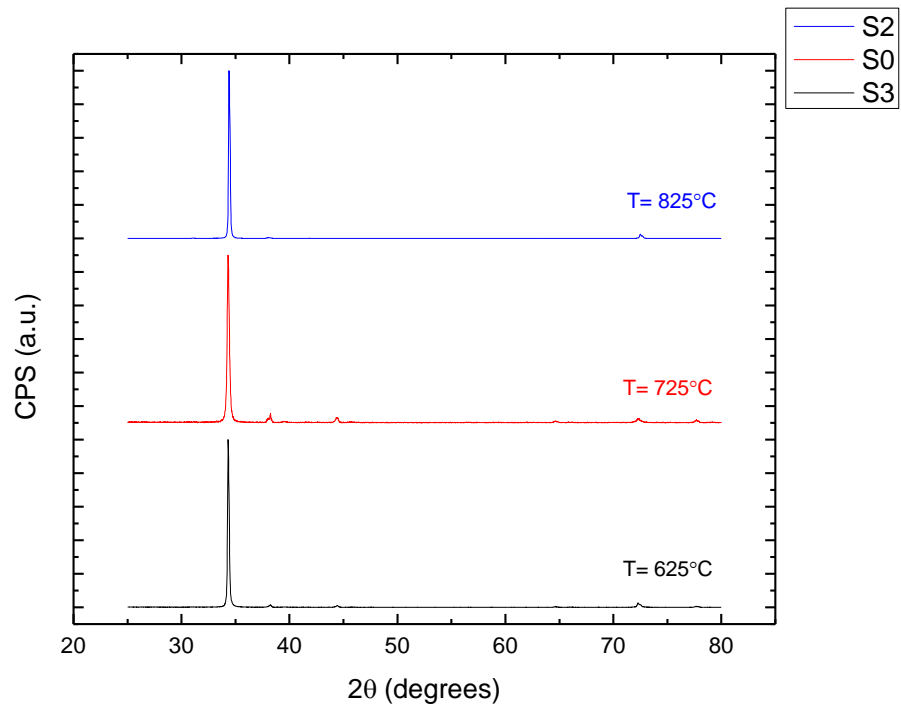


Figure 4.10: $\theta/2\theta$ scans for samples deposited at different substrate temperatures and oxygen pressure of 10 mTorr

The XRD diffractographs of the samples deposited under different substrate temperatures are shown above in figure 4.10. Clearly, one dominant, strong and narrow peak appears for all these samples resembling the (002) orientation and which implies an excellent crystalline quality of the following deposited films. From these graphs we can also detect the (004) orientation, these are parallel to the (002) planes, however they

have much lower intensity than the (002) peak, this indicates that these films are strongly c-axis oriented.

The same approach, as the one discussed in Chapter 3, has been followed to calculate the lattice constant c , the macroscopic (average) strain ϵ , the width w of the XRD (002) peak and the average grain size h of our samples. The results are listed in the table below.

Table 4.6: The lattice constant c , the strain ϵ , the (002) peak width and the average grain height h of films deposited at different substrate temperatures and oxygen pressure of 10 mTorr

Temperature (°C)	c (Å)	w (degrees)	h (nm)	strain ϵ (%)
625	5.2207 (0.0006)	0.079	37	0.31869
725	5.2139 (0.0006)	0.214	13.7	0.18812
825	5.2096 (0.0006)	0.063	47	0.10569

From figure 4.11 we can notice that the stress in the layers in the three different samples is tensile; at a lower substrate temperature (625°C) the layers experience a greater stress, the strain is ~ 0.3% which decreases to 0.1% as the substrate temperature increases to 825°C.

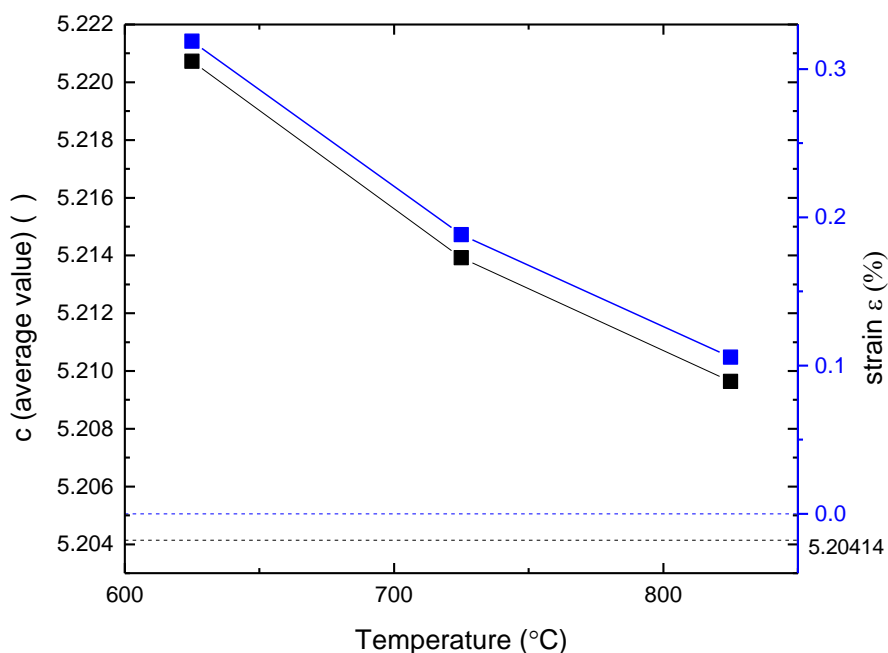


Figure 4.11: Variation of the lattice constant c and the strain ϵ as a function of substrate temperature for films deposited at oxygen pressure of 10 mTorr

Figures 4.12 and 4.13 show the variation of the width of the XRD (002) peak and the average grain size h with substrate temperature. The figures reveal that the XRD peaks of the ZnO films deposited at 625°C and 825°C are narrower than the one deposited at 725°C. The substrate temperature 825°C expresses the best crystallinity, since the width is the smallest at this temperature and as a result the grains are the largest. Besides at this determined optimum substrate temperature (825°C) the strain is the smallest. Similar results were obtained by Sun and Kowk; they found that the best crystalline quality of the films is at a substrate temperature of 700°C and 800°C, although they employed an ArF excimer laser to ablate the ZnO target at laser energy of 150 mJ and frequency of 10 Hz.

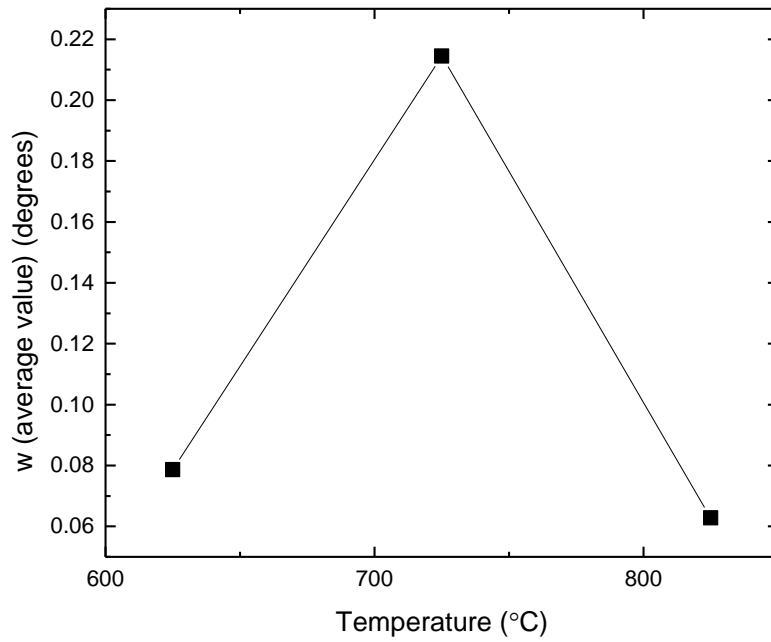


Figure 4.12: Variation of the width of the (002) peak with substrate temperature for films deposited at 10 mTorr oxygen pressure

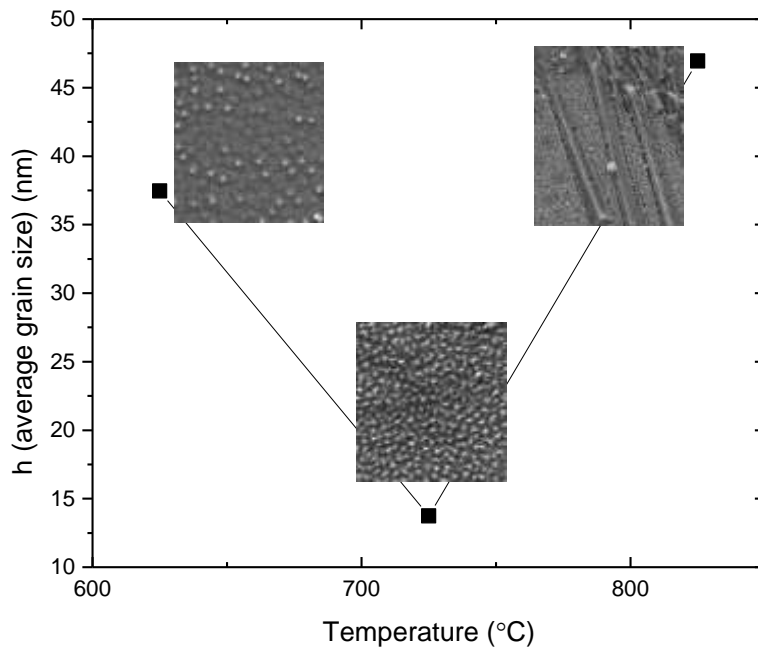


Figure 4.13: Variation of the average grain height h as a function of substrate temperature for films deposited at 10 mTorr oxygen pressure

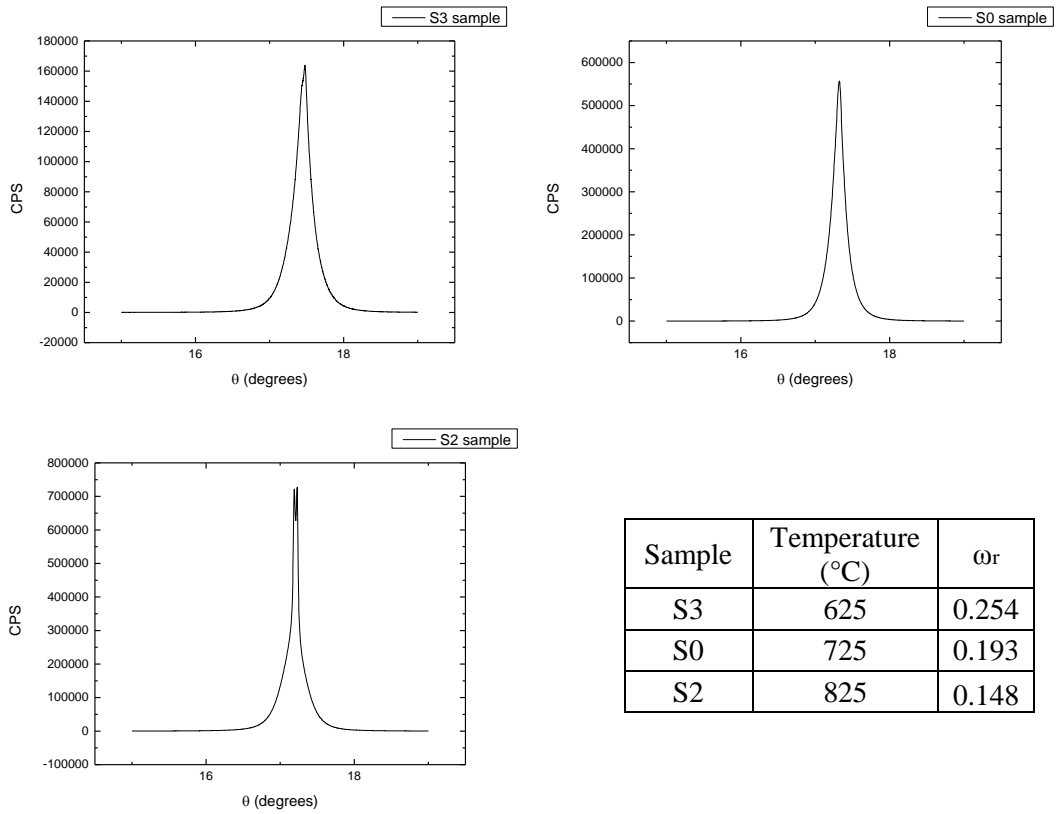


Figure 4.14: Rocking Curves of S3, S0 and S2 samples; the ZnO films deposited at a substrate temperature of 625°C, 725°C and 825°C

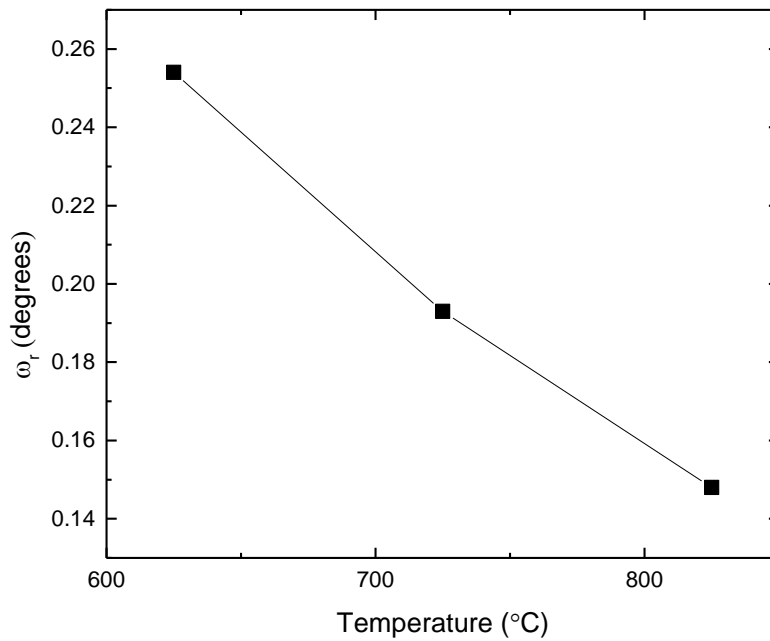


Figure 4.15: Variation of the FWHM rocking curves as a function of substrate temperature, for films deposited at 10 mTorr of oxygen pressure

The variation of the FWHM rocking curve (ω_r) as a function of substrate temperature shows a decreasing trend (Figure 4.15); ω_r takes the smallest value (0.15°) for the ZnO film deposited at a substrate temperature of 825°C (10 mTorr O_2 pressure), which indicates that this film has the best crystallinity. This also agrees with the analysis of the FWHM (002) XRD peak and the average grain size; previously we have concluded that the best crystalline quality is achieved in the ZnO thin film deposited at a substrate temperature of 825°C .

Surprisingly, for this S2 sample the rocking curve shows a double peak; possibly this happens when the surface of the sample shows ‘domains’ with low-angle boundaries created either by deposition defects or curvature of the substrate. Low-angle boundaries are created when the crystals in the film are not perfectly aligned and oriented; there is a slight mismatch and misalignment of the crystals (Speakman, 2012). Scattered x-rays from these domains will not be parallel and their separate interference explains the appearance of two peaks in the rocking curve (Figure 4.16). It is noteworthy to mention that the angular difference between these two peaks is related to the angular difference between these domains.

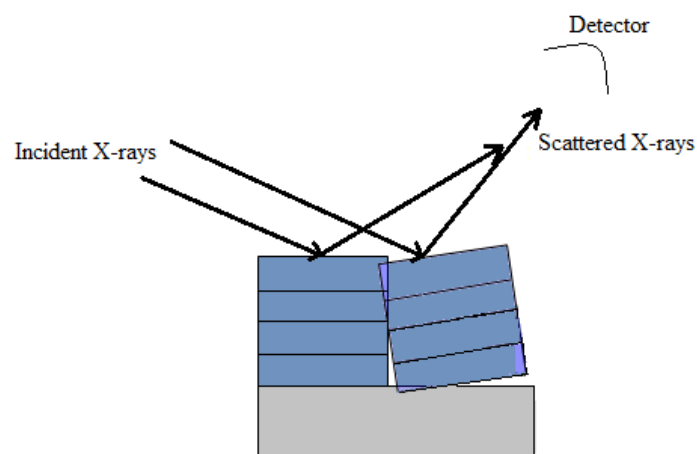


Figure 4.16: Schematic representation of scattered x-rays from domains with low-angle boundaries.

4.3.2. SEM images and discussion

The ZnO film deposited at a substrate temperature of 625°C possesses densely packed ZnO hexagonal nanostructures and pyramidal caps, which ensures the hexagonal crystal nature of our deposited films. These structures were also observed by Valerini et al. but at a substrate temperature of 700°C and fixed oxygen pressure 7.5 mTorr (close to our pressure 10 mTorr). As previously discussed SEM images of the sample deposited at a substrate temperature of 725°C (S0 sample) revealed a grained surface with some nanorods present on the top. Lastly, the surface of the ZnO film deposited at 825°C of substrate temperature also exhibited ZnO nano and micro-rods present atop a smooth surface. As for the roughness of the surface we can notice that it's not much affected by the substrate temperature; for all three films deposited at different substrate temperatures their surfaces are relatively smooth and their roughness are comparable.

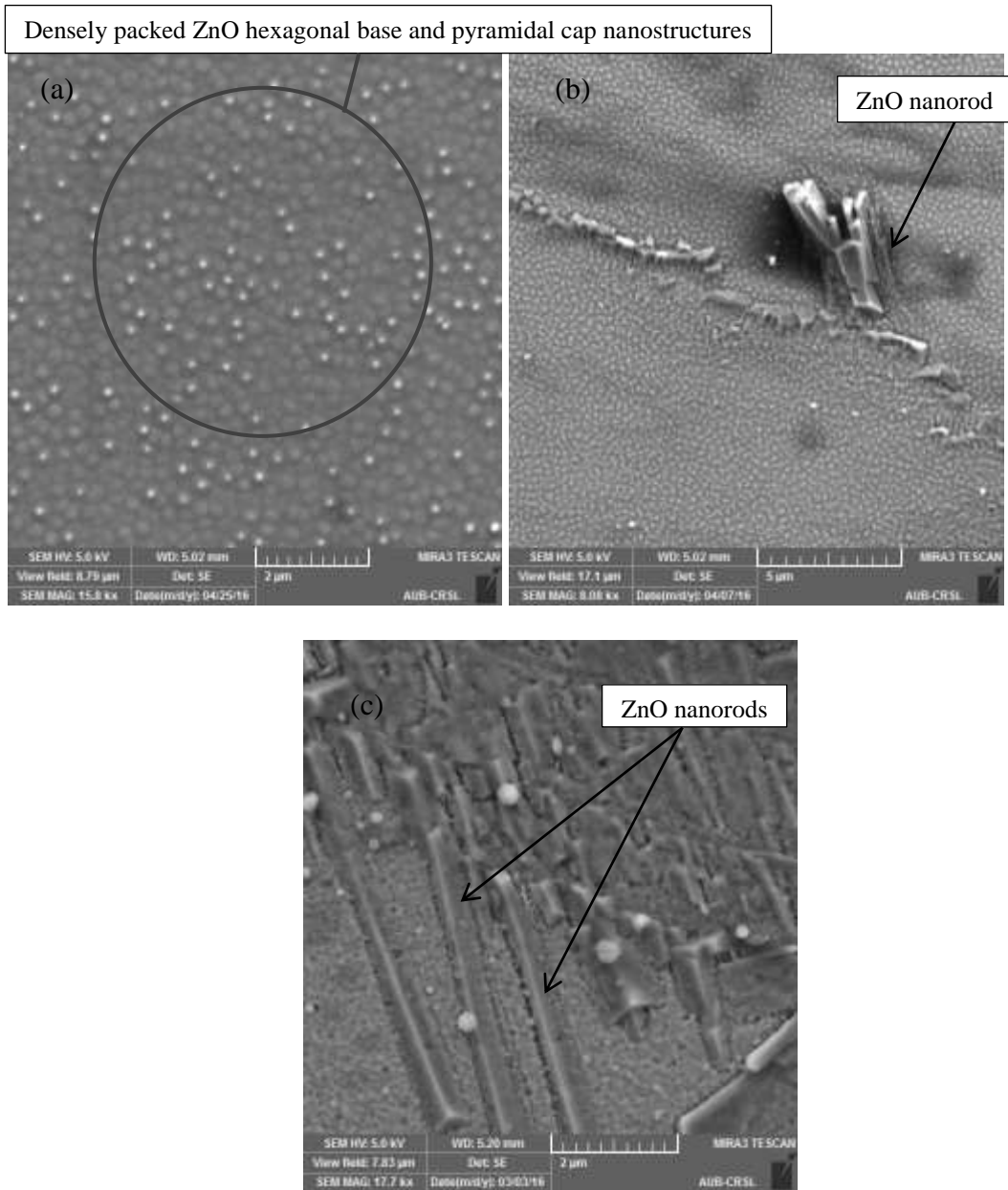


Image 4.2: SEM images of S3, S0 and S2 samples, the ZnO films deposited at (a) 625, (b) 725 and (c) 825°C of substrate temperature respectively, and 10 mTorr of oxygen pressure

4.3.3. EDX results and analysis

Table 4.7: The atomic composition of films deposited at different substrate temperatures and 10 mTorr oxygen pressure

Sample	Temperature	SEM-EDX			
		atomic % Zn	atomic % O	atomic ratio	atomic % C
S3	625°C	48.69	51.31	0.949	0
S0	725°C	40.08	40.88	0.980	19.04
S2	825°C	47.08	47.21	0.997	5.71

where the atomic ratio = $\frac{\text{atomic \% Zn}}{\text{atomic \% O}}$

EDX results showed a close 1:1 ratio of Zn atoms to O atoms for the three samples deposited at different substrate temperatures, and it was noticed that with increasing this temperature the atomic ratio increased to be closer to 1 and hence a better and even composition of zinc and oxygen atoms in the films is obtained at high temperatures (825°C). Note that the chosen ranges for EDX measurements are not the same which might affect the final results. Besides, carbon contamination in S0 and S2 films was detected, and this issue was solved as previously discussed in section 4.2.

4.3.4. Optical Properties

The reflectance spectra of the samples deposited at three different substrate temperatures are plotted in the graph below.

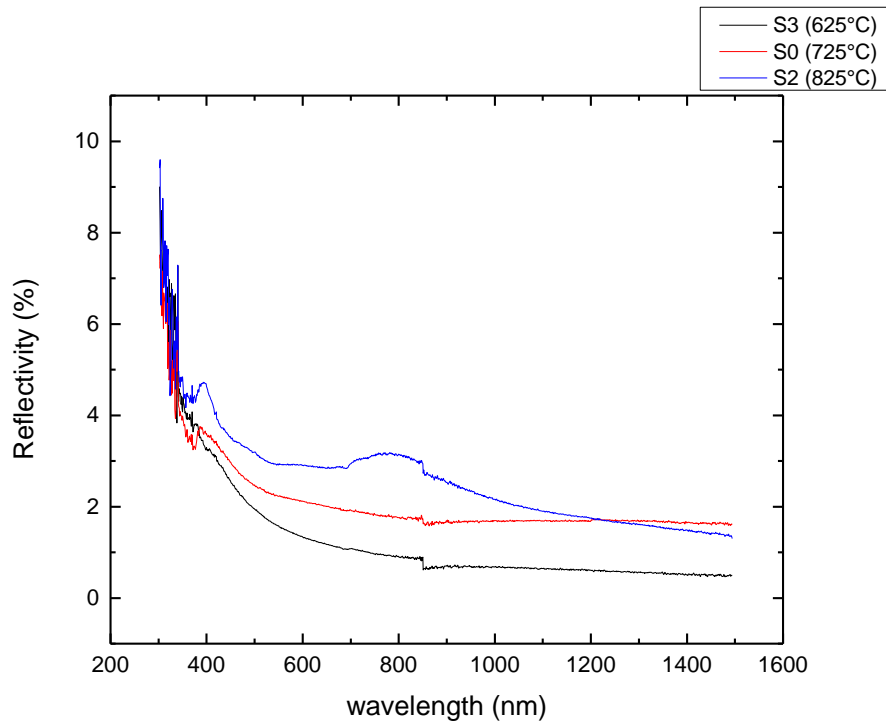


Figure 4.17: Reflectance spectra of ZnO films deposited at different substrate temperatures and 10 mTorr oxygen pressure

Over the infrared and visible range the reflectivity of the two samples (S3 and S0) deposited at 625°C and 725°C is very low, below 3%, which explains the transparency of these two ZnO thin films, unlike for S2 sample where a bump in its reflectivity spectrum and in the visible range appears, explaining the change of color of this sample; it actually reflects a blue-green color (Appendix E).

The experimental data was used to calculate the energy loss function of the films and their band gap energy. In figure 4.18 the smoothed energy loss functions are plotted against the wavenumber and table 4.8 lists the band gap energy values of the three samples and the target.

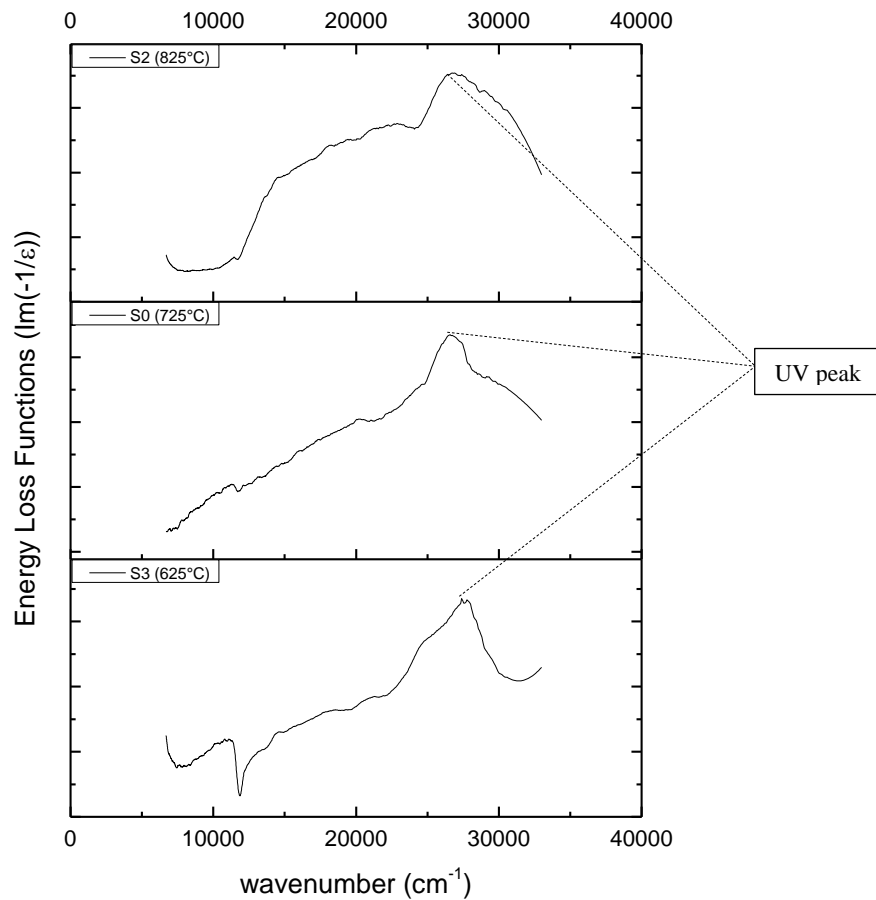


Figure 4.18: Energy loss functions of ZnO films deposited at different substrate temperatures and 10 mTorr oxygen pressure

A strong and clear UV peak centered at ~ 370 nm is observed for all the samples resembling the position of the band gap, which corresponds to exciton emission from the conduction band to the valence band (Wei et al., 2009). The energy loss function of the films do not reveal other pronounced peaks than the UV peak, indicating no significant defects in the films. Liu et al., for samples deposited at an oxygen pressure of 10 Torr and various substrate temperatures (550°C - 700°C), obtained a broad and strong green emission (~ 550 nm) which increased as the temperature increased to 700°C , this was attributed to structural defects in the samples such as oxygen deficiencies.

Table 4.8: Band gap energy values for films deposited at different substrate temperatures and 10 mTorr oxygen pressure

Sample	Pressure	Energy	Temp	RepRate	Band gap (eV)	Error (eV)
S3	10 mTorr	400 mJ	625°C	20 Hz	3.42	0.04
S0	10 mTorr	400 mJ	725°C	20 Hz	3.30	0.04
S2	10 mTorr	400 mJ	825°C	20 Hz	3.31	0.04
Target					3.181	0.026

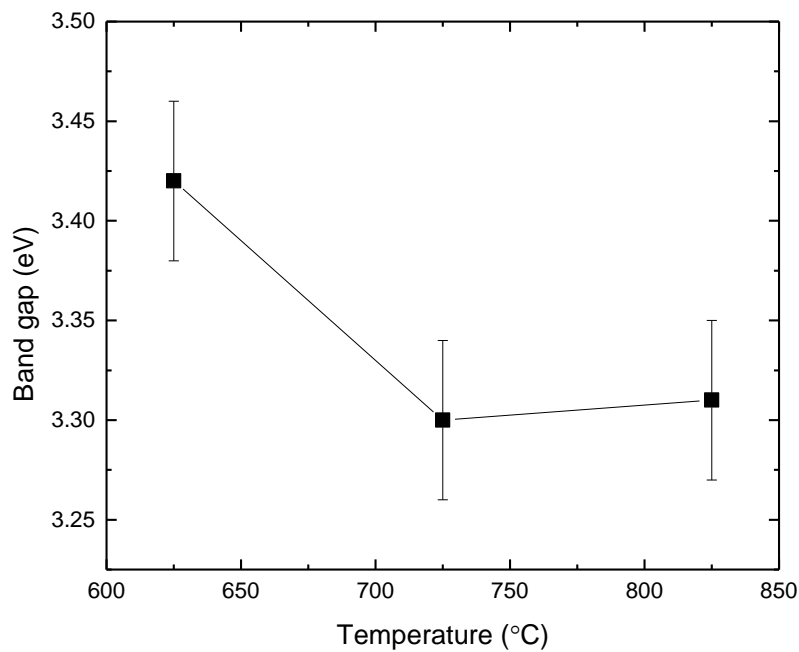


Figure 4.19: Variation of the band gap energy value as a function of substrate temperature for films deposited at 10 mTorr oxygen pressure

Comparing the band gap values of the three samples deposited at different substrate temperatures, the two samples deposited at 725°C and 825°C have a very close and reasonable value ~3.3 eV, while the ZnO film grown at 625°C, although it possessed a good crystalline quality as previously concluded, have a much larger band gap value (3.42 eV), which introduces doubts regarding its nature.

4.4. Effect of Oxygen Pressure at 825°C

A new set of samples was deposited at various oxygen pressures and at a fixed substrate temperature of 825°C; judging from XRD results the crystalline quality of the film deposited at this temperature is the best (narrowest XRD (002) peak).

Table 4.9 summarizes the conditions for the samples grown at this determined temperature and at various background oxygen pressures.

Table 4.9: Experimental conditions for samples grown at different background oxygen pressures and substrate temperature 825°C

Sample name	O ₂ pressure (mTorr)	Temperature (°C)	Laser Energy (mJ)	Repetition Rate (Hz)
S7	25	825	400	20
S8	50	825	400	20
S9	75	825	400	20
S10	100	825	400	20
S11	200	825	400	20
S12	500	825	400	20

4.4.1. XRD results and analysis

As indicated by the XRD patterns in figure 4.20, all samples possess high crystalline quality, by the appearance of a strong dominant and narrow peak at a diffraction angle around 34° corresponding to reflections from the (002) planes. We can also notice reflections from parallel planes to the (002) which are the (004), as indicated by a small peak at around $2\theta \sim 72^\circ$. For some samples, a peak next to the (002) peak appears, it is at a diffraction angle of $\sim 41^\circ$, however, this does not correspond to ZnO;

using the EVA software and matching our scans with the database, the peak at $2\theta \sim 41^\circ$ corresponds to reflections from the sapphire substrate.

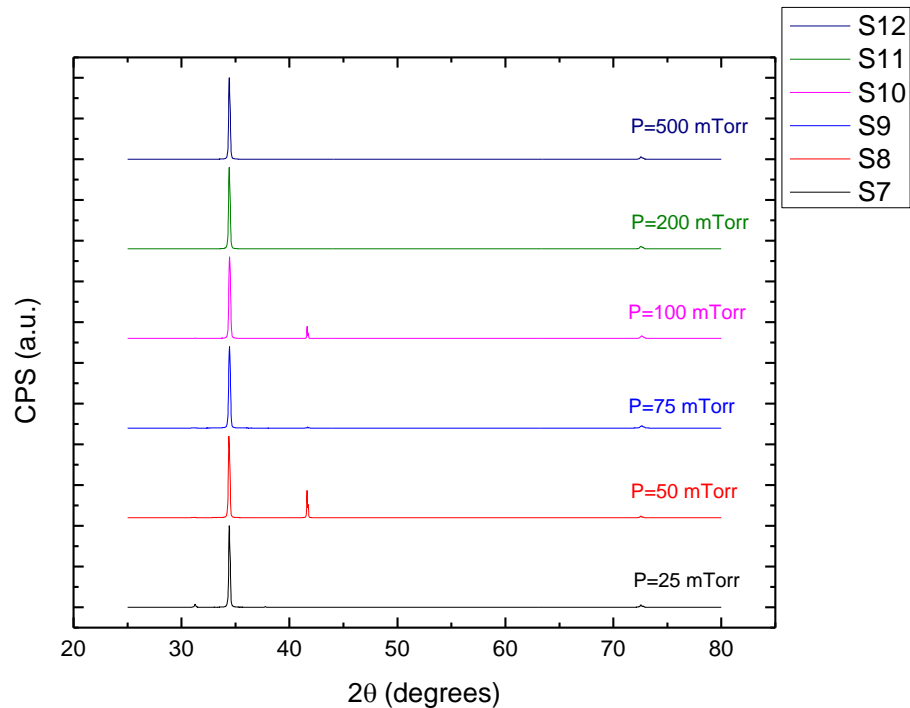


Figure 4.20: $\theta/2\theta$ scans for samples deposited at different background oxygen pressures and substrate temperature 825°C

In the study done by Susner et al. at a substrate temperature of 750°C and at oxygen pressures ranging from vacuum up to 250 mTorr and greater, highly crystallized ZnO thin films were produced at pressures > 250 mTorr by the appearance of a dominant (002) peak, whereas a near-polycrystalline XRD pattern was obtained for films deposited at low and intermediate pressures (25 to 150 mTorr) which indicates a poor crystal quality of the films. Unlike the samples we have, all ZnO thin films at different oxygen pressures are highly oriented along the c-axis as only one and dominant peak appeared corresponding to reflections from (002) planes. Hence all our films are highly crystallized. The difference between our results and the results obtained by Susner is attributed to the choice of the substrate; they used silicon Si (111) whereas

we chose sapphire, in addition to the substrate temperature and probably the laser repetition rate (10 Hz in their case).

Table 4.10: The lattice constant c , the strain ϵ , the (002) peak width and the average grain height h of films deposited at different oxygen pressures and substrate temperature 825°C

Pressure (mTorr)	c (Å)	w (degrees)	h (nm)	strain ϵ (%)
25	5.1819 (0.0006)	0.085	35	-0.42726
50	5.1874 (0.0006)	0.068	44	-0.32176
75	5.1879 (0.0006)	0.144	20.5	-0.31302
100	5.1883 (0.0006)	0.092	32	-0.30351
200	5.1900 (0.0006)	0.076	39	-0.27228
500	5.1926 (0.0006)	0.074	40	-0.22136

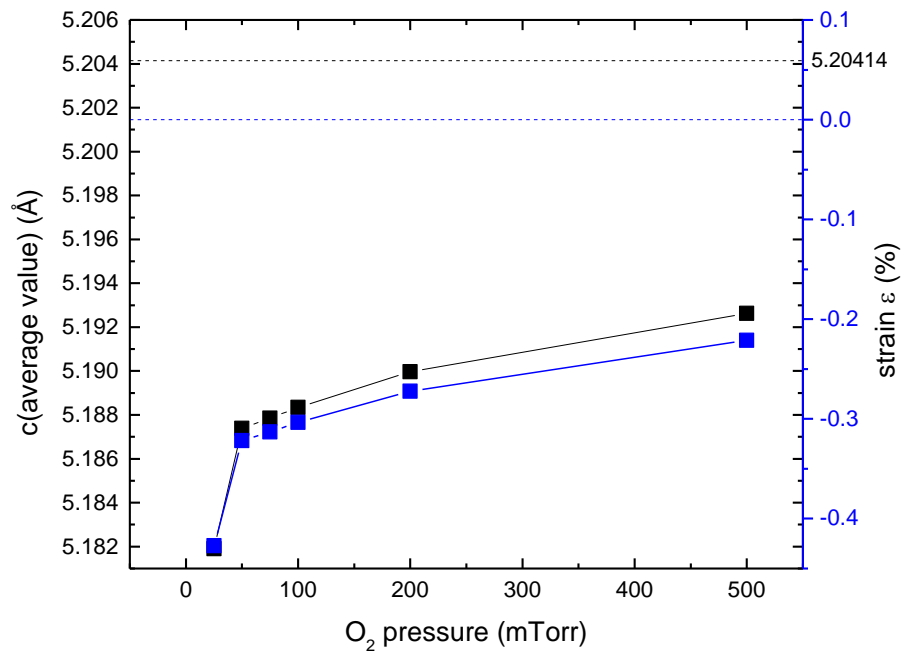


Figure 4.21: Variation of the lattice constant c as a function of oxygen pressure for films deposited at substrate temperature 825°C

For a substrate temperature of 825°C, the lattice constant 'c', and the macroscopic/average strain ϵ for samples deposited under different oxygen pressures show a different and an opposite trend from those deposited at a substrate temperature of 725°C. Recalling, the 'c' value and the average strain for samples deposited at 725°C exhibit a decreasing trend with increase in oxygen pressure, however, in this case, the case of 825°C as the substrate temperature, the 'c' value and the strain ϵ show an increasing trend (figure 4.21), towards a zero strain sample, as the background oxygen pressure increases.

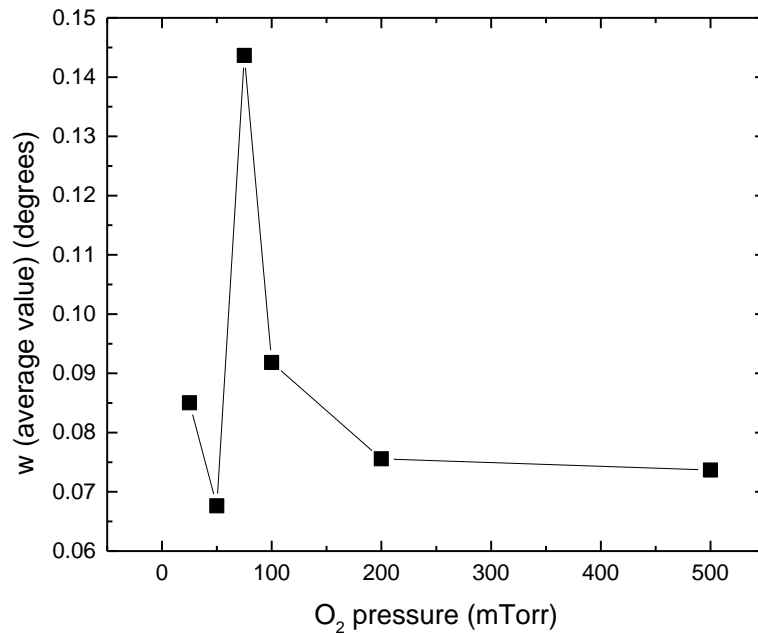


Figure 4.22: Variation of the width of the (002) peak with oxygen pressure for films deposited at substrate temperature 825°C

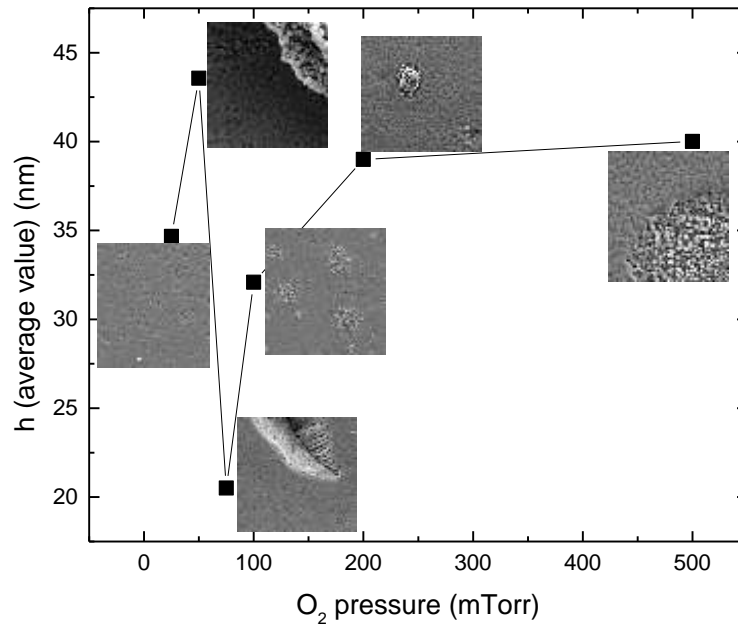


Figure 4.23: Variation of the average grain height h as a function of oxygen pressure for films deposited at substrate temperature 825°C

The above figures 4.22 and 4.23 demonstrate the variation of the FWHM of the XRD (002) peak and the average *out-of-plane* grain height h with background oxygen pressure, respectively. Obviously, most of the ZnO films especially those deposited at 50 mTorr, 200 mTorr and 500 mTorr exhibit a better crystal quality, for the FWHM of their (002) XRD peak is the smallest and consequently the average *out-of-plane* grain size is the largest. The samples at 25 mTorr and 100 mTorr can also be considered to possess great crystallinity. Surprisingly, the sample at 75 mTorr stands out from other samples; it has a poorer crystal quality compared to the rest of the samples in this set, this is indicated by it possessing the smallest grain size (i.e. largest FWHM).

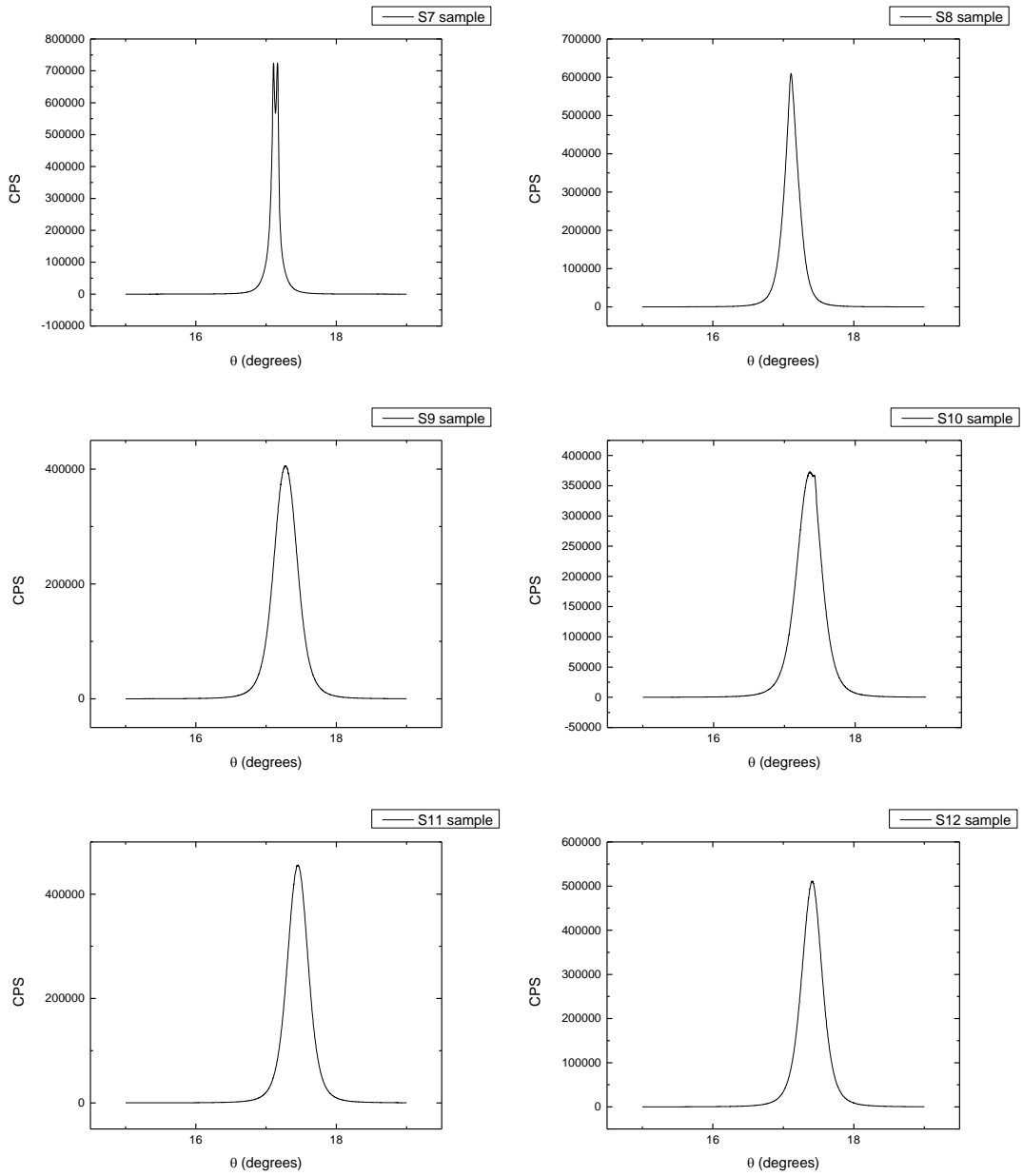


Figure 4.24: Rocking curves of S7, S8, S9, S10, S11 and S12 samples; the ZnO films deposited at 25, 50, 75, 100, 200, and 500 mTorr of oxygen pressure, respectively

Sample	Pressure (mTorr)	ω_r
S7	25	0.113
S8	50	0.205
S9	75	0.339
S10	100	0.354
S11	200	0.307
S12	500	0.305

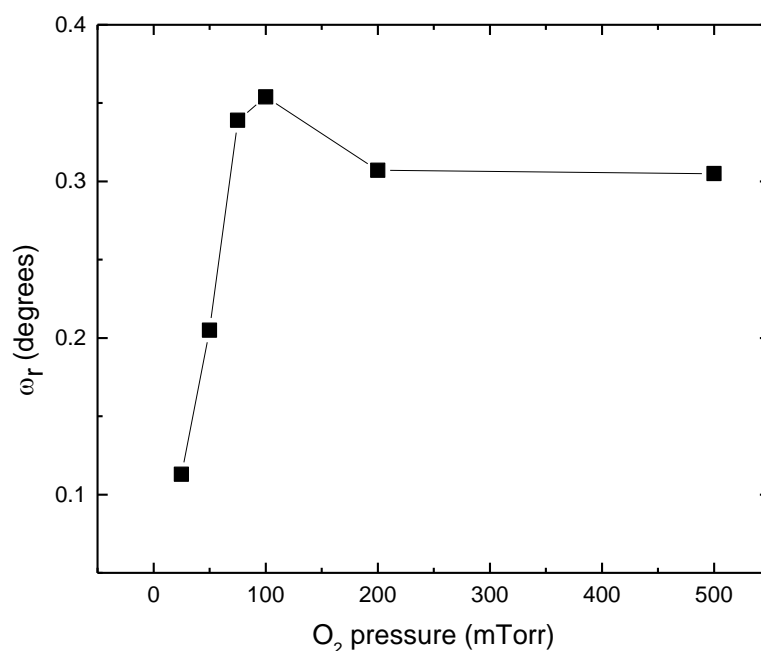
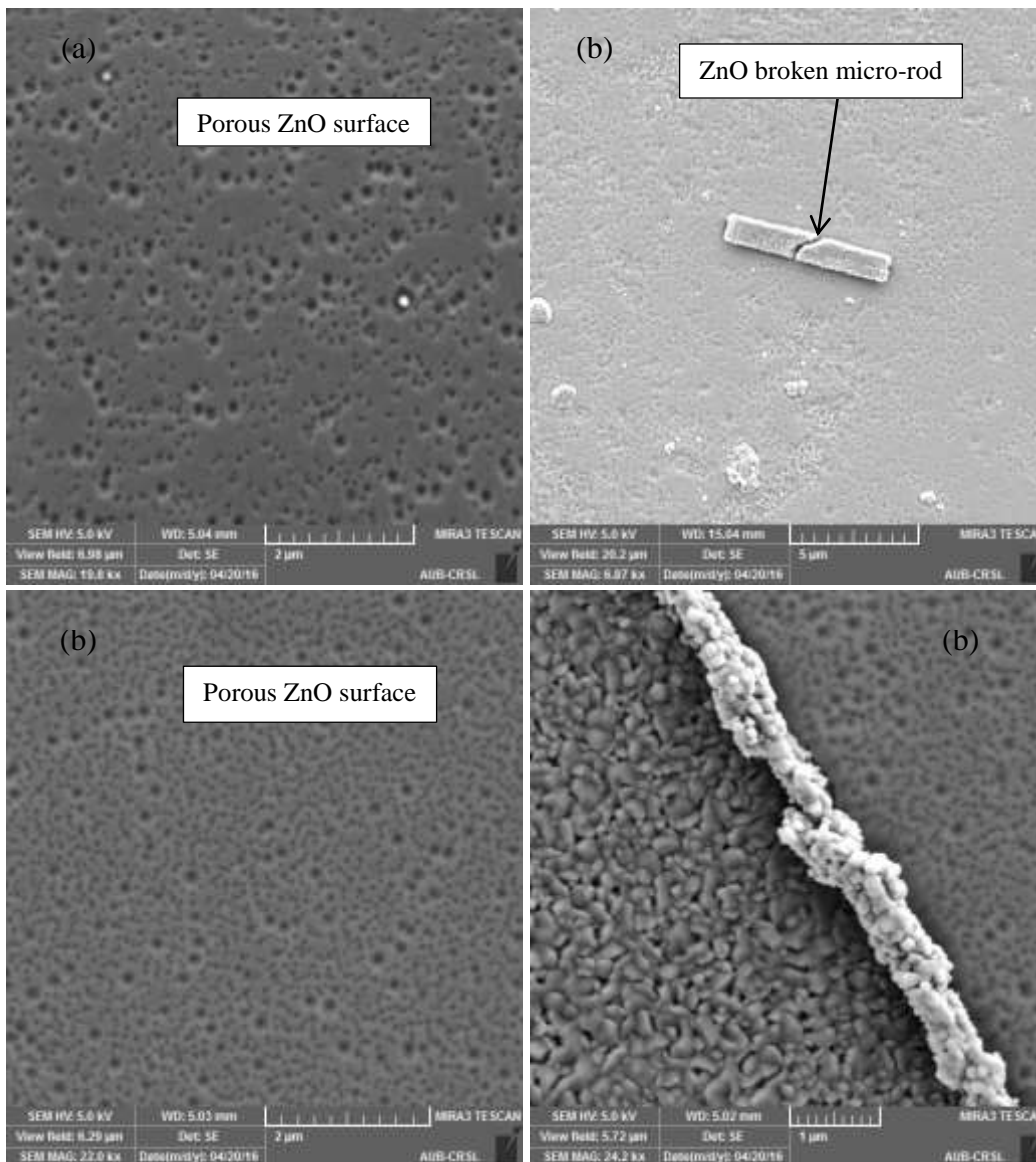


Figure 4.25: Variation of the FWHM rocking curves as a function of oxygen pressure, for films deposited at a substrate temperature of 825°C

In this set of samples, the FWHM rocking curve increases with increasing oxygen pressure (Figure 4.25), where it reaches a maximum value of 0.35° at 100 mTorr and then slightly decreases to an almost constant value of ~0.31° at 200 mTorr and 500 mTorr. The smallest value ($\omega_r=0.11^\circ$) is obtained for the ZnO film deposited at an oxygen pressure of 25 mTorr (S7 sample), hence expressing the best crystalline quality for this ZnO film compared to the rest of the samples in this set. The analysis from the (002) XRD peak does not prove this result, and the reason for this disagreement requires further investigation. Notice that the rocking curve of the 25 mTorr-deposited sample shows a double peak, and the possible reason for this occurrence, as discussed in section 4.3, is the presence of domains in the film probably due to low-angle boundary defects.

4.4.2. SEM images and discussion



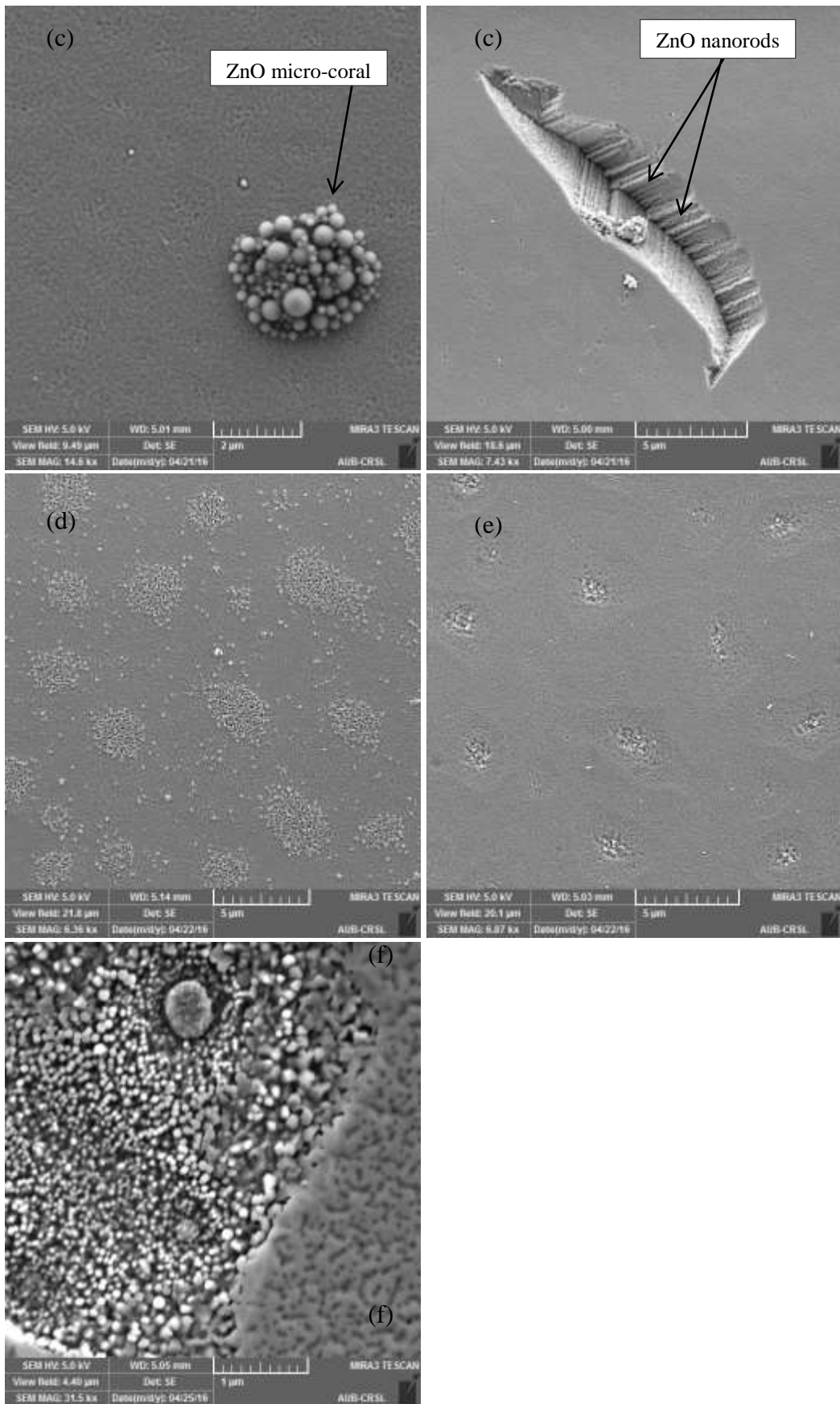


Image 4.3: SEM images of S7, S8, S9, S10, S11 and S12 samples, the ZnO film deposited at (a) 25, (b) 50, (c) 75, (d) 100, (e) 200 and (f) 500 mTorr of oxygen pressure respectively, and 825°C of substrate temperature

For all the ZnO films deposited at various oxygen pressures and at a substrate temperature of 825°C, the roughness is observed to be more or less the same; the surface of S10 sample (100 mTorr oxygen pressure) might be considered to be rougher than the rest, as it contains islands of ZnO nano-grains, in addition to a side of S12 sample (500 mTorr) which has a grained surface, unlike the other side which is much smoother. The film deposited at 25 mTorr and 50 mTorr of oxygen pressure (S7 and S8 samples respectively) possess a smooth porous surface with some interesting ZnO nanostructures, such as ZnO micro-rods atop. As for the film deposited at an oxygen pressure of 75 mTorr, it's surface is considered to be smooth, however, it consisted of some cracks that revealed the inner structures in the film which are clearly ZnO nano-rods. S10 sample (100 mTorr of oxygen pressure) as previously stated had ZnO nano-grains atop of its smooth surface while S11 sample (200 mTorr of oxygen pressure) had a smooth surface with finger-like prints on it. Finally, the film deposited at an oxygen pressure of 500 mTorr also possesses a smooth surface and hexagonal nano-rods are revealed at a certain location on the surface.

4.4.3. EDX results and analysis

Table 4.11: The atomic composition of films deposited at different background oxygen pressures and substrate temperature 825°C

Sample	Pressure	SEM-EDX			
		atomic % Zn	atomic % O	atomic ratio	atomic % C
S7	25 mTorr	46.55	53.45	0.871	0
S8	50 mTorr	48.74	51.26	0.951	0
S9	75 mTorr	50	50	1.000	0
S10	100 mTorr	49.27	50.73	0.971	0
S11	200 mTorr	50.74	49.26	1.030	0
S12	500 mTorr	48.95	51.05	0.959	0

where the atomic ratio = $\frac{\text{atomic \% Zn}}{\text{atomic \% O}}$

An even composition of zinc and oxygen atoms in the films is found by EDX measurements, where the atomic ratio of zinc to oxygen atoms is less than but close to one and in some samples it reaches one. Note that the EDX ranges selected above might affect the results, for they are not the same, however, we can say that there are no major oxygen and zinc deficiencies in all films deposited at various background oxygen pressures.

4.4.4. Thickness measurements

The surface profilometer was used to measure the thickness of the deposited films under various oxygen pressures and at a fixed substrate temperature of 825°C. The results are shown in the graph below.

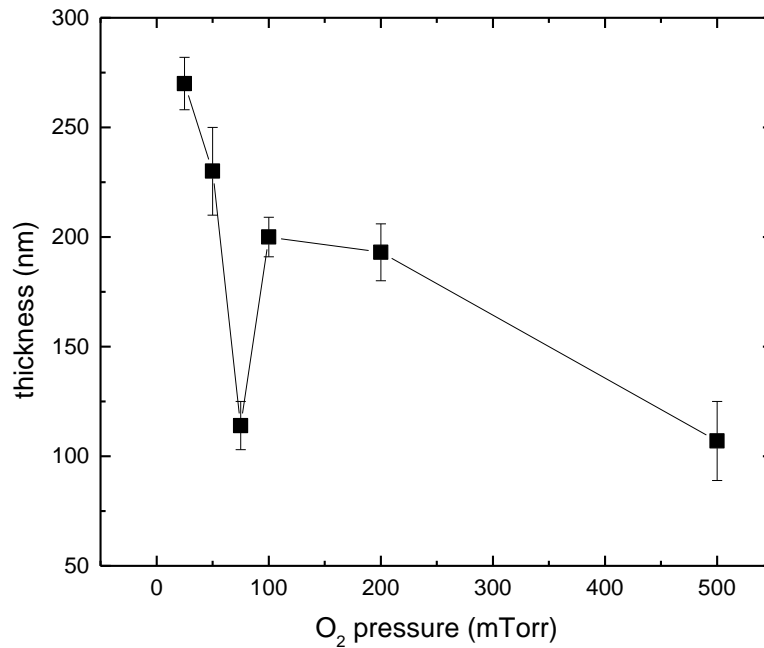


Figure 4.26: Variation of the thickness of the films deposited at different background oxygen pressures and substrate temperature 825°C

There is a clear decreasing trend in the thickness of the ZnO thin films as the oxygen pressure increases. Reasonably, this should be the case, since at high oxygen pressures the plasma plume (containing the Zn and O ablated atoms) experiences more collisions with the surrounding oxygen (O₂) atoms, limiting its expansion towards the sapphire substrate and hence fewer ZnO layers would be deposited. There is a surprising decrease in thickness for the ZnO film deposited at 75 mTorr, which is due to unknown reasons, and recall that this sample had the poorest crystalline quality.

4.4.5. Optical Properties

The UV-VIS spectrometer delivered the reflectance spectra of the samples deposited at a fixed substrate temperature of 825°C and at various oxygen pressures. The spectra are shown in figure 4.27.

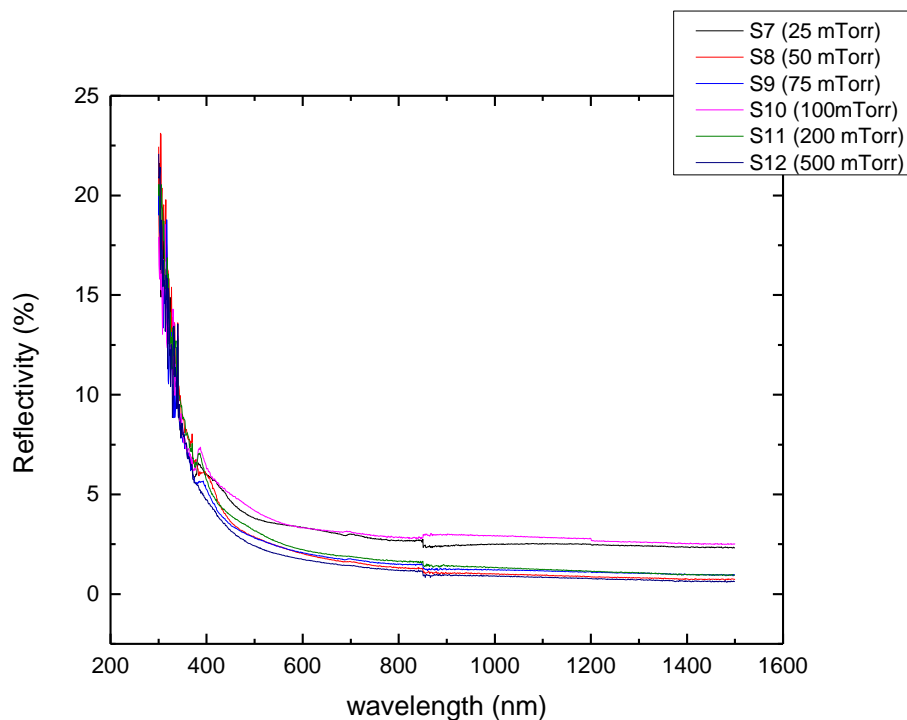


Figure 4.27: Reflectance spectra of ZnO films deposited at different oxygen pressures and substrate temperature 825°C

The reflectivity of the near infrared and visible radiation by all six samples is very small, below 5% (figure 4.27), which implies that over this wide wavelength range (1500 nm- 450 nm) transmission of radiation takes place, explaining our observation of these extremely transparent samples. The reflectivity data has been used to calculate the energy loss function of each sample and their smoothed envelope is plotted in figure 4.28.

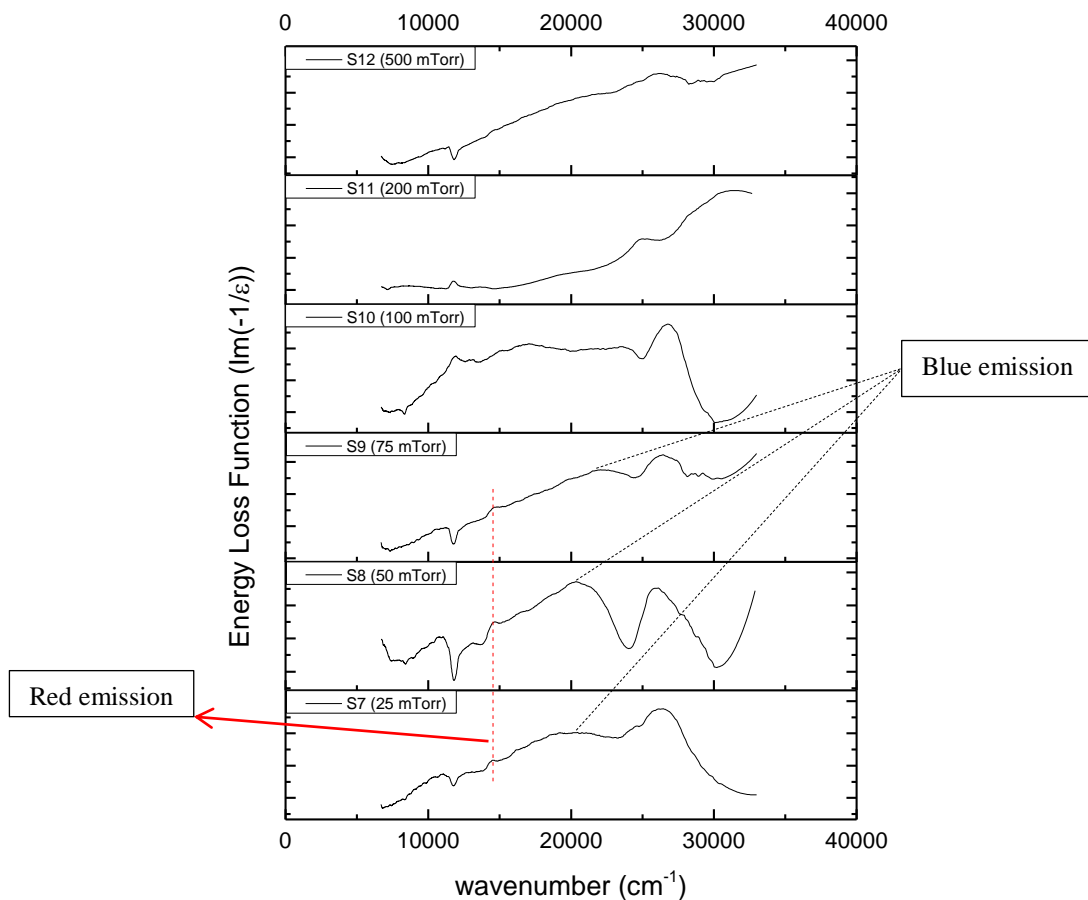


Figure 4.28: Energy loss functions of ZnO films deposited at different oxygen pressures, and 825°C substrate temperature

The pronounced UV peak centered at ~ 370 nm corresponds to the band edge emission. For the three samples deposited at 25 mTorr, 50 mTorr and 75 mTorr, a small red emission is observed, presented by a small peak at a wavenumber of ~ 14532 cm^{-1} (~ 688 nm), besides to a broad blue emission, which is much pronounced for the 50 mTorr-deposited sample.

Notice that in the energy loss function of S11 sample, the film deposited at 200 mTorr of oxygen pressure, there is an increasing trend of peaks beyond the position of the band gap (below 400 nm), this is an evidence of the existence of excitons in the film. In other materials than ZnO, excitons cannot exist at room temperature because in most cases the thermal energy $3kT/2$ ($T \sim 300$ K and k is the Boltzmann constant) is

much greater than the binding energy of the excitons which leads to its dissociation; however, in the case of zinc oxide the exciton's binding energy is $60 \text{ meV} \gg 3kT/2$ ($\sim 39 \text{ eV}$), which allows the excitons to exist at room temperature (as in the case of S11 sample (200 mTorr)).

Table 4.12: Band gap energy values for films deposited at different oxygen pressures and substrate temperature 825°C

Sample	Pressure	Energy	Temp	RepRate	Band gap (eV)	Error (eV)
S7	25 mTorr	400 mJ	825°C	20 Hz	3.26	0.04
S8	50 mTorr	400 mJ	825°C	20 Hz	3.22	0.04
S9	75 mTorr	400 mJ	825°C	20 Hz	3.28	0.04
S10	100 mTorr	400 mJ	825°C	20 Hz	3.32	0.04
S11	200 mTorr	400 mJ	825°C	20 Hz	3.122	0.026
S12	500 mTorr	400 mJ	825°C	20 Hz	3.26	0.06

For this set of samples, the band gap has been varied from 3.12 eV to 3.32 eV, however, except for S11 sample which had the smallest band gap value, the variation in the band gap values with oxygen pressure is said to be within the experimental error.

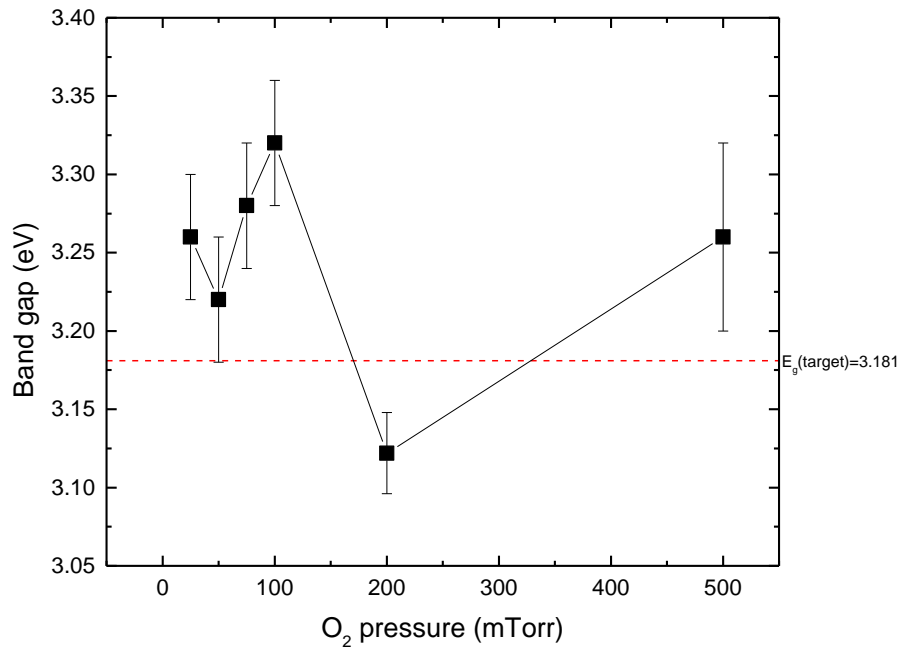


Figure 4.29: Variation of the band gap energy value as a function of oxygen pressure for films deposited at substrate temperature 825°C

To explain the origin of the blue and red emissions observed in the energy loss functions above, we have followed a paper by S. Zhao et al. (2006) to correlate these emissions with possible point defects in the sample. In their paper they presented the following diagram shown in figure 4.30, calculated by the full-potential linear muffin-orbit method (FP-LMTO).

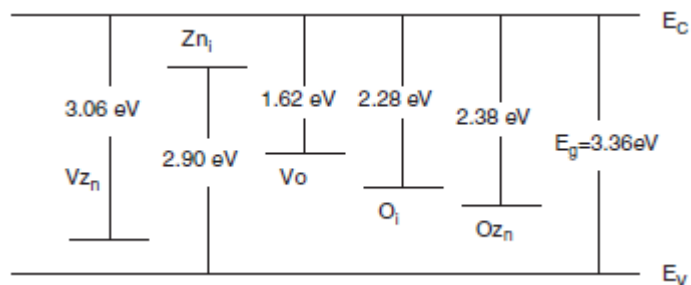


Figure 4.30: Schematic representation of the energy levels of the intrinsic defects in ZnO thin films

The blue emission (500 nm) and the red emission (680 nm) observed in the energy loss functions, correspond to an energy value of ~2.48 eV and 1.82 eV respectively. Lin et al. (2004) have attributed red emission from ZnO thin films to

oxygen vacancies, and comparing to the diagram in figure 4.20 we can conclude that the red emission detected in our three specified samples above (S7, S8 and S9 samples) is due to oxygen vacancies. The type of the point defect causing the blue emission is not clear from figure 4.20; however, in a paper by Wei et al. (2009), blue emission was attributed to zinc interstitials as it is derived from electronic transition from the donor level of zinc interstitial to the valence band, while Lin et al., associated green emission to zinc interstitials. Both authors employed different methods to prepare ZnO thin films; Wei et al. prepared their samples by the pulsed laser deposition technique while Lin et al. used the radio frequency magnetron sputtering technique. Supporting our analysis by similar work done by Wei et al., we can conclude that the strong blue emission observed in S8 sample and S6 sample (section 4.2 (iv)) is due to zinc interstitial defects.

4.5. Effect of Laser Energy

Few works have been done by researchers to test the impact of the laser energy on the quality of the grown ZnO thin films. We have been curious to figure out the effect of the laser energy and for this reason we prepared two samples at conditions summarized in table 4.13.

Table 4.13: Experimental conditions for samples grown at different laser energies, 10 mTorr oxygen pressure and substrate temperature 725°C

Sample name	Temperature (°C)	O ₂ pressure (mTorr)	Laser Energy (mJ)	Repetition Rate (Hz)
S1	725	10	200	20
S0	725	10	400	20

4.5.1. XRD results and analysis

Locked coupled $\theta/2\theta$ scans for samples deposited at different laser energies, confirm that both energies 200 mJ and 400 mJ are suitable in producing ZnO thin films of great crystal quality. This is verified by the strong and extremely narrow peak displayed in both XRD graphs which corresponds to the (002) orientation of the ZnO deposited films, at an angle of $2\theta \sim 34^\circ$, in addition to a small peak, at a diffraction angle $\sim 72^\circ$, corresponding to the (004) orientation (Figure 4.31). The fact that only the (00 l) peaks ($l=2, 4, 6, \dots$) are exhibited in the XRD patterns is an indication that our films deposited at two different laser energies are highly oriented along the z or c-axis.

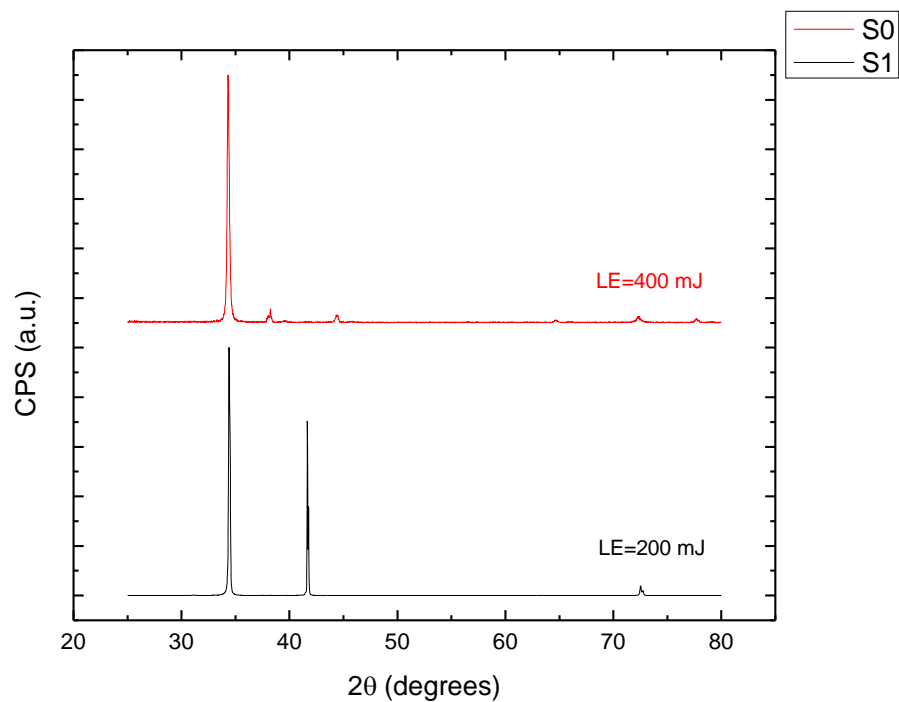


Figure 4.31: $\theta/2\theta$ scans for samples deposited at different laser energies, substrate temperature 725°C and 10 mTorr of oxygen pressure

As discussed in Chapter 3 and was in previous sections followed, the FWHM w of the (002) peak, the average grain size h , the lattice constant ' c ' and the macroscopic strain ϵ were determined and calculated, and the values are listed in table 4.14.

Table 4.14: The lattice constant c , the strain ϵ , the (002) peak width and the average grain height h of films deposited at different laser energies, 10 mTorr oxygen pressure and substrate temperature 725°C

Laser Energy (mJ)	c (Å)	w (degrees)	h (nm)	strain ϵ (%)
200	5.2078 (0.0006)	0.140	21.1	0.07023
400	5.2139 (0.0006)	0.214	13.7	0.18812

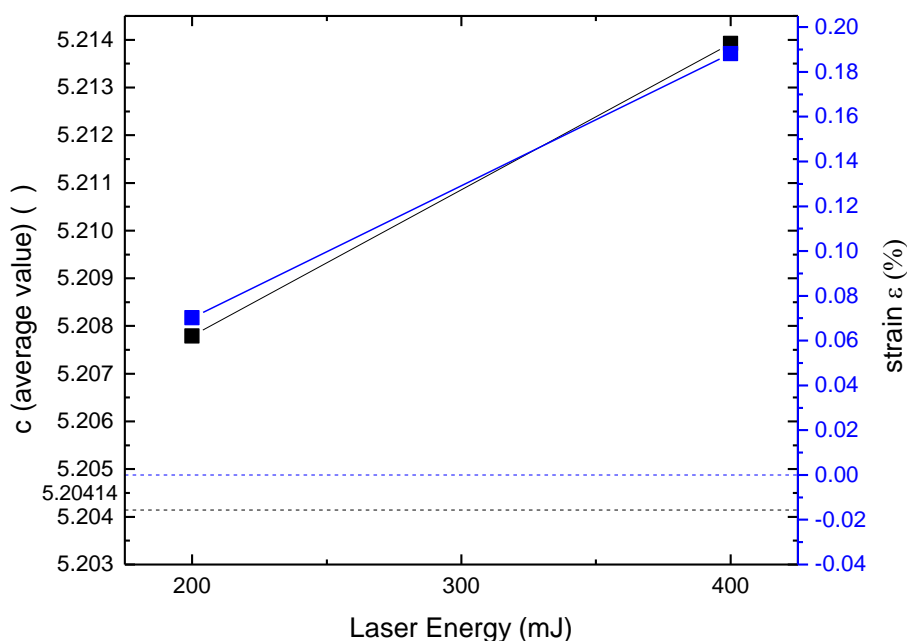


Figure 4.32: Variation of the lattice constant c and the strain ϵ as a function of laser energy for films deposited at 10 mTorr oxygen pressure and substrate temperature 725°C

A notable change in the lattice constant ' c ' and consequently the macroscopic strain ϵ of the samples can be observed as the laser energy varies; for a laser energy of 200 mJ the strain in the sample is extremely small 0.07%, and it increases to 0.19% as the laser energy increases to 400 mJ. The stress in the layers in the films at 400 mJ and 200 mJ is tensile, and it's greater for the ZnO film at 400 mJ. For one to produce a stress-free sample, low energies should be considered.

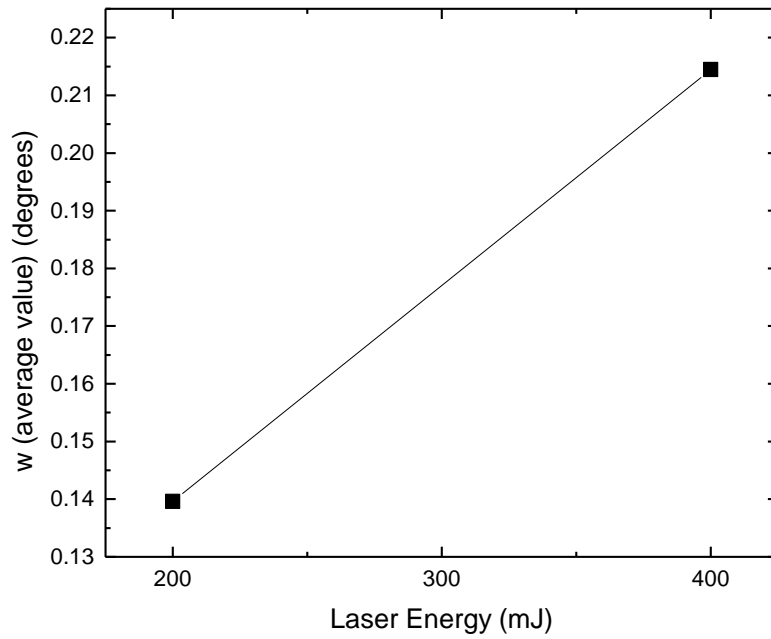


Figure 4.33: Variation of the width of the (002) peak with laser energy for films deposited at 10 mTorr oxygen pressure and substrate temperature 725°C

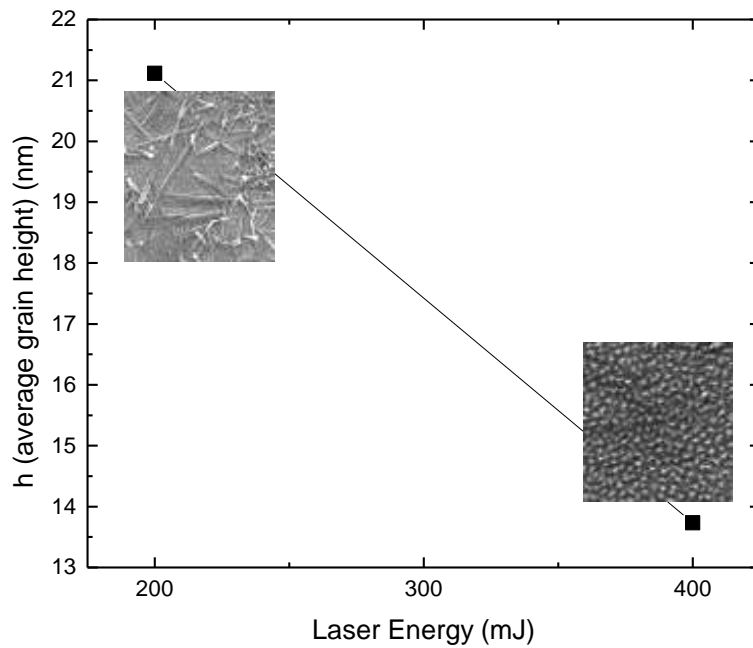


Figure 4.34: Variation of the average grain height h as a function of laser energy for films deposited at 10 mTorr oxygen pressure and substrate temperature 725°C

A change in the FWHM of the XRD (002) peak and the *out-of-plane* grain height h is detected as the laser energy varies. This is exhibited in figures 4.34 and 4.35 above. As shown in these figures, a better crystal quality of the deposited ZnO thin films is obtained at a laser energy of 200 mJ, based on the fact that at this value the FWHM of the (002) peak is the smallest $\sim 0.14^\circ$ and as a result the average *out-of-plane* grain height is the largest ~ 21 nm. As the laser energy increases to 400 mJ the FWHM takes a value of 0.21° and the grain height becomes smaller ~ 14 nm. So from this analysis a laser energy of 200 mJ expresses the best crystallinity of ZnO thin films, keeping in mind that this film was deposited at an oxygen pressure of 10 mTorr, substrate temperature 725°C and laser repetition rate 20 Hz.

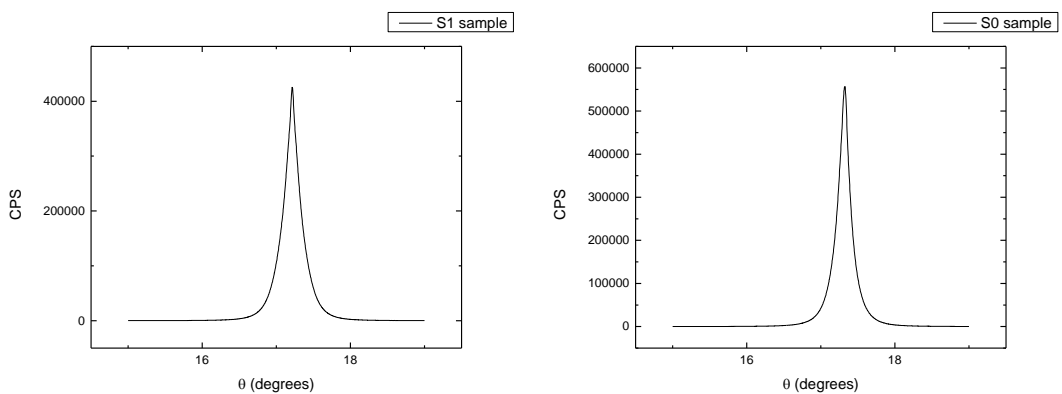


Figure 4.35: Rocking Curves of S1 and S0 samples; the ZnO films deposited at laser energy of 200 mJ and 400 mJ respectively

Sample	Laser Energy (mJ)	ω_r
S1	200	0.249
S0	400	0.193

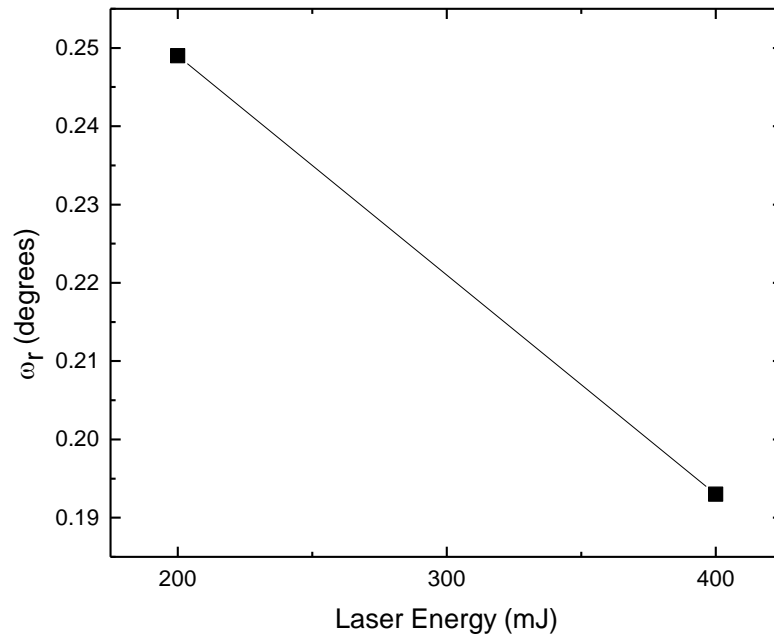


Figure 4.36: Variation of the FWHM rocking curves as a function of laser energy, for films deposited at 10 mTorr of oxygen pressure and 725°C of substrate temperature

The FWHM rocking curve for the ZnO film deposited at laser energy of 400 mJ is (0.19°) smaller than one deposited at 200 mJ (0.25°); this proves that the crystalline quality of the former sample is better. This disagrees with the previous conclusion, where we have obtained a better crystallinity for the 200 mJ deposited sample. To find the reasons of this disagreement, it requires further investigation. However, judging from the rocking curves, a laser energy of 400 mJ produces ZnO thin films with better crystalline quality than 200 mJ laser energy.

4.5.2. SEM images and discussion

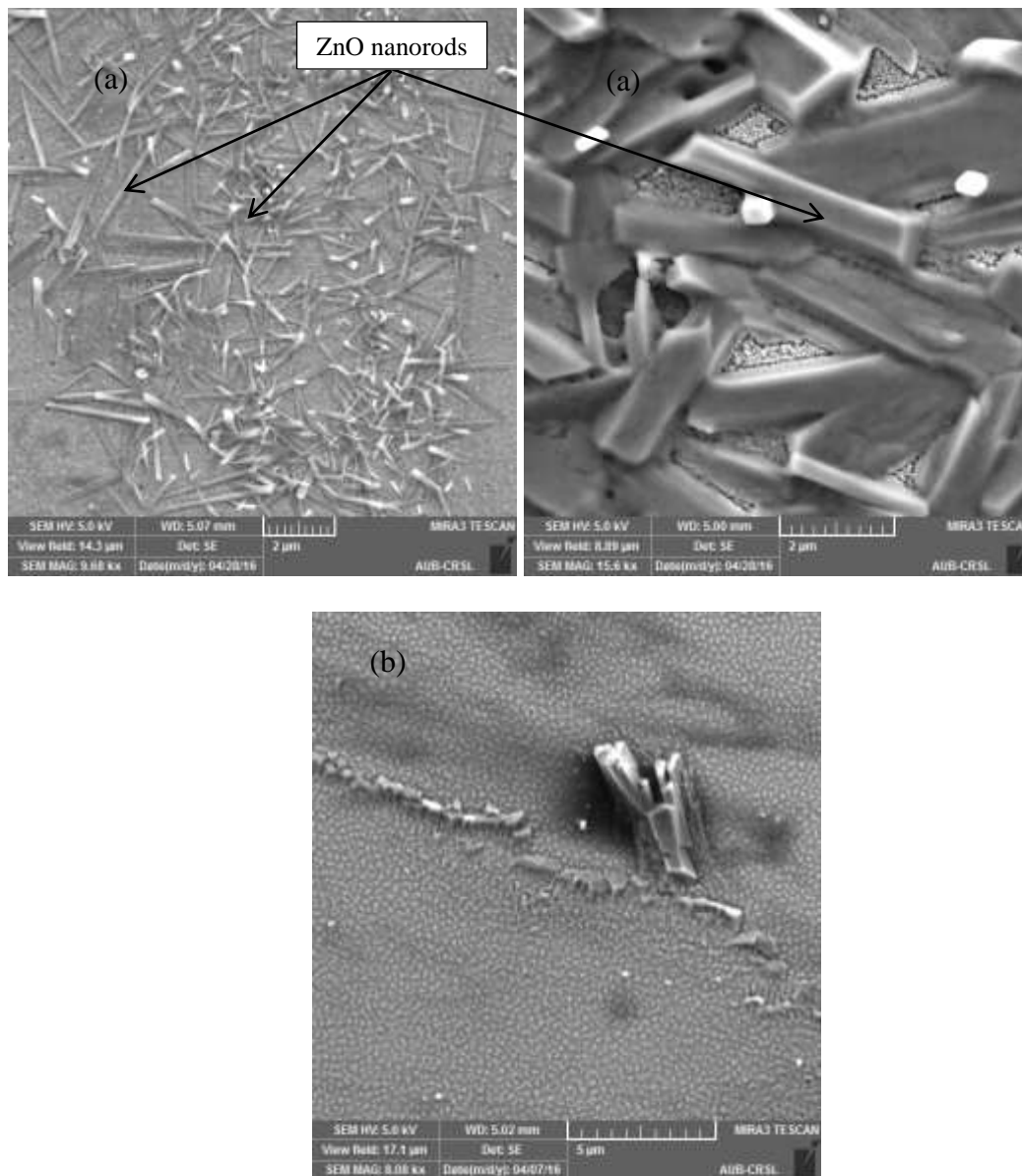


Image 4.4: SEM images of S1 and S0 samples, the ZnO films deposited at a laser energy of (a) 200 and (b) 400 mJ respectively, 10mTorr of oxygen pressure and 725°C of substrate temperature

The morphology of the film deposited at laser energy of 200 mJ is different than the film deposited at 400 mJ. The former one is observed to have a smooth surface and ZnO nano-rods are seen on its top. As previously discussed in sections 4.2 and 4.3 the ZnO film deposited at laser energy of 400 mJ (S0 sample) consists of a grained surface.

4.5.3. EDX results and analysis

Table 4.15 summarizes the EDX measurements.

Table 4.15: The atomic composition of films deposited at different laser energies, 10 mTorr oxygen pressure and substrate temperature 725°C

Sample	Laser Energy	SEM-EDX			
		atomic % Zn	atomic % O	atomic ratio	atomic % C
S1	200 mJ	48.86	51.14	0.955	0
S0	400 mJ	40.08	40.88	0.980	19.04

where the atomic ratio = $\frac{\text{atomic \% Zn}}{\text{atomic \% O}}$

The above EDX results show that the film deposited at a higher laser energy (400 mJ) has an enhanced atomic ratio of zinc atoms to oxygen atoms than the one deposited at a lower laser energy (200 mJ), this is due to the fact that higher laser energies are capable of ablating more atoms (Zn and O atoms) from the ZnO target. The atomic ratio of S0 sample (400 mJ) is closer to one than S1 sample (200 mJ).

4.5.4. Optical Properties

The reflectance spectra of the films deposited at two different laser energies has been collected by the UV-VIS spectrometer and is shown in figure 4.37.

The figure shows that both samples are extremely transparent, since the reflectivity of both thin films in the near infrared and visible spectrum is very low (less than 2%)

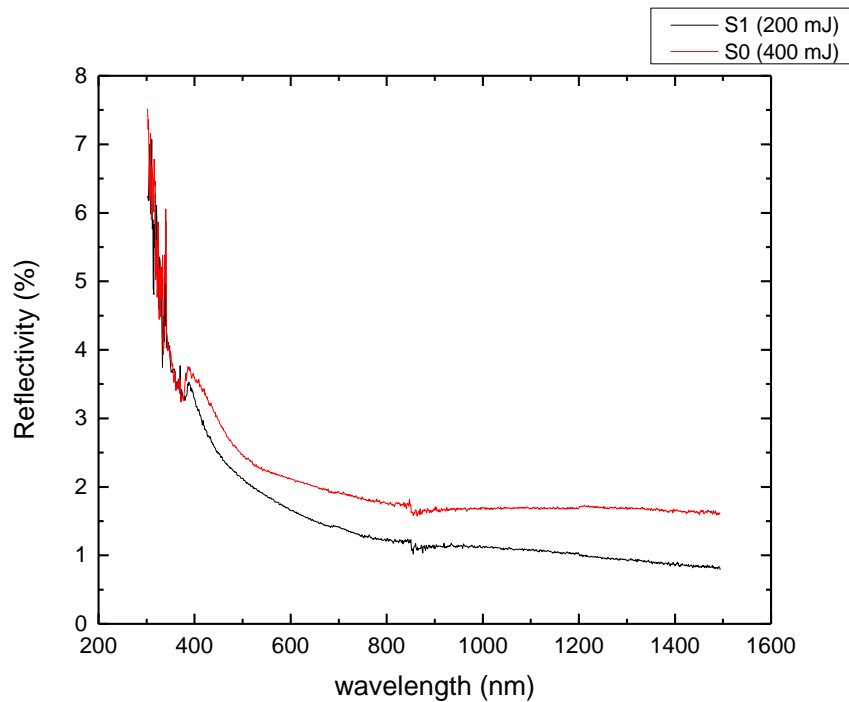


Figure 4.37: Reflectance spectra of ZnO films deposited at different laser energies, 10 mTorr oxygen pressure and substrate temperature 725°C

Using the above experimental data the energy loss functions were computed by the Kramers-Kronig model and the band gap of the samples was determined and listed in table 4.16.

One dominant and pronounced peak centered at around 370 nm is observed in the energy loss functions of both samples (figure 4.38), which is a UV emission corresponding to the near band edge emission. These peaks locate the position of the band gap of the samples. Clearly, no major defects exist; a very small peak is observed in the energy loss function of the sample deposited at 400 mJ, it is centered at 490 nm i.e. it's a blue emission. This defect emission may be due to zinc interstitial defects (as discussed in section 4.4).

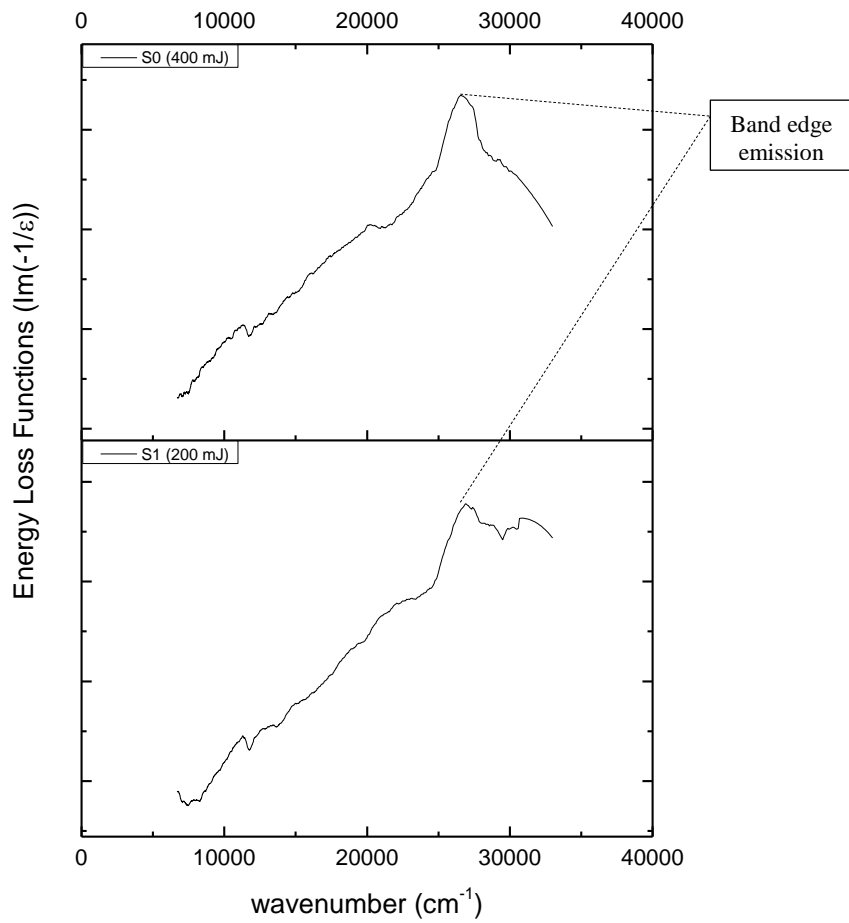


Figure 4.38: Energy loss functions of ZnO films deposited at different laser energies, 10 mTorr oxygen pressure and substrate temperature 725°C

Table 4.16: Band gap energy values for films deposited at different laser energies, 10 mTorr oxygen pressure and substrate temperature 725°C

Sample	Pressure	Energy	Temp	RepRate	Band gap (eV)	Error (eV)
S1	10 mTorr	200 mJ	725°C	20 Hz	3.34	0.04
S0	10 mTorr	400 mJ	725°C	20 Hz	3.30	0.04
Target					3.181	0.026

The variation in the band gap energy of the two samples is within the experimental error and is said to be negligible. As a conclusion, the laser energy has no considerable effect on the band gap energy of the deposited ZnO films.

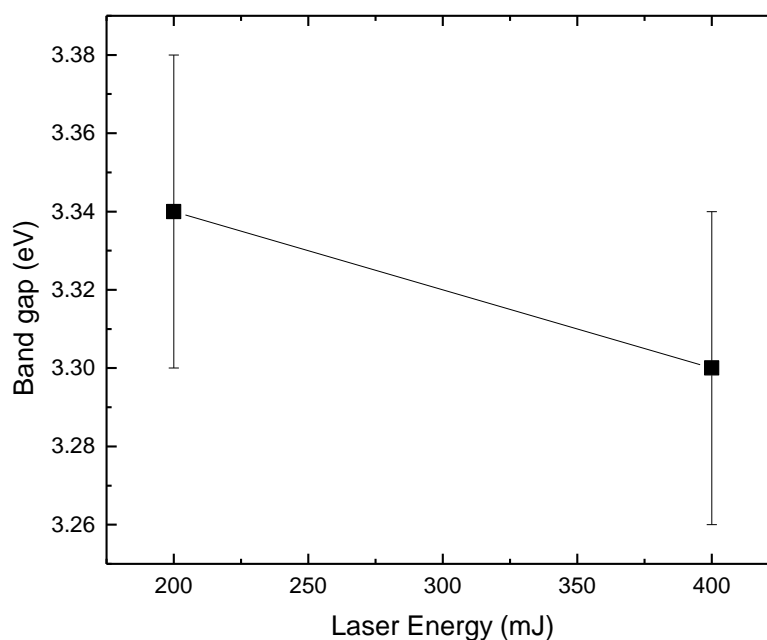


Figure 4.39: Variation of the band gap energy value as a function of laser energy, for films deposited at 10 mTorr of oxygen pressure and 725°C of substrate temperature

4.6. Effect of Laser Repetition Rate

The effect of the laser repetition rate on the quality of the deposited ZnO thin films has not been investigated. Much work was conducted at low repetition rates, such as 5 Hz and 10 Hz, and so to study the influence of higher laser repetition rates on the grown ZnO thin films, we deposited two samples under conditions summarized in table 4.17.

Table 4.17: Experimental conditions for samples grown at different laser repetition rates, 10 mTorr oxygen pressure and substrate temperature 725°C

Sample name	Temperature (°C)	O ₂ pressure (mTorr)	Laser Energy (mJ)	Repetition Rate (Hz)
S0	725	10	400	20
S4	725	10	400	50

4.6.1. XRD results and analysis

The XRD diffractograph in figure 4.40 reveals that both ZnO films deposited at different laser repetition rates have an excellent crystalline quality. This is ensured by a dominant and a very narrow peak presented at a diffraction angle of $2\theta \sim 34^\circ$ due to reflections from the (002) planes, in addition to a small peak at around 72° corresponding to reflections from the (004) planes. From these $\theta/2\theta$ scans and the display of the (00 l) ($l=2, 4\dots$) peaks we can conclude that both films are highly crystallized and oriented along the c-axis. Using the EVA software and matching the scans with sapphire (Al_2O_3) XRD patterns from the database, we found that the small peaks appearing at diffraction angles $2\theta \sim 38.27^\circ, 44.36^\circ$ and 77.75° correspond to the (110), (113), and (119) reflections from the sapphire substrate, respectively (Appendix B).

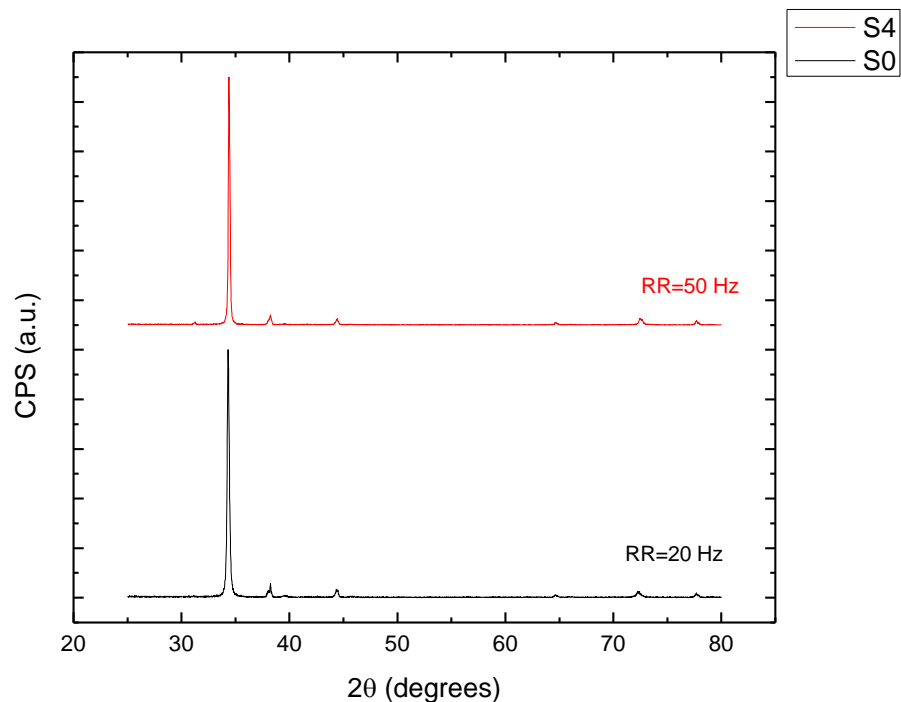


Figure 4.40: $\theta/2\theta$ scans for samples deposited at different laser repetition rates, substrate temperature 725°C and 10 mTorr oxygen pressure

The position and width of the (002) XRD peak were determined as explained in Chapter 3, and they were used to calculate the average grain size h , the lattice constant ' c ' and the macroscopic/average strain ϵ . The variation of these parameters as a function of laser repetition rate was then plotted.

Table 4.18: The lattice constant c , the strain ϵ , the (002) peak width and the average grain height h of films deposited at different laser repetition rates, 10 mTorr oxygen pressure and substrate temperature 725°C

Repetition Rate (Hz)	c (Å)	w (degrees)	h (nm)	strain ϵ (%)
20	5.2139 (0.0006)	0.214	13.7	0.18812
50	5.2102 (0.0006)	0.082	36	0.11645

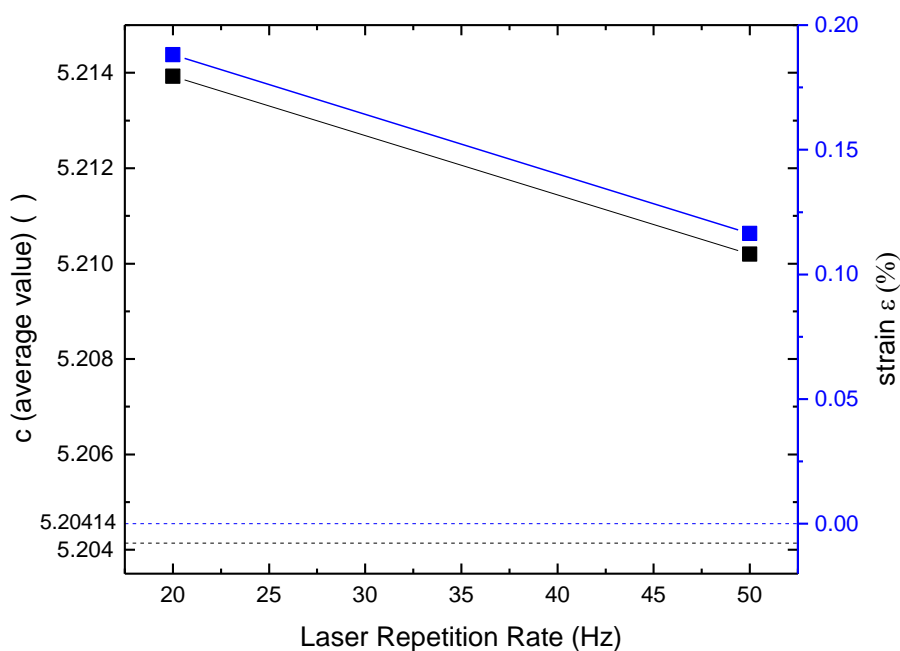


Figure 4.41: Variation of the lattice constant c and the strain ϵ as a function of laser repetition rate for films deposited at 10 mTorr oxygen pressure and substrate temperature 725°C

There is no significant variation in the ' c ' value or the average strain ϵ with the variation in laser repetition rate. This is demonstrated in figure 4.41. Under the conditions of 10 mTorr of background oxygen pressure, 725°C substrate temperature

and 400 mJ as laser energy, the strain in the layers of the ZnO films decreases slightly from ~0.19% at 20 Hz to 0.12% at 50 Hz.

We can compare our results to those obtained by Nie et al. although their depositions parameters are different than ours, 640°C substrate temperature, 20 mTorr oxygen pressure and 5 Hz repetition rate, they were able to produce highly c-axis oriented films of different thicknesses, also evidenced by the appearance of a strong (002) peak in their diffraction pattern. They varied their thickness by increasing the deposition time, however here in our case the thickness was varied by increasing the repetition rate. They also used the position of this peak to calculate the lattice constant 'c', grain size d, and strain ϵ , and similar to our results they obtained low values for the strain; in their case for a film thickness of 200 nm the strain had an equal but opposite value (-0.19 %) to our strain at this thickness; their strain is compressive, ours is tensile and this is affected by the deposition parameters chosen.

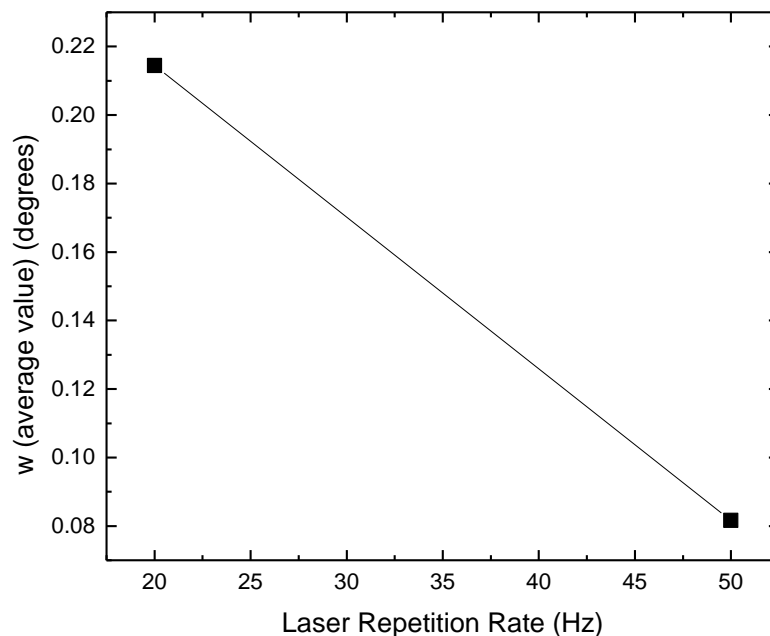


Figure 4.42: Variation of the width of the (002) peak with laser repetition rate for films deposited at 10 mTorr oxygen pressure and substrate temperature 725°C

Unlike, the variation of lattice constant 'c' and the macroscopic strain ϵ with laser frequency, the laser repetition rate has a remarkable impact on the FWHM of the XRD (002) peak and consequently the average grain size h , calculated using Scherrer's equation. This is shown in figures 4.42 and 4.43 respectively. Clearly, as the repetition rate increases to 50 Hz, the FWHM w decreases significantly from 0.21° at 20 Hz to 0.08° at 50 Hz, as a result since the FWHM of the (002) peak and the average grain size h are inversely proportional, the grain size h increases considerably from 14 nm to 36 nm. Therefore, a better crystallinity of ZnO films is obtained at high repetition rates.

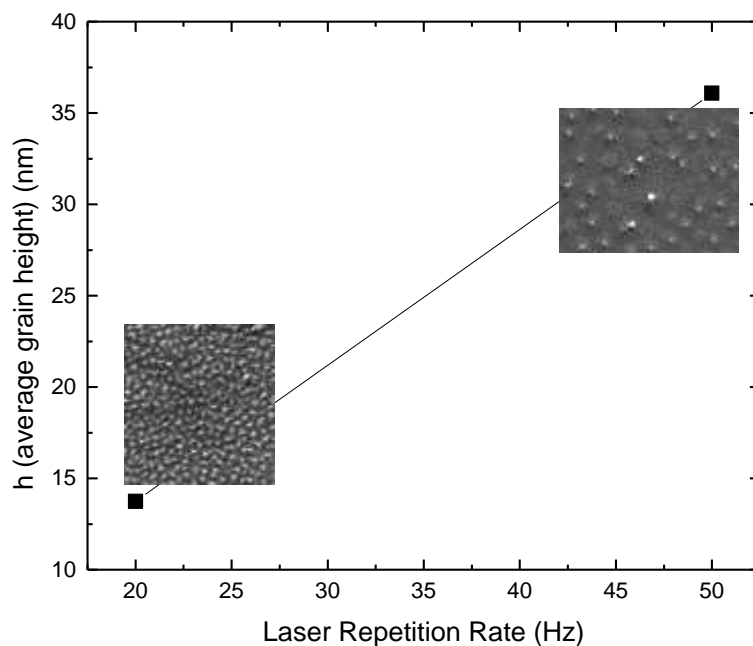


Figure 4.43: Variation of the average grain height h as a function of laser repetition rate for films deposited at 10 mTorr oxygen pressure and substrate temperature 725°C

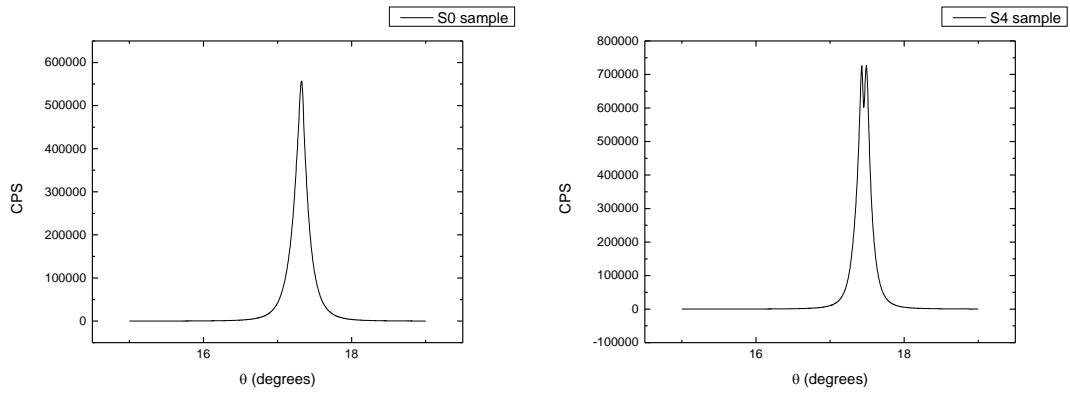


Figure 4.44: Rocking curves of S0 and S4 samples; the ZnO films deposited at a laser repetition rate of 20 Hz and 50 Hz respectively

Sample	Repetition Rate (Hz)	ω_r
S0	20	0.193
S4	50	0.182

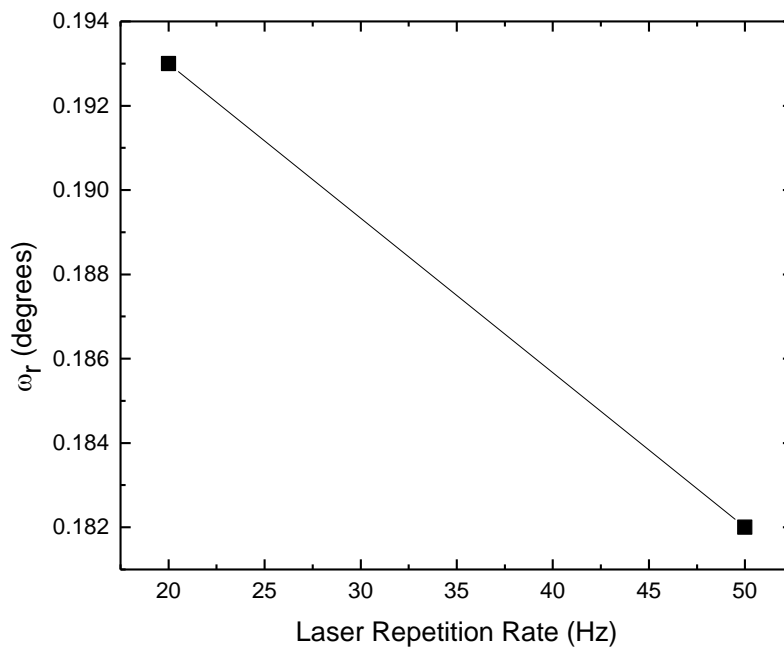


Figure 4.45: Variation of the FWHM rocking curves as a function of laser repetition rate, for films deposited at 10 mTorr of oxygen pressure and 725°C of substrate temperature

From figure 4.45 we can notice that there is no significant variation in the FWHM rocking curve of both samples, the ZnO films deposited at laser repetition rates of 20 Hz and 50 Hz, they have a value ω_r of 0.19° and 0.18° respectively; hence both

films express a good crystalline quality. However, it is important to note that the rocking curve of S4 sample (the thin film deposited at laser repetition rate of 50 Hz) shows a double peak, similar to the graph obtained in S7 sample (Section 4.4). Reasonably, the same reasoning applies here too; the film might possess domains that are possibly formed from low-angle boundary defects.

4.6.2. Thickness measurements

The thickness of the samples deposited at two different repetition rates is shown in the graph below.

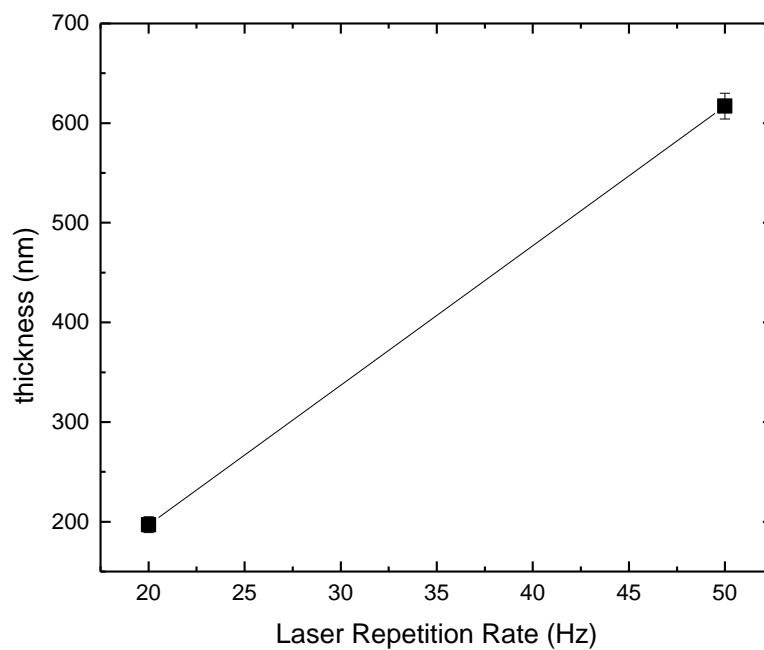


Figure 4.46: Variation of the thickness of the films deposited at different laser repetition rates, 10 mTorr oxygen pressure and substrate temperature 725°C

An enormous increase in thickness is noticed as the repetition rate increases to 50 Hz. In fact, for a laser repetition rate of 20 Hz the thickness of the ZnO films was around 200 nm and tripled to around 620 nm for a repetition rate of 50 Hz. This is not

surprising since as the repetition rate increases, the ZnO target is being more ablated by the laser, consequently more species (Zn and O species) are coming out from the target and the plume is much denser. Hence for a fixed deposition time more species and layers are deposited on the substrate at high repetition rates (50 Hz in our case).

From figure 4.43 and 4.46 we can say that as the film thickness increases the average out-of-plane grain size or height h increases, this is in agreement with what Nie et al. arrived at, a significant increase in the out-plane grain size (h) as the thickness increases.

4.6.3. SEM images and discussion

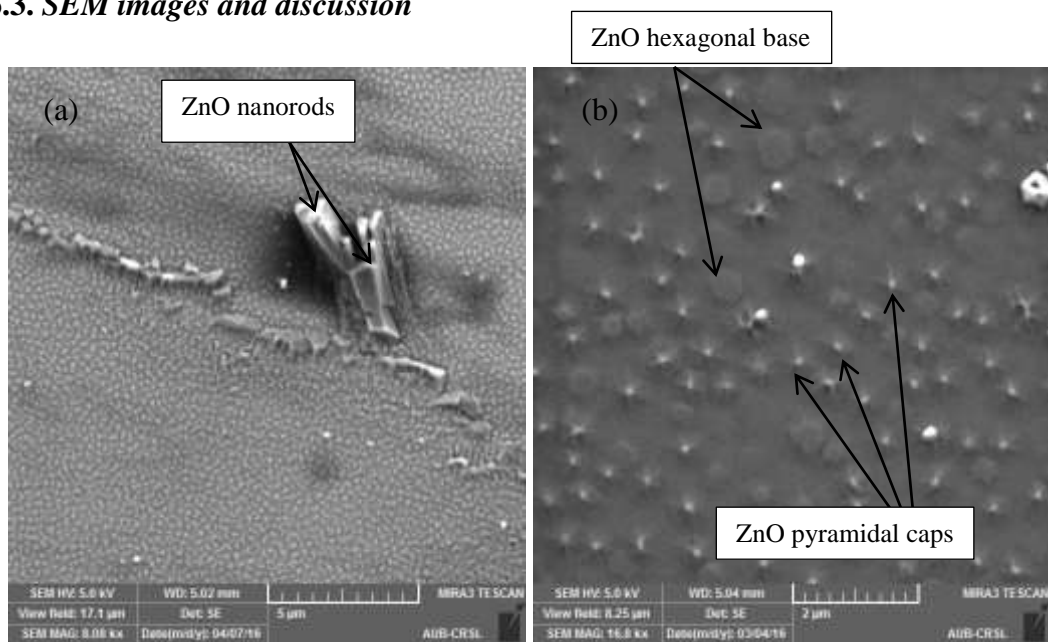


Image 4.5: SEM images of S0 and S4 sample, the ZnO films deposited at a repetition rate of (a) 20 and (b) 50 Hz, respectively, 10 mTorr of oxygen pressure and 725°C of substrate temperature

Clear zinc oxide hexagons and pyramidal caps are seen on the surface of the film deposited at a repetition rate of 50 Hz; this ensures the 'wurtzite' hexagonal crystal nature of our films and the formation of ZnO micro and nanorods in the film.

Previously, by XRD analysis, we have discussed that the film deposited at a laser repetition rate of 20 Hz holds smaller *out-of-plane* grains, than the film deposited at 50 Hz. SEM images for S0 sample (i.e. the ZnO film at 20 Hz) reveal smaller *in-plane* grains, roughly 100-200 nm, than S4 sample (i.e. the ZnO film at 50 Hz) where the ZnO hexagons and caps are larger, around one micron or half a micron. As a conclusion, the laser repetition rate significantly influences the ZnO grain size, both the *out-of-plane* and the *in-plane* grain size, and therefore as the repetition rate increases the crystallinity of the deposited films is greatly enhanced.

Nie et al. obtained similar results of hexagonal structures of the films by SEM images, confirming as in our case the ‘wurtzite’ hexagonal crystal nature of the ZnO films produced, the hexagonal structures were observed at a thickness of 200 nm, while in our case these nanostructures appeared at a thickness of around 617 nm. Of course the morphology of the deposited ZnO films is affected by the deposition parameters in charge.

4.6.4. EDX results and analysis

Table 4.19: The atomic composition of films deposited at different laser frequencies, 10 mTorr oxygen pressure and substrate temperature 725°C

Sample	Repetition Rate	SEM-EDX		
		atomic % Zn	atomic % O	atomic ratio
S0	20 Hz	40.08	40.88	0.980
S4	50 Hz	49.06	50.94	0.963

where the atomic ratio = $\frac{\text{atomic \% Zn}}{\text{atomic \% O}}$

The atomic composition of the films deposited at two different repetition rates (20 Hz and 50 Hz) has an almost equal percentage of zinc and oxygen atoms, which ensures that there are no oxygen or zinc vacancies in the films.

4.6.5. Optical Properties

By the UV-VIS spectroscopy technique the reflectance spectra of the films deposited at two different repetition rates of the laser was scanned.

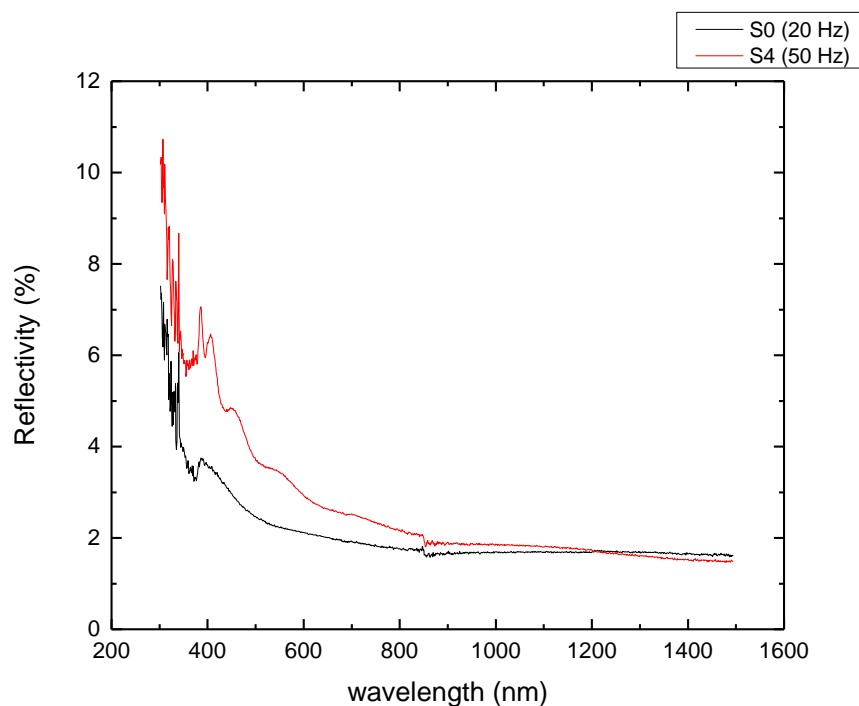


Figure 4.47: Reflectance spectra of ZnO films deposited at different laser frequencies, 10 mTorr oxygen pressure and substrate temperature 725°C

Over the near infrared and visible range, the reflectivity of the ZnO thin film deposited at 20 Hz is extremely small (below 3 %) which explains its transparency, while the one deposited at 50 Hz of laser repetition rate shows an interference pattern; this occurs when the film is not highly transparent.

As previously done the energy loss functions of the films were calculated via Kramers-Kronig model and their resulting smoothed envelopes are plotted in figure 4.48. A clear and dominant UV peak is observed for both samples, which locates the position of the band gap and the corresponding values are listed in table 4.20. For S4 sample, the ZnO film deposited at a repetition rate of 50 Hz, three peaks precede the UV peak, and they are located at wavenumbers 15369 cm^{-1} (650 nm), 19300 cm^{-1} (520 nm) and 22770 cm^{-1} (440 nm), corresponding to the interference of light from this sample.

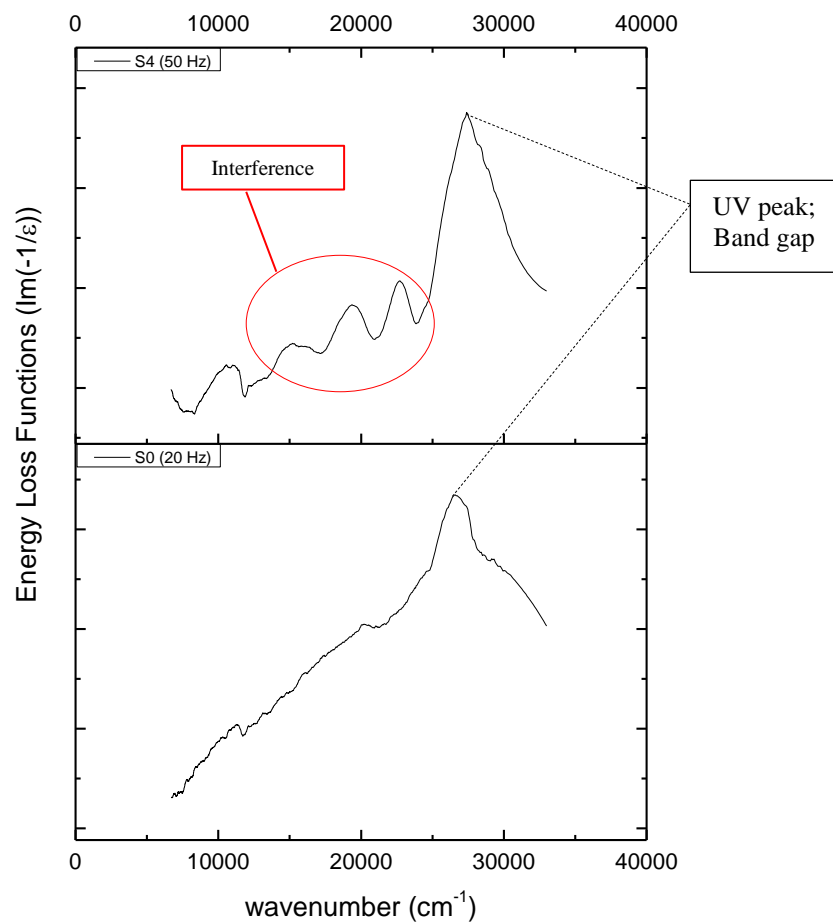


Figure 4.48: Energy loss functions of ZnO films deposited at different laser frequencies, 10 mTorr oxygen pressure and substrate temperature 725°C

Table 4.20: Band gap energy values for films deposited at different laser repetition rates, 10 mTorr oxygen pressure and substrate temperature 725°C

Sample	Pressure	Energy	Temp	RepRate	Band gap (eV)	Error (eV)
S0	10mTorr	400mJ	725°C	20Hz	3.30	0.04
S4	10mTorr	400mJ	725°C	50Hz	3.396	0.023
Target					3.181	0.026

The band gap of the resulting ZnO thin films has been greatly influenced by the laser repetition rate; with the increase in the repetition rate the band gap energy value increased from 3.30 eV at 20 Hz to 3.396 eV at 50 Hz (figure 4.49).

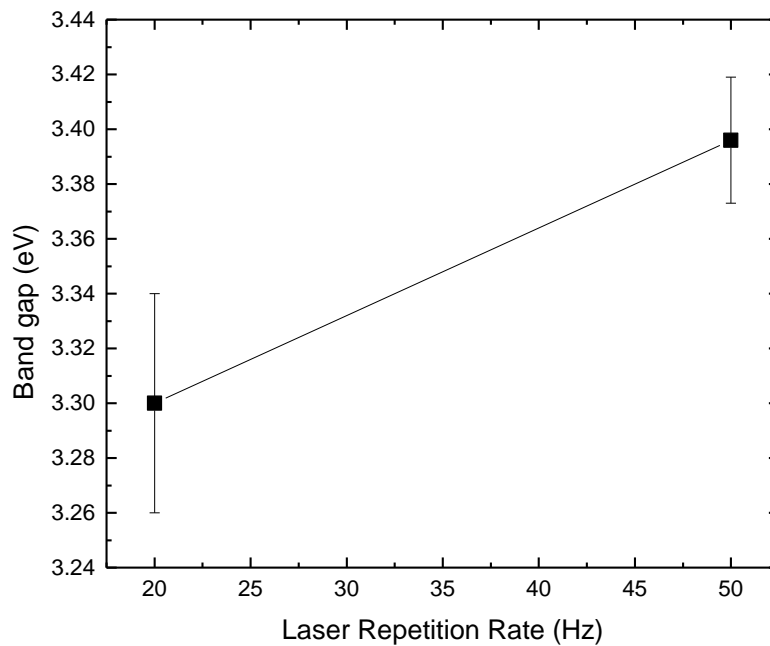


Figure 4.49: Variation of the band gap energy value as a function of laser repetition rate, for films deposited at 10 mTorr of oxygen pressure and 725°C of substrate temperature

4.7. Large Area Depositions

This section presents the work done to deposit large area ZnO thin films. Three samples were deposited under different conditions that are summarized in table 4.21.

The target installed is the 99.99% pure ZnO and the substrate is silicon pieces. The deposition conditions, namely, the substrate temperature, oxygen pressure, laser energy and repetition rate were chosen based on the XRD results and band gap energy values investigated in the previous sections.

Table 4.21: Deposition conditions for large area samples

Sample #	Temperature (°C)	Pressure (mTorr)	Energy (mJ)	RepRate (Hz)	Deposition time	S-T distance
I	825	100	400	20	30 mins	~7.5 cm
II	825	50	250	20	45 mins	~7.5 cm
III	825	50	250	20	1 hr + 27 mins	~8.5 cm

The laser was aligned to hit the target in such a way by projecting its strike on the metal plate it is at quarter its radius, this is where one piece of silicon was pasted and the rest two pieces followed along the diameter of the metal plate (Appendix C). Note that the speed of rotation of the substrate holder was intermediate.

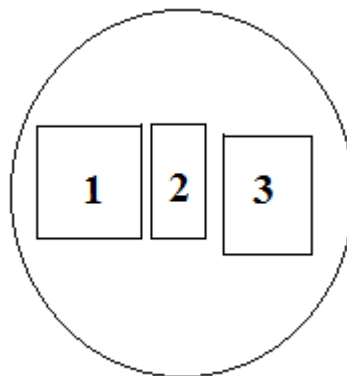


Figure 4.50: Schematic representation of the three silicon pieces pasted on the metal plate

After deposition the pieces were cut in half and cross-sectional SEM was performed to measure their thickness.

Some cross-sectional SEM images are shown in figure 4.52.

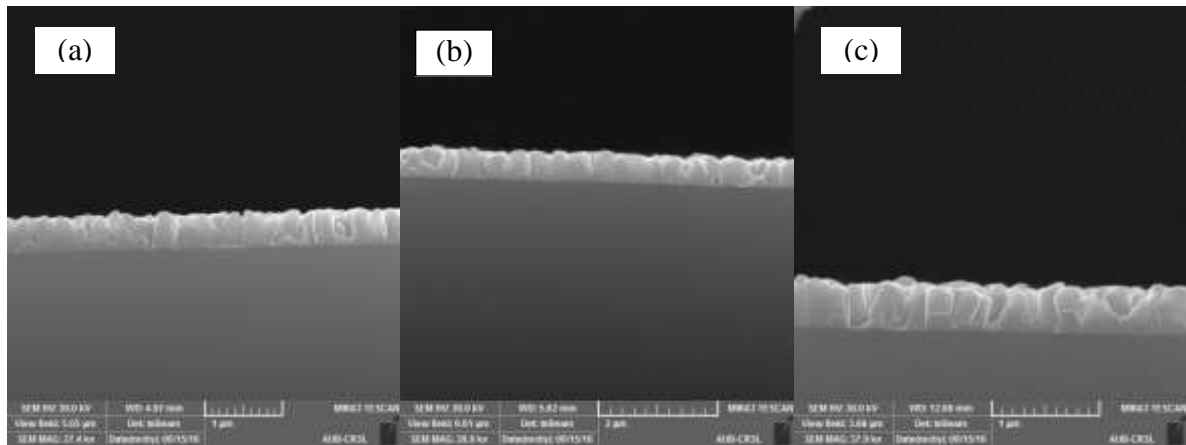


Figure 4.51: Cross-sectional SEM of sample I for the (a) 1 (b) 2 and (c) 3 pieces

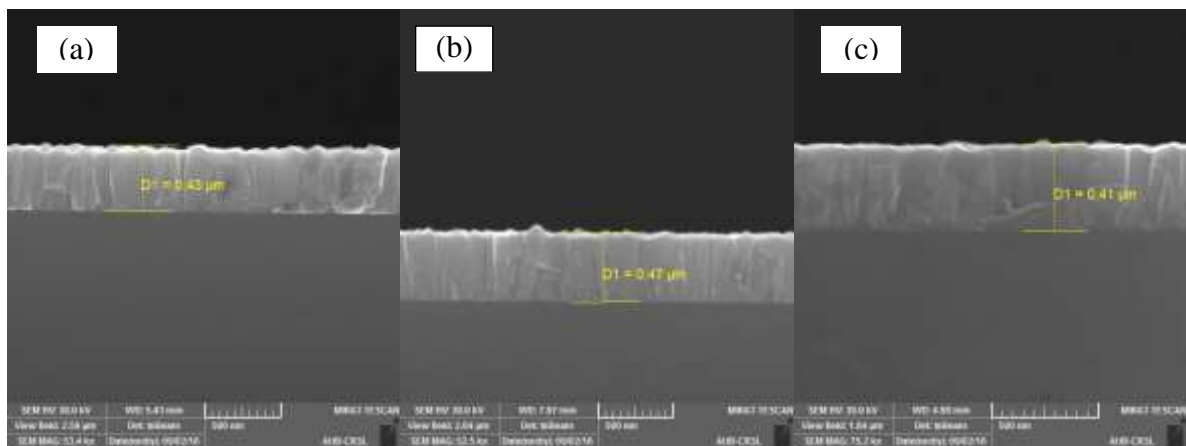


Figure 4.52: Cross-sectional SEM of sample II for the (a) 1 (b) 2 and (c) 3 pieces

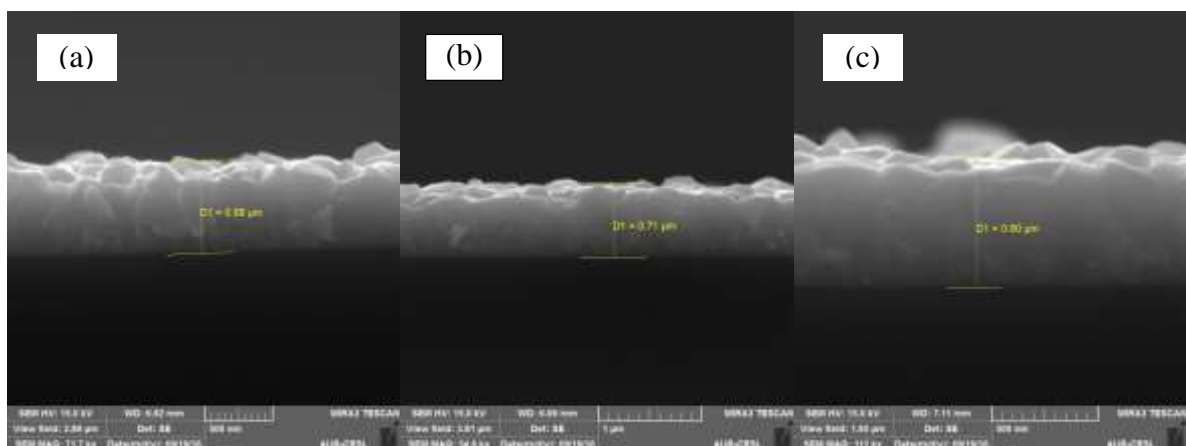


Figure 4.53: Cross-sectional SEM of sample III for the (a) 1 (b) 2 and (c) 3 pieces

The average thickness of the three pieces – two on the edges of the metal plate t_1 and t_3 and one in the middle t_2 – are reported in table 4.22.

Table 4.22: Average thickness of large area deposited samples

Sample #	Average thickness t_1	Average thickness t_2	Average thickness t_3
I	489 ± 6 nm	527 ± 12 nm	467 ± 32 nm
II	0.43 ± 0.015 μm	0.466 ± 0.007 μm	0.41 ± 0.016 μm
III	0.66 ± 0.02 μm	0.677 ± 0.017 μm	0.617 ± 0.012 μm

We can notice that the thickness of the ZnO thin film is greatest for the one located at the center of the metal plate (t_2); this is due to the fact this specific piece experiences more deposition than the edges since its rotation is least.

The percentage difference in thickness among the three deposited ZnO thin films for each sample is given in table 4.23. The percentage difference is given by:

$$= \frac{|\text{difference}|}{\text{average}} \times 100$$

Table 4.23: Percentage difference in thickness among the different deposited ZnO thin film pieces for each sample

Sample #	% difference between t_1 and t_2	% difference between t_2 and t_3	% difference between t_1 and t_3
I	7.48%	12.07%	4.6%
II	8.04%	12.8%	4.76%
III	2.54%	9.27%	6.74%

In sample III, the *maximum* variation in film thickness is 9.27%, hence we were able to achieve thickness uniformity below 10%.

X-Ray diffraction analysis of sample III has been carried out

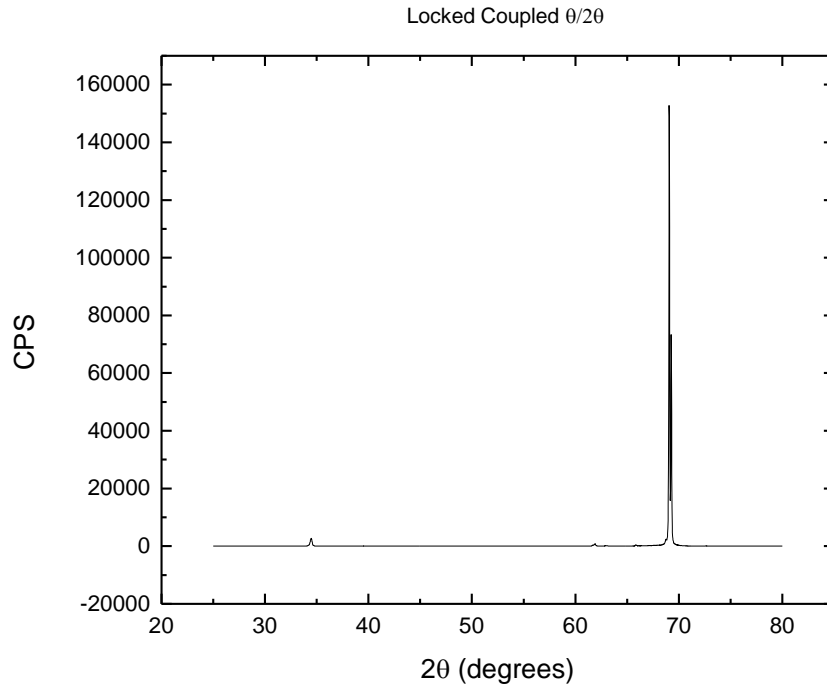


Figure 4.54: $\theta/2\theta$ scan of sample III

The $\theta/2\theta$ scan (i.e. Bragg-Brentano geometry) shows a strong reflection from the silicon substrate; the strong XRD peak appearing at an angle of $2\theta \sim 69.1^\circ$ correspond to reflections from the (400) Si planes.

GIXRD (Figure 4.55) reveals a strong (002) peak at an angle of $\sim 34.5^\circ$, which indicates that the deposited ZnO film (III) has a preferred orientation along the c-axis. However, other ZnO XRD peaks were shown at angles $\sim 36.3^\circ$, 62.9° , 67.9° and 72.6° , resembling reflections from the (101), (103), (112) and (004) planes respectively. Hence the ZnO XRD pattern is a nearly polycrystalline pattern. The remaining peaks are suspected to be reflections from either the silicon substrate or the ZnO film because these XRD peaks are common to both. The XRD patterns presented in figures 4.54 and 4.55 and their EVA matches are shown in Appendix D.

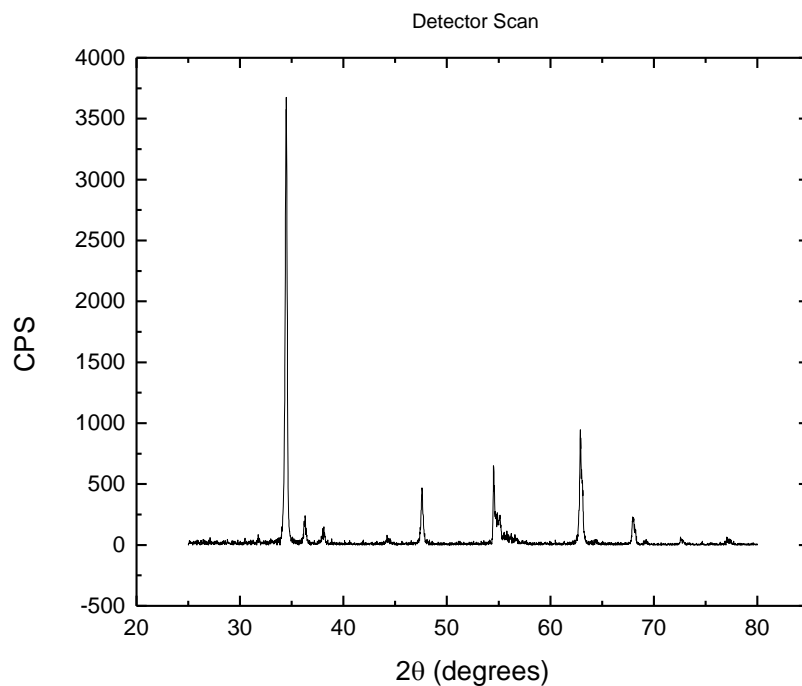


Figure 4.55: GIXRD of sample III

4.8. Summary

As a summary of the work presented above, we have grown highly crystalline ZnO thin films at various sets of deposition parameters having a hexagonal structure and with an extremely strong preferential orientation along the c-axis. We were able to image different morphologies, some verifying the hexagonal wurtzite-type structure of the deposited thin films.

The investigated reflectivity measurements explained the extreme transparency of the resulting ZnO thin films (except for S2 sample); the percentage of reflectance was minimal in the infrared and visible range. In addition to the pronounced UV band edge emission in the energy loss functions, red, and blue emissions for some samples were detected, and were attributed to point defects in the thin films. Moreover, there has been

a significant variation in the band gap with the change in the deposition parameters (oxygen pressure, substrate temperature and laser repetition rate)

Concluding from XRD results, at a substrate temperature of 725°C, the optimal oxygen pressure was 1 mTorr, however, at the optimal substrate temperature 825°C, an oxygen pressure of 25 mTorr and 50 mTorr produced the best crystalline quality of ZnO thin films. Compared to a laser energy of 400 mJ, a 200 mJ laser energy resulted in a better crystalline quality of the deposited ZnO films, while rocking curves proved the opposite. Although at a high repetition rate (50 Hz) the crystallinity of the film was better than that deposited at 20 Hz, the energy loss function revealed an interference pattern, indicating that the film is not highly transparent.

A uniformity in the thickness of large area - full wafer - depositions below 10 % was successfully achieved, and XRD measurements showed a preferred c-orientation of the layers, although not strong.

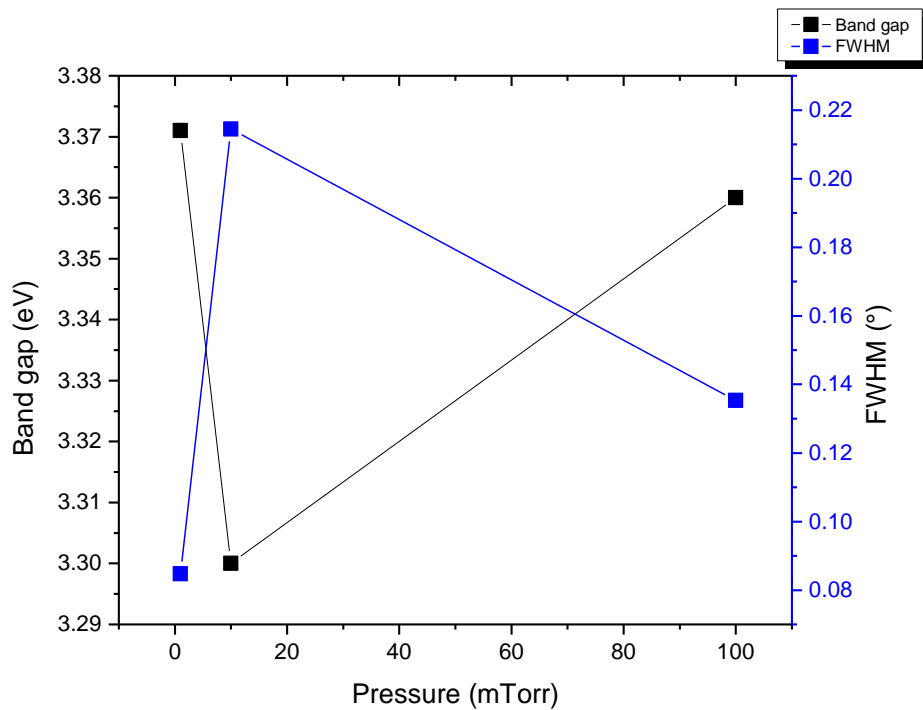
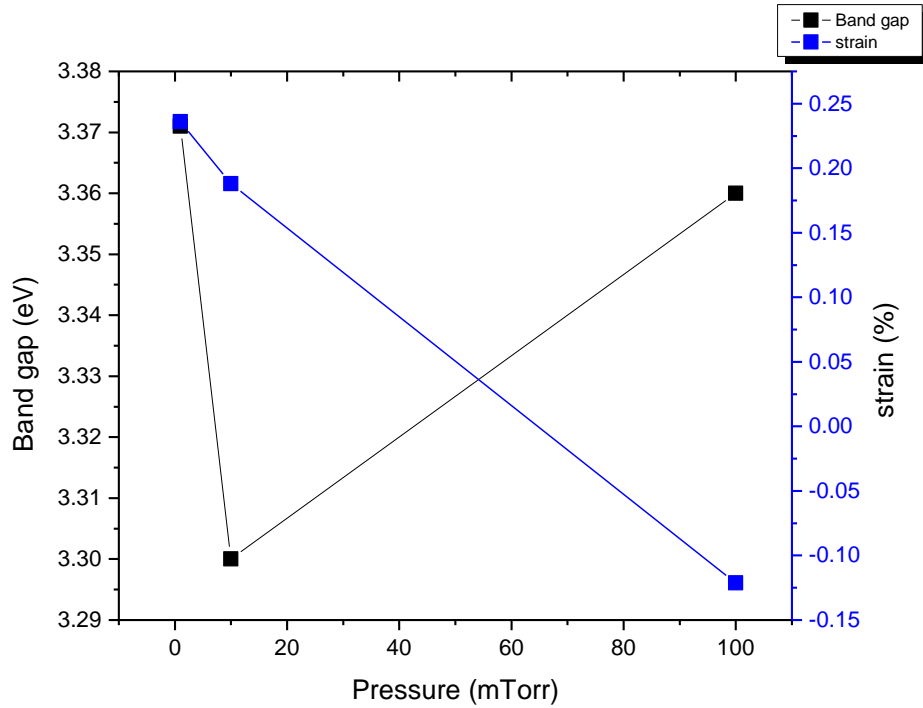
4.9. Further Analysis

In this section we present the correlation between the variation in the band gap with the macroscopic strain ϵ and the FWHM XRD (002) peak.

4.9.1. *Variation of the Band gap, strain and FWHM XRD peak as function of O₂ pressure at 725°C*

	T=725°C			
	P(mTorr)	Band gap (eV)	strain ϵ	FWHM (002)
S5	1	3.371	0.23606	0.085
S0	10	3.30	0.18812	0.214
S6	100	3.36	-0.12125	0.135

The strain has a significant impact on the band gap, and we can notice in the graph below the change in the band gap with the change in the macroscopic strain, however, there's no clear trend for this change.

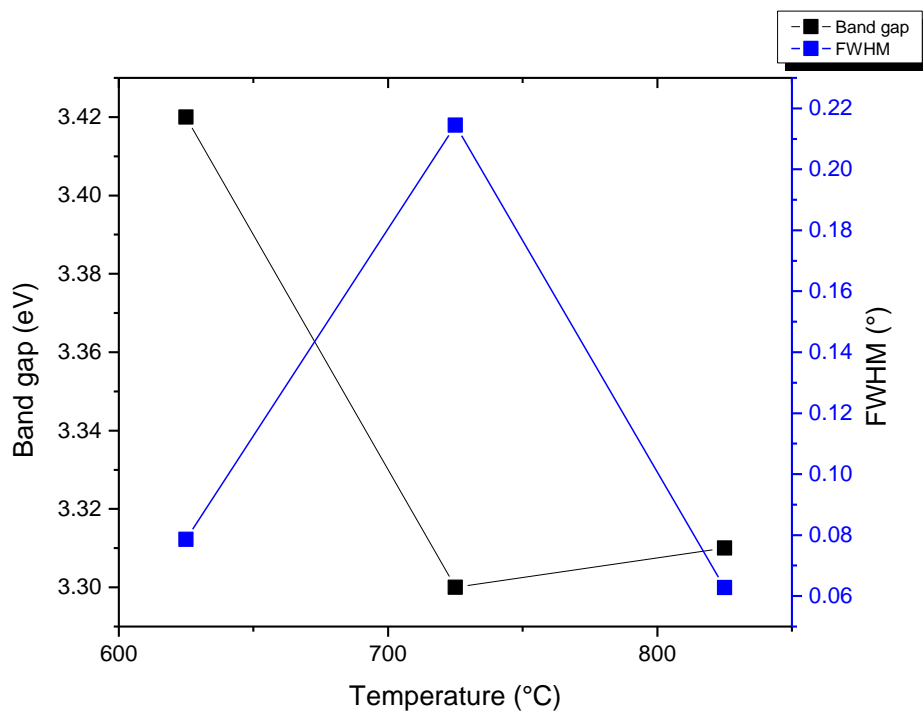
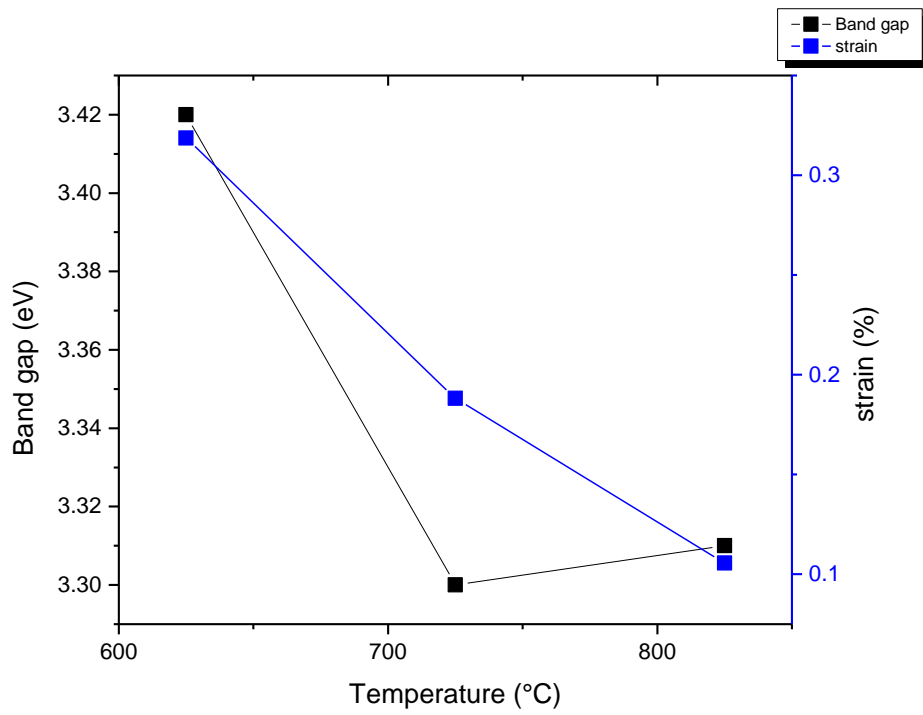


There's a correlation between the variation in the band gap and FWHM XRD peak with oxygen pressure; there is an inverse relation between both. Along the pressure scale as the FWHM increases (*decreases*) the band gap decreases (*increases*).

4.9.2. Variation of the Band gap, strain and FWHM XRD peak as function of substrate temperature at 10 mTorr

P=10mTorr				
	Temperature (°C)	Band gap (eV)	strain ϵ	FWHM (002)
S3	625	3.42	0.31869	0.079
S0	725	3.30	0.18812	0.214
S2	825	3.31	0.10569	0.063

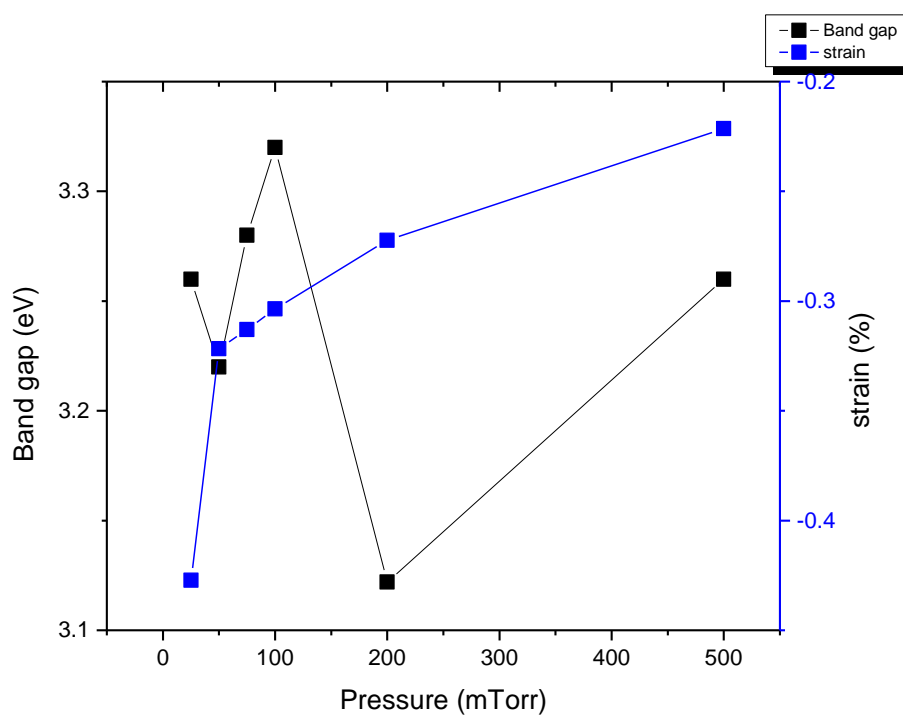
Clearly, the band gap and the strain are interrelated; the strain in the thin films affects the band gap. Besides, the FWHM XRD peak is also observed to influence the band gap; from the graph below, the inverse relation discussed in the previous section (4.9 i) occurs in the case of substrate temperature too, the decrease in the band gap value is accompanied by the increase in the FWHM, although not with the same proportion.

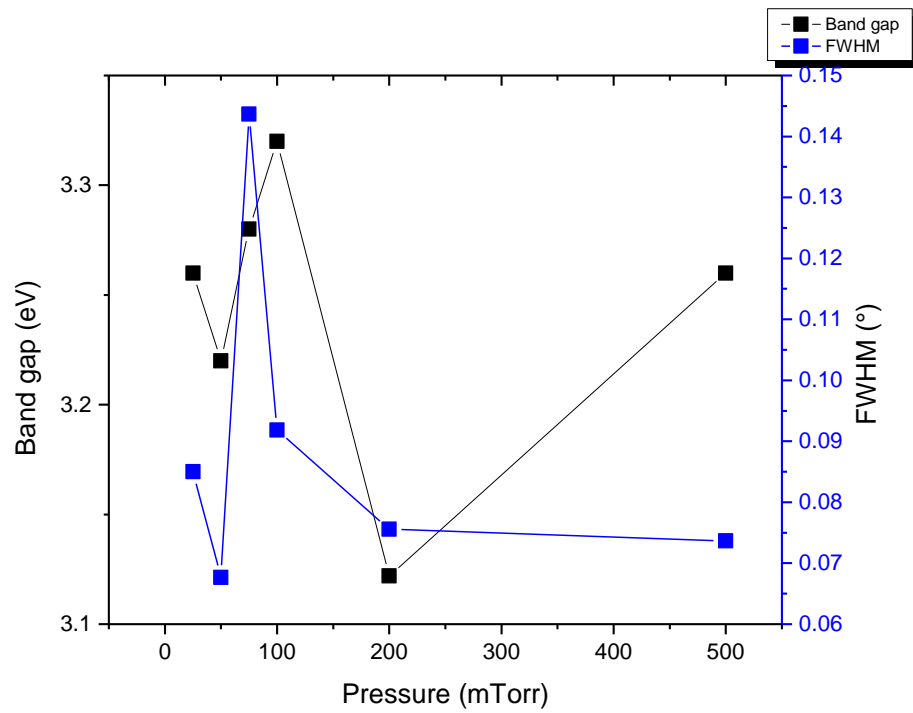


4.9.3. Variation of the Band gap, strain and FWHM XRD peak as a function of O₂ pressure at 825°C

T=825°C				
	P(mTorr)	Band gap (eV)	strain ϵ	FWHM (002)
S7	25	3.26	-0.42726	0.085
S8	50	3.22	-0.32176	0.068
S9	75	3.28	-0.31302	0.144
S10	100	3.32	-0.30351	0.092
S11	200	3.122	-0.27228	0.076
S12	500	3.26	-0.22136	0.074

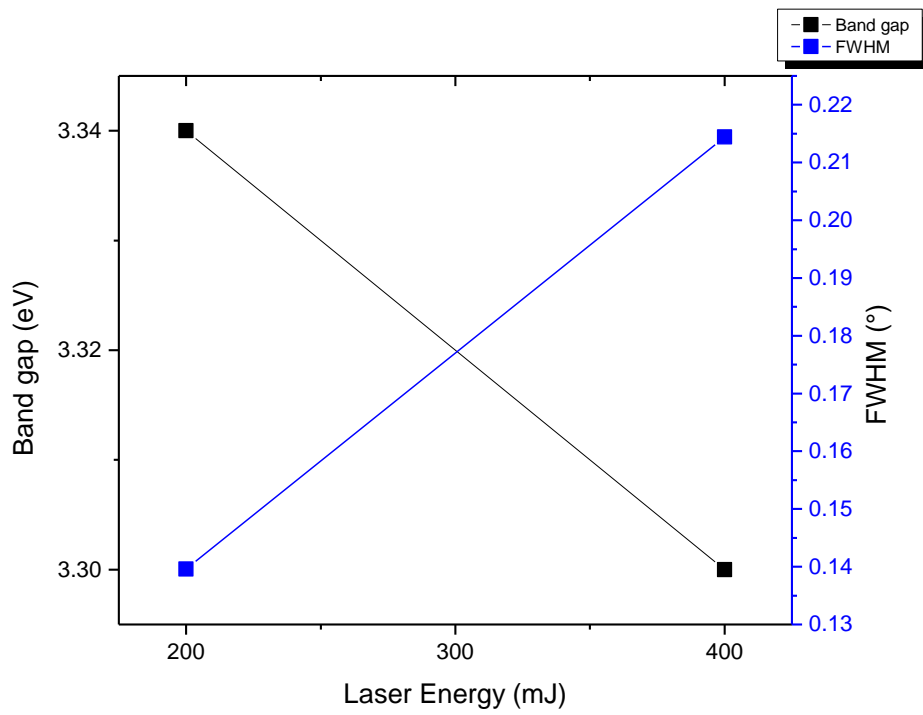
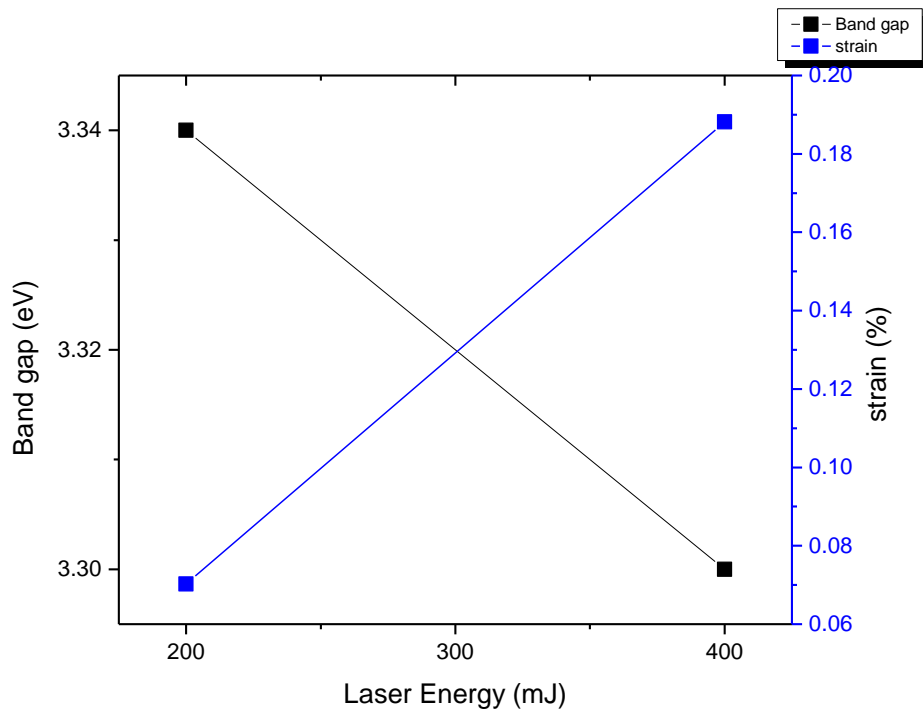
In the figure we can notice that the variation in the band gap and the FWHM is directly proportional and sometimes inversely proportional.





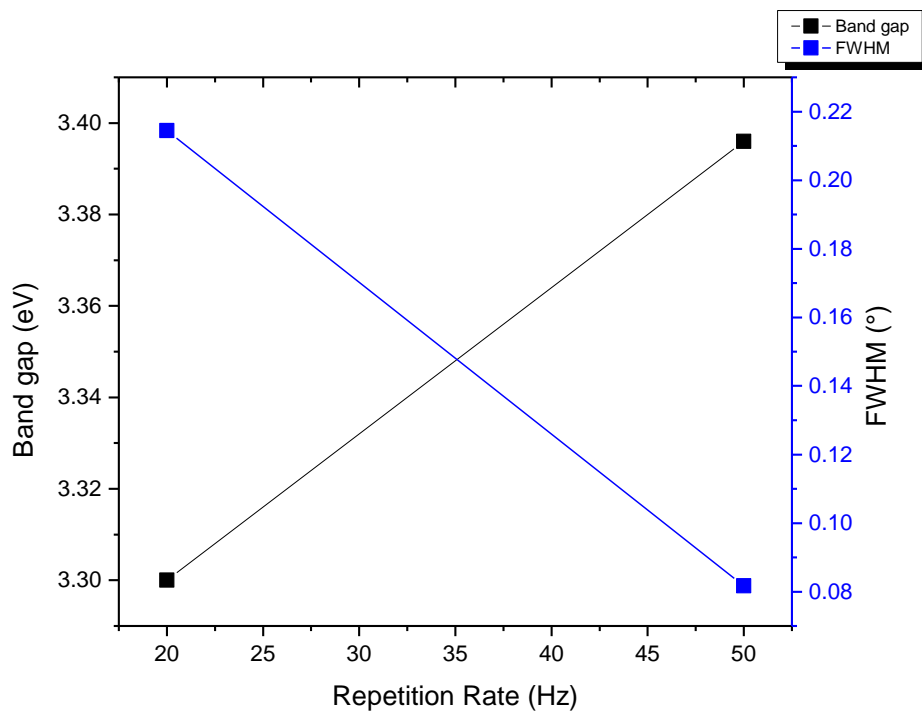
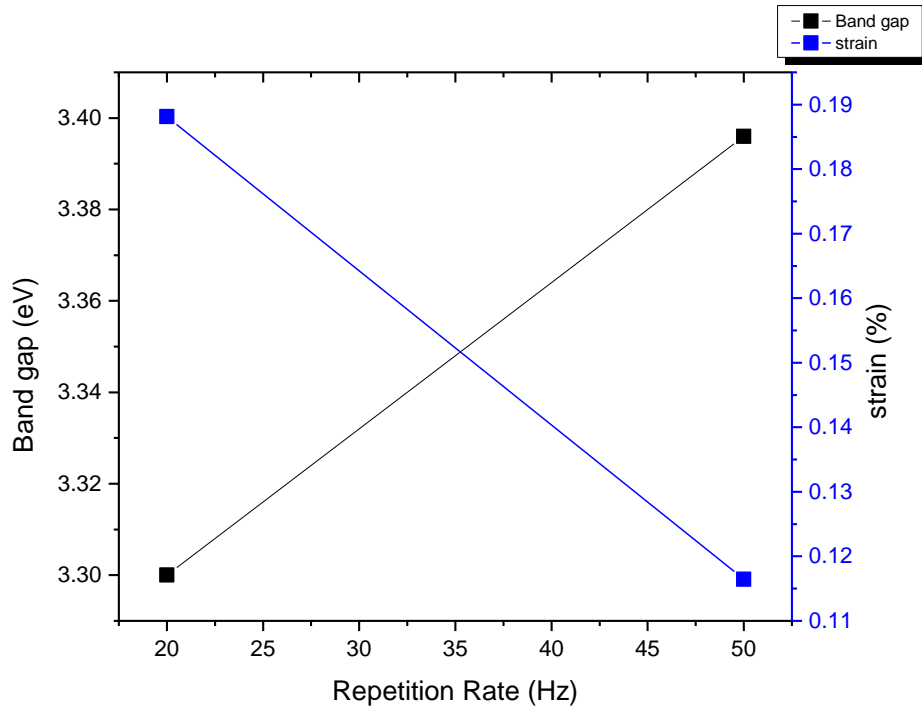
4.9.4. Variation of the Band gap, strain and FWHM XRD peak as a function of laser energy at 10 mTorr and 725°C

	Laser Energy (mJ)	Band gap (eV)	strain ϵ	FWHM (002)
S1	200	3.34	0.07023	0.140
S0	400	3.30	0.18812	0.214



4.9.5. Variation of the Band gap, strain and FWHM XRD peak as a function of laser repetition rate at 10 mTorr and 725°C

	RR(Hz)	Band gap (eV)	strain ϵ	FWHM (002)
S0	20	3.30	0.18812	0.214
S4	50	3.396	0.11645	0.082



Chapter 5

CONCLUSION AND FUTURE DIRECTION OF THE WORK

5.1. Conclusion

In this study we fabricated zinc oxide (ZnO) thin films on sapphire substrates (Al_2O_3) at different deposition parameters, to test the impact of each set of conditions chosen on the crystallinity, morphology, elemental composition and band gap energy value of the deposited ZnO thin films. Our aim was to determine the optimum conditions of substrate temperature, ambient oxygen pressure, laser energy and repetition rate.

The experimental techniques employed were X-Ray Diffraction (XRD) for studying the crystalline quality, Scanning Electron Microscopy (SEM) for imaging the surface of the films, Energy Dispersive X-Ray Spectroscopy (EDX) to determine the atomic percentage of each of the zinc and oxygen atoms in the ZnO films and the Surface Profiler to calculate their thickness. Finally, the data collected from the UV-VIS-NIR spectroscopy technique was then entered in a corrected Kramers-Kronig MATLAB code that permits us to calculate the optical dielectric function from which we can get the band gap energy value.

We have successfully grown highly crystallized ZnO thin films which had a strong preferential orientation along the c-axis. Different surface morphologies were observed corresponding to the different growth modes. EDX measurements confirmed the same proportion of zinc and oxygen atoms in the films, and mainly no oxygen deficiencies. Lastly, the calculated band gap value showed a significant variation with the change in the deposition parameters.

Our analyses of the results have led to the following conclusions:

- All deposited ZnO thin films were determined to have a hexagonal crystal structure, and some SEM images revealed hexagonal nanostructures and pyramid-like nanostructures-S4 sample (RR=50 Hz). Besides, some images showed the formation of nano-rods in the films such as the one deposited at a laser energy of 200 mJ (S1 sample) and another at an oxygen pressure of 75 mTorr (S9 sample).
- The stress in the layers was varied from tensile to compression with the increase in oxygen pressure from 1 mTorr to 100 mTorr, at a substrate temperature of 725°C and the best crystallinity (smallest FWHM (002) peak) was observed at an oxygen pressure of 1 mTorr. This conclusion was confirmed by the rocking curve measurements; the smallest FWHM (0.07°) was obtained for this 1 mTorr-deposited ZnO film and its corresponding band gap value is 3.37 eV. The reflectivity of the samples over the infrared and visible range is minimal and the variation in the band gap as the O₂ pressure increases from 1 mTorr to 100 mTorr is considered to be within the experimental error; it's 3.3 eV at 10 mTorr and 3.36 at 100 mTorr. Blue emission was observed in the energy loss function of the sample deposited at 100 mTorr, and this was attributed to zinc interstitial defects.
- The narrowest (002) XRD peak and rocking curve were obtained for the sample deposited at a substrate temperature of 825°C (S2 sample) with a fixed oxygen pressure of 10 mTorr, hence 825°C is selected as the optimal substrate temperature for which the best crystallinity is attained,

and the ratio of the atomic composition (Zn atoms: O atoms) of this sample was closest to 1. The rocking curve had two peaks which indicate that this S2 sample possessed domains with low angle boundaries. The stress in the films deposited at temperatures ranging from 625°C to 825°C was tensile with a decreasing trend towards a zero strain. The sample deposited at 825°C reflects a blue-green color, while the other samples were observed to be extremely transparent. The energy loss functions did not reveal major defects in the produced thin films. Surprisingly, the band gap of the sample grown at 625°C has an unreasonable and a high band gap 3.42 eV, while both samples grown at 725°C and 825°C have the same band gap energy value (3.3 eV).

- All ZnO films deposited at a substrate temperature of 825°C and oxygen pressures ranging from 25 mTorr to 500 mTorr possessed compressive stress in the layers, and presented an increasing trend towards stress-free layers. Although all the samples deposited over this range of oxygen pressure were highly c-axis oriented, the 50 mTorr-deposited ZnO film resulted in the narrowest (002) XRD peak, while the one deposited at 25 mTorr had the smallest rocking curve with a double peak due to domains in the film. Moreover, with the increase in oxygen pressure the thickness of the ZnO films decreased. The samples are greatly transparent; their reflectivity in the near infrared and visible range is very low (below 5%). The energy loss functions of the samples grown at 25 mTorr, 50 mTorr and 75 mTorr exhibited a small red emission, in addition to a broad blue emission for the 50 mTorr deposited film; the red and blue emissions have been linked to oxygen vacancies and zinc interstitials, respectively.

The existence of excitons, at room temperature, in the sample deposited at 200 mTorr has been detected. The band gap of the ZnO thin films in this set has been varied from 3.12 eV to 3.32 eV with no defined trend in the variation as the oxygen pressure increases.

- ZnO film deposited at 200 mJ of laser energy showed a better crystallinity than the one deposited at 400 mJ, by judging from the (002) XRD peak, however, rocking curves revealed that the 400 mJ deposited film had a better crystalline quality. The stress in the layers in both films was tensile; the strain in the 400 mJ deposited film is much larger than the 200 mJ-film, therefore encountering greater stress in the layers. The variation in the laser energy did not remarkably affect the optical properties; no major defects were detected and the variation in the band gap energy fell within the experimental error (3.30 ± 0.04 eV).
- As for the laser repetition rate, the sample grown at a high repetition rate (50 Hz) had a better crystalline quality than the one grown at 20 Hz; for a high repetition rate (50 Hz) both the *out-of-plane* and the *in-plane* grain sizes increase considerably, as well as the thickness of the ZnO thin film, while no significant variation in the strain is noted; the stress in both films is tensile; the 20 Hz-deposited film holds slightly greater stress in the layers than the film grown at 50 Hz. Rocking curves showed that both samples are highly crystallized, and the one deposited at 50 Hz exhibited a double peak which is again an evidence of domains in the film. The laser repetition rate greatly influences the optical properties; for the 50 Hz-deposited sample an interference pattern is observed in the visible range of its energy loss function graph, and its corresponding

band gap energy (3.396 eV) is larger than the 20 Hz-deposited film (3.3 eV).

- For large area depositions we were able to achieve uniformity in the thickness at different locations of the full wafer below 10%. XRD measurements showed preferred c-axis oriented layers but some other orientations as well.

5.2. Future Work

There are two main issues that requires further investigation, first the effect of the laser energy has to be done on a broad energy ranges, as well as the laser repetition rate, in order to obtain and follow a certain trend that can say something clear in regard to their effect on the properties of the deposited layers. Interestingly, as a challenge the deposition on a larger area – a full wafer – has to be further investigated, in order to study the uniformity of the deposited layers and their crystalline quality. This is significantly applicable in lithography and in patterning of zinc oxide crystals for the purpose of enhancing the performance of electrical and optical devices.

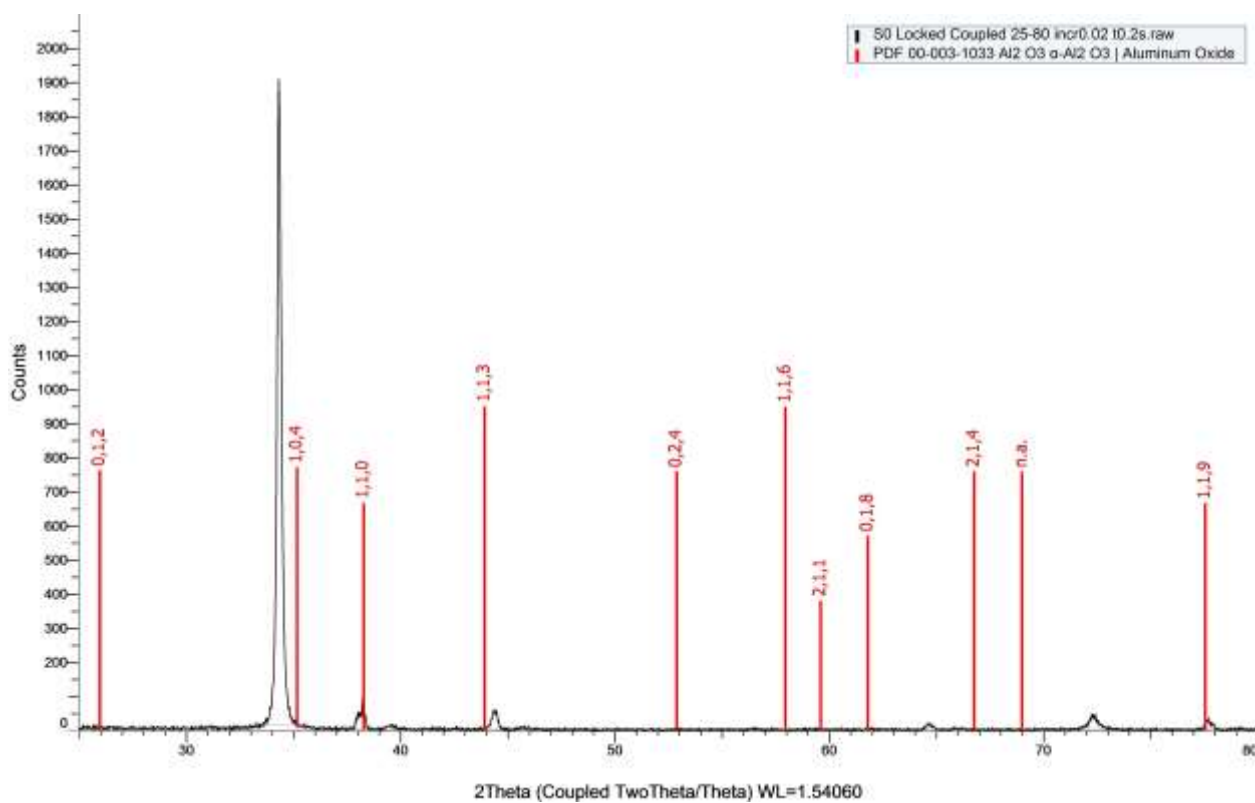
APPENDIX A

Sample information table:

Sample Number	Substrate (S)	Target (T)	Laser Energy	Temperature	Pressure	RepRate	S-T distance	Deposition time
S0	Sapphire	ZnO	400mJ	725°C	10 mTorr	20 Hz	7.5 cm	20mins
S1	Sapphire	ZnO	200mJ	725°C	10 mTorr	20 Hz	7.5 cm	20mins
S2	Sapphire	ZnO	400mJ	825°C	10 mTorr	20 Hz	7.5 cm	20mins
S3	Sapphire	ZnO	400mJ	625°C	10 mTorr	20 Hz	7.5 cm	20mins
S4	Sapphire	ZnO	400mJ	725°C	10 mTorr	50 Hz	7.5 cm	20mins
S5	Sapphire	ZnO	400mJ	725°C	1 mTorr	20 Hz	7.5 cm	20mins
S6	Sapphire	ZnO	400mJ	725°C	100 mTorr	20 Hz	7.5 cm	20mins
S7	Sapphire	ZnO	400mJ	825°C	25mTorr	20 Hz	7.5 cm	20mins
S8	Sapphire	ZnO	400mJ	825°C	50mTorr	20 Hz	7.5 cm	20mins
S9	Sapphire	ZnO	400mJ	825°C	75mTorr	20 Hz	7.5 cm	20mins
S10	Sapphire	ZnO	400mJ	825°C	100mTorr	20 Hz	7.5 cm	20mins
S11	Sapphire	ZnO	400mJ	825°C	200mTorr	20 Hz	7.5 cm	20mins
S12	Sapphire	ZnO	400mJ	825°C	500mTorr	20 Hz	7.5 cm	20mins

APPENDIX B

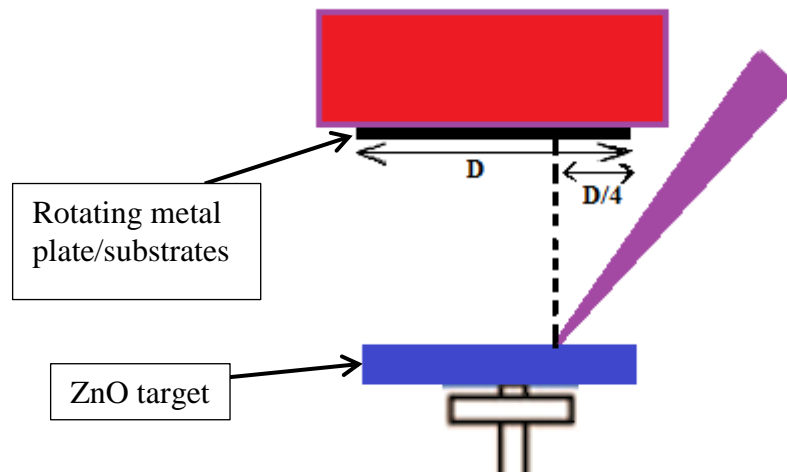
EVA match of S0 sample; the sample deposited at laser energy and repetition rate of 400 mJ and 20 Hz, respectively, 10 mTorr of oxygen pressure and 725°C of substrate temperature.



The match (red vertical lines) represents the XRD pattern of sapphire.

APPENDIX C

In this appendix some experimental details about the large area depositions (Section 4.7) is shared.



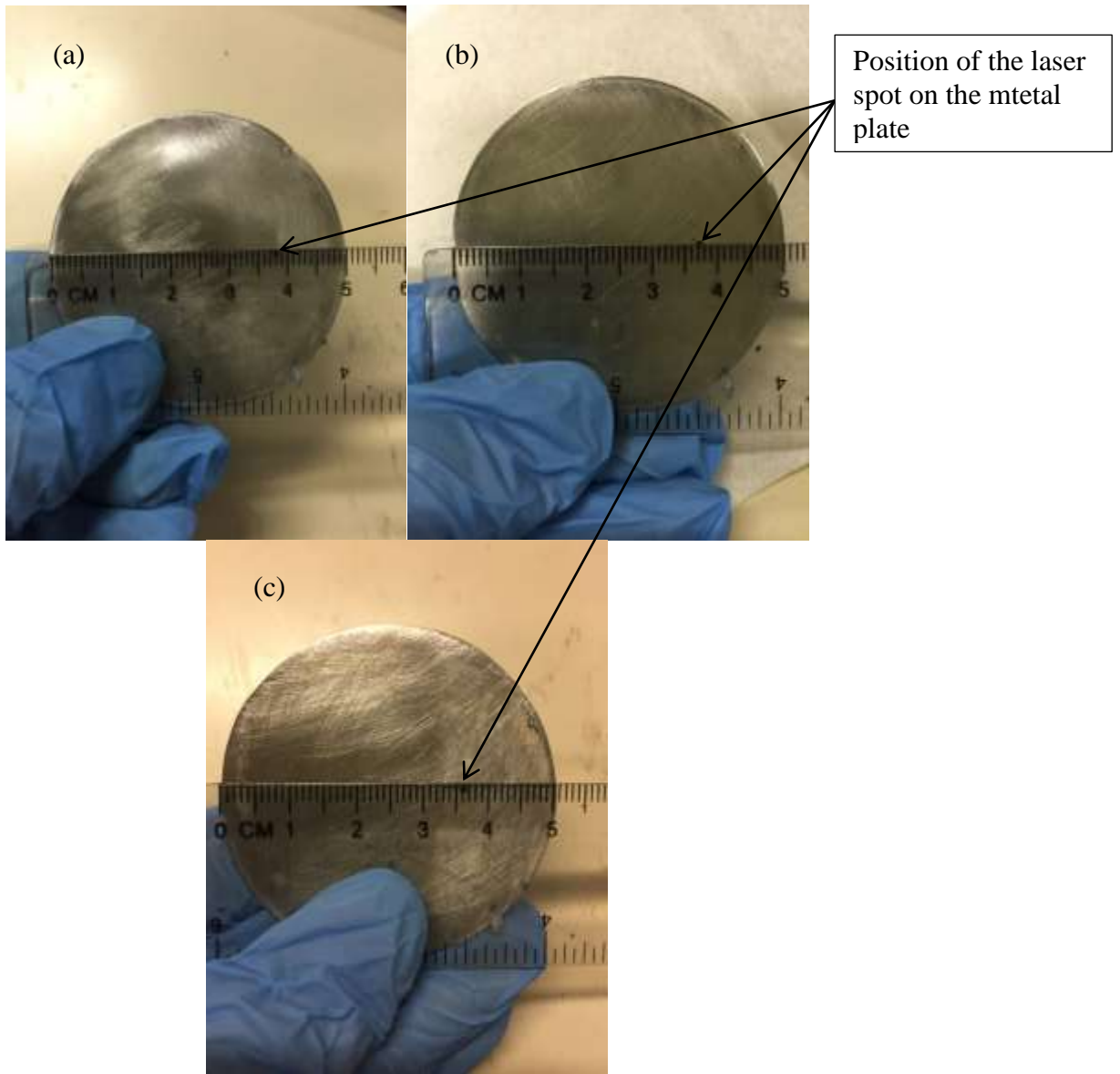
Schematic representation of laser alignment for full wafer deposition by PLD



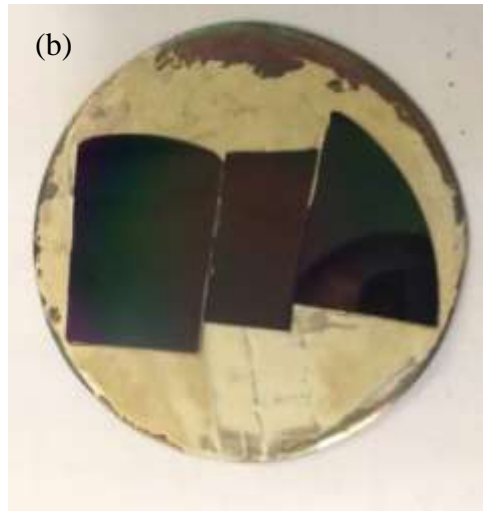
Laser alignment



Speed of rotation of the substrate holder for samples I, II and III



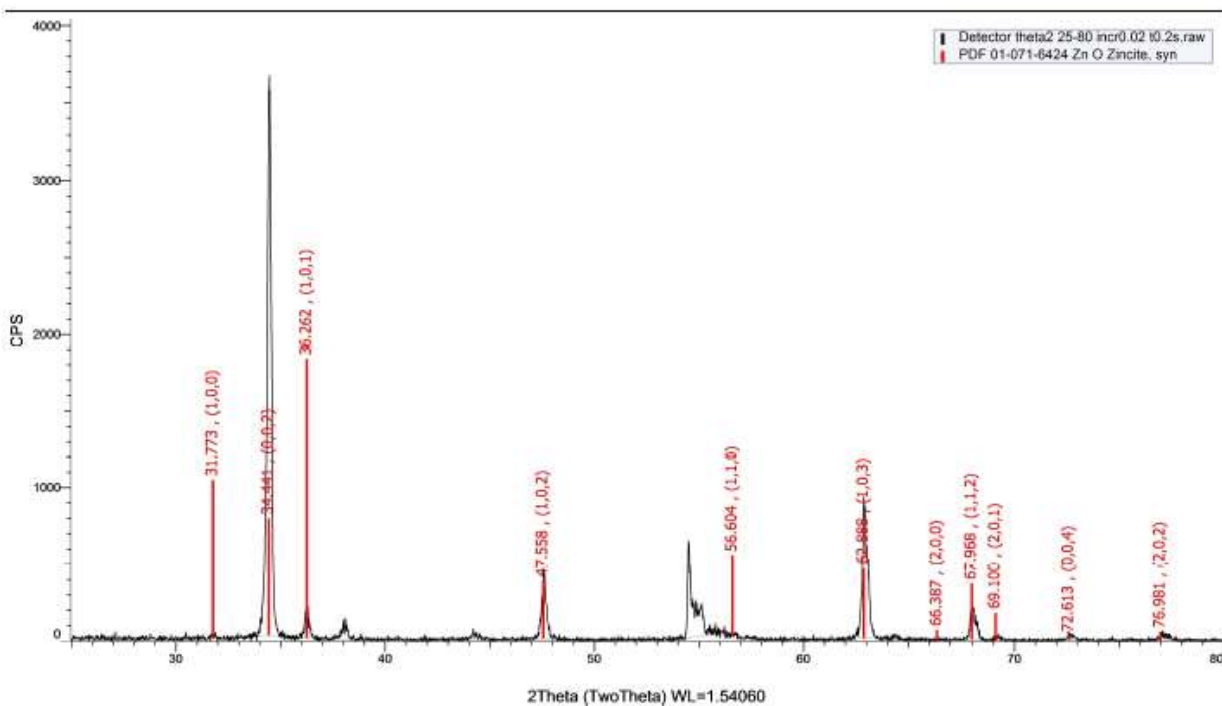
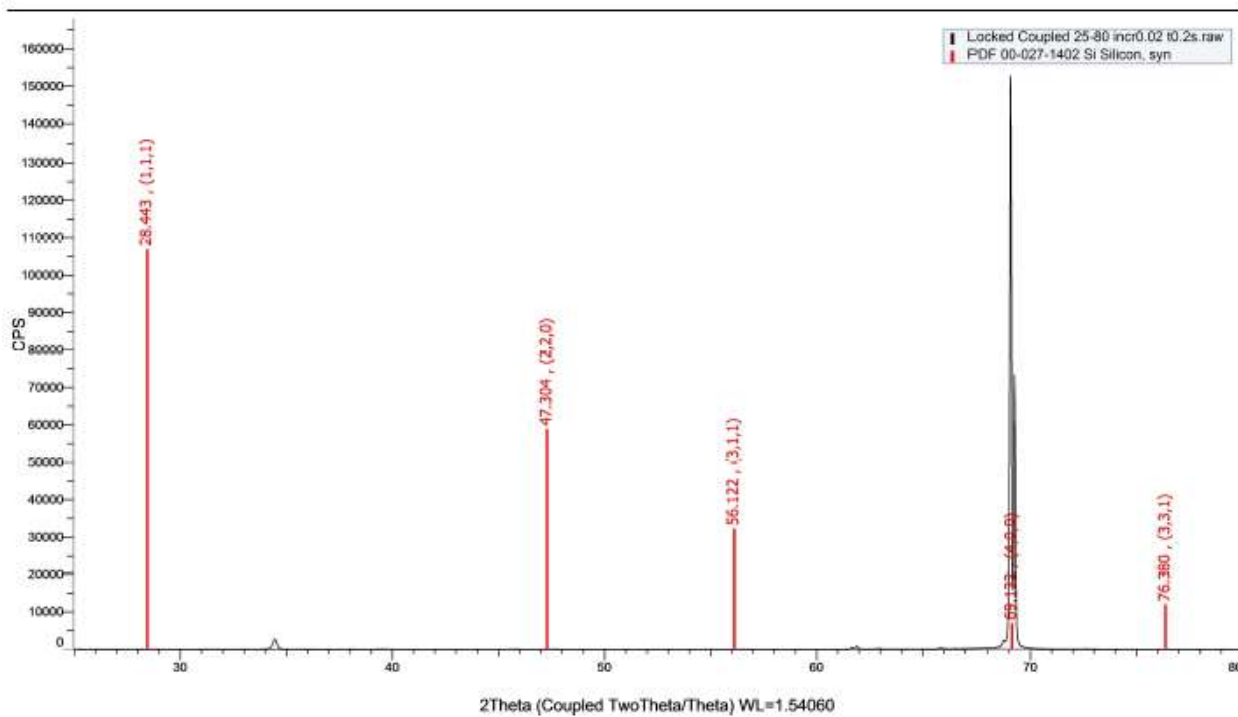
Laser alignment of samples (a) I, (b) II and (c) III



Silicon pieces glued on the metal plate for samples (a) I, (b) II and (c) III

APPENDIX D

EVA match of the $\theta/2\theta$ and detector scans for Sample III, the large area deposited ZnO film. (Section 4.7)



APPENDIX E



S2 sample; emphasizing the reflection of a color

REFERENCES

- Abi Akl, M. N. (2009). Phase Control of Manganese Dioxide Thin Films by Plasma Assisted Laser Ablation. Master's Thesis. American University of Beirut, Lebanon.
- Abu Amer, R. I. (2015). Crystalline and Optical Properties of Zinc Oxide Nanoparticles Synthesized by a Solvent Based Technique. Master's Thesis. American University of Beirut, Lebanon.
- Ali, F. A. (2011). Literature Review, in Investigation on the Properties of Pure and Doped Nanocrystalline ZnO films. PhD thesis. Karunya University, Tamilnadu, India. Retrieved from http://shodhganga.inflibnet.ac.in/bitstream/10603/10122/9/09_chapter2.pdf
- Barnes, P., Jacques, S., & Vickers, M. (1997-2006). *Sources of Peak Broadening*. UK, University of London, Birkbeck College, School of Crystallography. Retrieved from <http://pd.chem.ucl.ac.uk/pdnn/peaks/broad.htm>
- Birkholz, M. (2005). *Principles of X-ray Diffraction*, in *Thin Film Analysis by X-Ray Scattering*. Germany, Weinheim: Wiley-VCH Verlag GmbH & Co. KGaA.
- Chrisey, D. B., & Hubler, G. K. (1994). *Pulsed Laser Deposition of Thin Films*. Canada: John Wiley & Sons, Inc.
- Greer, J. A., & Tabat, M. D. (1995). Large-area pulsed laser deposition: Techniques and applications. *Journal of Vacuum Science and Technology A*, 13(3), 1175.
- Hoffman, D. M., Singh, B., & Thomas, III, J. H. (1998). *Handbook of Vacuum Science and Technology*. USA & UK: Academic Press. Retrieved from https://books.google.com.lb/books/about/Handbook_of_Vacuum_Science_and_Technolog.html?id=HWvo5gKTiv0C&redir_esc=y
- Jang, Y. R., Yoo, K. H., & Park, S. M. (2010). Properties of ZnO Thin Films Grown on Si (100) Substrates by Pulsed Laser Deposition. *Journal of Material Science and Technology*, 26(11), 973-976.

Langford, J. I., & Louër, D. (1982). Diffraction Line Profiles and Scherrer Constants for Materials with Cylindrical Crystallites. *Journal of Applied Crystallography*, 15, 20-26.

Lin, C. C., Hsiao, C. S., Chen, S. Y., & Cheng, S. Y. (2004). Ultraviolet Emission in ZnO Films Controlled by Point Defects. *Journal of The Electrochemical Society*, 151 (5), G285-G288.

Liu, Z. W., Ong, C. K., Yu, T., & Shen, Z. X. (2006). Catalyst-free pulsed-laser-deposited ZnO nanorods and their room-temperature photoluminescence properties. *Applied Physics Letters*, 88, 053110.

Morkoç, H., & Özgür, Ü. (2009). *General Properties of ZnO*, in *Zinc Oxide: Fundamentals, Materials and Device Technology*. Germany, Weinheim: Wiley-VCH Verlag GmbH & Co. KGaA.

Mosca, M., Macaluso, R., Cali, C., Butté, R., Nicolay, S., Feltin, E., ... Grandjean, N. (2013). Optical, structural, and morphological characterisation of epitaxial ZnO films grown by pulsed-laser deposition. *Thin Solid Films*, 539, 55-59.

Nie, J. C., Yang, J. Y., Piao, Y., Li, H., Sun, Y., Xue, Q. M., ... Tu, Q. Y. (2008). Quantum confinement effect in ZnO thin films grown by pulsed laser deposition. *Applied Physics letters*, 93, 173104.

O'Haire, R., Meaney, A., McGlynn, E., Henry, M. O., Duclère, J. -R., & Mosnier, J. -P. (2006). Growth of crystalline ZnO nanostructures using pulsed laser deposition. *Superlattices and Microstructures*, 39, 153-161.

Perrière, J., Millon, E., & Craciun, V. (2006). *Zno and Zno-Related Compounds*, in *Pulsed Laser Deposition of Thin Films: Applications-Led Growth of Functional Materials* (ed R. Eason). USA, New Jersey, Hoboken: John Wiley & Sons, Inc.

Prasad, P. N. (2004). *Growth and Characterization of Nanomaterials*, in *Nanophotonics*. USA, New Jersey, Hoboken: John Wiley & Sons, Inc.

Sandana, V. E., Rogers, D. J., Teherani, F. H., McClintock, R., Bayram, C., Razeghi, M., ... Falyouni, F. (2009). Comparison of ZnO nanostructures grown using pulsed laser deposition, metal organic chemical vapor deposition, and physical vapor transport. *Journal of Vacuum Science and Technology B*, 27(3), 1678.

Smyth, J. R., & McCormick, T.C. – Geology Course, Lecture notes. (Fall, 1995). GEOLOGY 3010. *X-ray Generation and Powder Diffraction*, in *Mineralogy: Fundamental Science of Earth Materials*. U.S. Colorado: University of Colorado.

Speakman, S. A. (2012). *Introduction to High Resolution X-Ray Diffraction of Epitaxial Thin Films*. Massachusetts Institute of Technology, Center for Materials Science and Engineering.

Sun, X. W., & Kwok, H. S. (1999). Optical properties of epitaxially grown zinc oxide films on sapphire by pulsed laser deposition. *Journal of Applied Physics*, 86(1), 408.

Susner, M. A., Carnevale, S. D., Kent, T. F., Gerber, L. M., Phillips, P. J., Sumption, M. D., & Myers, R. C. (2014). Catalyst-free ZnO nanowires on silicon by pulsed laser deposition with tunable density and aspect ratio. *Physica E*, 62, 95-103.

Taabouche, A., Bouabellou, A., Kermiche, F., Hanini, F., Menakh, S., Bouachiba, Y., ... Amara, S. (2013). Effect of Substrates on the Properties of ZnO Thin Films Grown by Pulsed Laser Deposition. *Advances in Materials Physics and Chemistry*, 3, 209-213.

Valerini, D., Caricato, A. P., Lomascolo, M., Romano, F., Taurino, A., Tunno, T., & Martino, M. (2008). Zinc oxide nanostructures grown by pulsed laser deposition. *Applied Physics A: Materials Science & Processing*, 93, 729-733.

Wei, X. Q., Zhang, Z., Yu, Y. X., & Man, B. Y. (2009). Comparative study on structural and optical properties of ZnO thin films prepared by PLD using ZnO powder target and ceramic target. *Optics and Laser Technology*, 41, 530-534.

Willmott, P. R., & Huber, J. R. (2000). Pulsed laser vaporization and deposition. *Reviews of Modern Physics*, 72(1), 315(14).

Yang, B., Kumar, A., Zhang, H., Feng, P., Katiyar, R. S., & Wang, Z. (2009). Growth of ZnO nanostructures on metallic and semiconducting substrates by pulsed laser deposition technique. *Journal of Physics D: Applied Physics*, 42, 045415.

Zhang, Z. G., Zhou, F., Wei, X. Q., Liu, M., Sun, G., Chen, C. S., ... Man, B. Y. (2007). Effects of oxygen pressures on pulsed laser deposition of ZnO films. *Physica E*, 39, 253-257.

Zhao, S., Zhou, Y., Zhao, K., Liu, Z., Han, P., Wang, S., ... Yang, G. (2006). Violet luminescence emitted from Ag-nanocluster doped ZnO thin films grown on fused quartz substrates by pulsed laser deposited. *Physica B*, 373, 154-156.

(2010). User's manual for *Bruker AXS D8 Advance/D8 Discover diffractometers*. Germany, Karlsruhe: Bruker AXS GmbH.

(2011). User's manual for *Mira 3 series Scanning Electron Microscope*. Czech Republic, Brno: TESCAN, a.s.

(2006). Operator manual for *INCA Energy Energy-Dispersive X-Ray Spectrometer*. Oxford Instruments Analytical Halifax Road, High Wycombe HP12 3SE, UK.

(2011). Energy Dispersive Spectroscopy (EDX). *CNR-ISTEC Institute of Science and Technology for Ceramics*. Retrieved from

<http://www.istec.cnr.it/index.php/eng/resources/expertises/96-chemico-physical-characteristics/207-energy-dispersive-spectroscopy-edx>

n.d. Cleaning Procedures for Silicon Wafers. USA, Irvine: University of California. Retrieved from <https://www.inrf.uci.edu/wordpress/wp-content/uploads/sop-wet-silicon-solvent-clean.pdf>

